UNIVERSIDADE FEDERAL DE JUIZ DE FORA

INSTITUTO DE CIÊNCIAS EXATAS

PÓS-GRADUAÇÃO EM FÍSICA

Ultrafast dynamics of excited carriers in GaAs by a time-resolved differential reflectivity

Hamid Reza Darabian

JUIZ DE FORA

MARCH, 2020

Ultrafast dynamics of excited carriers in GaAs by a time-resolved differential reflectivity

Hamid Reza Darabian

Tese de doutorado apresentada ao Programa de Pós-Graduação em Física da Universidade Federal de Juiz de Fora, como requisito parcial a obtenção do título de Doutor em Física.

Área de concentração: Física

Orientador: Prof. Dr. Virgílio de Carvalho dos Anjos

Coorientador: Dr. Seshadri Meruva
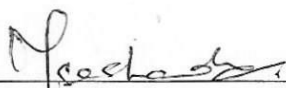
JUIZ DE FORA

MARCH, 2020

Hamid Reza Darabian

"Ultrafast dynamics of excited carriers in GaAs by a time-resolved differential reflectivity".

Tese apresentada ao Programa de Pós-graduação em Física, da Universidade Federal de Juiz de Fora como requisito parcial a obtenção do grau de Doutor em Física. Área de Concentração: Física.
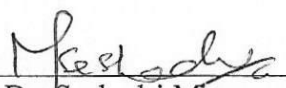
Aprovada em 02 de março de 2020.

BANCA EXAMINADORA

_____
Prof. Dr. Virgilio de Carvalho dos Anjos - Orientador
Universidade Federal de Juiz de Fora

_____
Prof. Dr. Seshadri Meruva - Coorientador
Universidade Federal Rural do Rio de Janeiro

_____
Prof.ª Dr.ª Ana Maria de Paula
Universidade Federal de Minas Gerais

_____
Prof. Dr. Christoph Friedrich Deneke
Universidade Estadual de Campinas

_____
Prof. Dr. Sergio Saul Makler
Universidade Federal de Juiz de Fora

_____
Prof. Dr. Wallon Anderson Tadaiesky Nogueira
Universidade Federal de Juiz de Fora

Acknowledgments

Resumo

Neste estudo, a dinâmica dos portadores de carga fotoexcitados nos cristais de GaAs é investigada pelo método de refletância diferencial res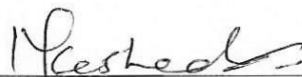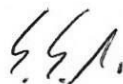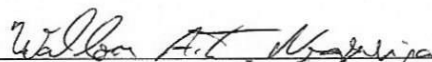olvida no tempo. O aparato é montado em uma configuração de "pump-probe", com comprimento de onda ajustável e duração de pulso de 100 fs. Três amostras de cristais de GaAs, cada uma com diferentes níveis de dopagem, são consideradas neste trabalho. Os dados obtidos na espectroscopia de "pump-probe" revelam que o tempo de relaxação dos elétrons excitados na banda de condução é altamente dependente de sua energia. Um tempo de relaxação em torno de 4 ps foi medido para os elétrons excitados em 720 nm, enquanto que para excitação em 800 nm, o tempo de relaxação é de 12 ps. Esse comportamento é atribuído a diferentes mecanismos de interação elétron-fônon. De modo que, para baixa energia de excitação, a interação Frohlich é dominante, enquanto que para alta energia de excitação o espalhamento "intervalley" desempenha o papel principal na relaxação energética dos elétrons. Além disso, as amostras com diferentes níveis de dopagem são consideradas para observar o efeito da dopagem na dinâmica dos elétrons, particularmente na relaxação de energia. Os dados não mostram mudanças consideráveis no tempo de relaxação dos elétrons para diferentes níveis de dopagem. No entanto, fica a influência da concentração de portadores de carga excitados considerável no tempo de relaxação e na recuperação das mudanças induzidas nas propriedades ópticas. A alta concentração de portadores de carga fotoexcitados gera rápida relaxação energética dos elétrons e recuperação dos efeitos ópticos não lineares. Além disso, os efeitos da difusão dos portadores de carga são estudados através de simulações baseadas no modelo ambipolar. Os resultados da simulação mostram que os efeitos de difusão no GaAs são mais pronunciados no menor comprimento de onda em uma configuração degenerada de "pump-probe".

Palavras-chave: Espectroscopia "pump-probe", refletividade diferencial resolvida no tempo, GaAs, interação elétron-fônon

Abstract

In this thesis, the dynamics of the photoexcited carriers in the bulk GaAs are investigated by a time-resolved differential reflectance method. The setup is mounted in a pump-probe configuration, with tunable wavelength and 100 fs pulse duration. Three bulk GaAs samples, each with different doping levels are considered in this work. The obtained data from the pump-probe spectroscopy reveal that the relaxation time of the excited electrons in the conduction band is highly dependent on the energy of the electrons. A relaxation time around 4 ps is measured for the electrons that are excited by 720 nm while for 800 nm excitation 12 ps relaxation time is recorded for the electrons. The behavior is attributed to different mechanisms of the electron-phonon interaction such that at the low excitation energy Frohlich interaction is dominant while in the higher energy excitation the intervalley scattering plays the principal role in the energy relaxation of the electrons. Besides, GaAs samples with different doping levels are considered to observe the effect of the doping in the dynamics of the electron, particularly the energy relaxation. The data show no considerable changes in the relaxation time of the electrons for different doping levels. However, the influences of the excited carrier concentration are considerable in the relaxation time and the recovery of the induced optical properties changes. The high concentration of the photoexcited carriers gives rise to a faster energy relaxation of the electrons and the recovery of nonlinear optical effects. Moreover, the effects of carrier diffusion are studied by performing simulations based on an ambipolar model. The simulation results show that the diffusion effects in GaAs are more pronounced at shorter wavelength in a degenerate pump-probe setup.

Keywords: Pump-probe spectroscopy, Time-resolved differential reflectivy, GaAs, electron-phonon interaction

Contents

List of Figures

List of Tables

List of Abbreviations

DCC   Departamento de Ciência da Computução

UFJF   Universidade Federal de Juiz de Fora

GaAs   Gallium Arsenide

CW   Continuous Wave

AOM   Acousto-Optic Modulator

SHG   Second Harmonic Generation

LO phonon   Longitudinal Optical Phonon

EO sampling   Electro-Optic Sampling

CARS   Coherent Anti-Stokes Raman Spectroscopy

CEF   Coulomb Enhancement Factor

1 Introduction

Light-matter interaction in semiconductors is an interesting topic in pure physics and technology and has remarkable applications for optoelectronic devices such as solar cells [1]. The dynamics of carriers that are generated by light absorption has a crucial role in transport and efficiency of devices made by semiconductors [2]. Therefore, knowledge of the physical and optical properties of semiconductors helps us to design and fabricate the devices with better performance. As the size of the devices decrease down to micron scale, the times of light-matter interactions become comparable to the lifetime of carriers and thus the interaction effects may possess considerable role in the dynamics of carriers [3]. In this realm, all generated photo-carriers and the atomic lattice interact together and influence on the optical and electronic properties. Carrier- carrier and carrier-phonon interactions are the most important mechanisms that occur at picosecond or sub-picosecond time regime [4]. These interactions lead to changes in the energy and momentum of the excited carriers. For this reason, knowing the underlying mechanisms helps us to understand the dynamics of photo-carriers at the short time after generation.

There are some techniques, called ultrafast optical spectroscopy, to investigate the lifetime and dynamics of the carriers after the onset of generation inside the materials. All the techniques are based on using optical short pulses in a time-resolved mode in order to detect events occurring in short time after excitation. On the other hand, advents in producing of ultrashort pulses in a broad wavelength range give the opportunity to study and observe substantial phenomena influencing on the carrier dynamics [5].

Gallium Arsenide (GaAs) is a semiconductor compound that due to high mobility of electrons and holes and direct energy bandgap is one of the favorite materials in optoelectronics and microelectronics [6]. The photon absorption generates pairs of electron-hole in a GaAs and these those carriers with the doped ones form a plasma with characteristic frequency which is dependent on the carrier density, carrier mass and dielectric constant of the semiconductor [4]. The plasma couples with the lattice vibrations and this coupling has a great role in the transport properties of GaAs [7]. However,

the lifetime of the photo-generated carriers are limited and of order of nanosecond due to electrons and holes recombination thus thy dynamics of these carriers becomes important.

In literature, one can find various studies on ultrafast spectroscopy of GaAs representing effects of different parameters like sample temperature and the excitation energy on the dynamics of carriers in GaAs by different methods [8, 9, 10]. However, we want to perform a systematic and detailed study on the ultrafast dynamics of carriers in GaAs that covers large number of parameters like energy of the carrier energy, density carrier and doping effects in a large temporal window.

In this work, we present our results about the dynamics of carriers in bulk of GaAs through differential reflectivity by a pump-probe setup. Light absorption in GaAs bulk generates a 3D gas of electrons and holes. A 3D gas of electrons are selected because confined electron distributions like 2D gas of electrons introduce a complex energy band, subbands and emergent collective behaviors that make interpretation of results more complicated [11, 12]. The effects of parameters like the excited-carrier concentration, the energy of excited electrons and the doping level of samples on the lifetime of the electrons are studied as well. On this aim, bulk GaAs with three different Si doping concentrations are studied. Also, the effects of energy excitation are observed in the GaAs by changing the pump-probe wavelength to observe the influences of the kinetic energy of electrons in the conduction band on their dynamics. Moreover, the optical properties changes are investigated in various pump intensities, which generate different excited electron concentrations. Besides, we present an ambipolar diffusion model in order to study diffusion effects of electrons and holes inside the semiconductors. In this model, the difference mobility and diffusion constants of electrons and holes are considered [13].

The chapters in this thesis are outlined as the follows. First chapter is an introduction of the work. The second chapter is dedicated to ultrafast spectroscopy, different types of it and also ultrashort pulse generation are discussed. The third chapter is a review about the optical and electronic properties of GaAs. Besides, the light-matter interactions and scattering of carriers with the lattice and carriers at the short time after the carrier generation are explained. In chapter 4, the specifications of the setup that is mounted in our Lab will be given in detail. Also, the setup calibration, technical considerations and

the samples details will be described in that chapter. Finally, the experimental results for the different conditions will be presented along with the analysis and simulation results of ambipolar diffusion in chapter 5.

2 Ultrafast Spectroscopy

2.1 Introduction

Thanks to the progress in producing short-pulsed lasers, high temporal resolution spectroscopy becomes available [14]. Ultrafast spectroscopy refers to techniques that are able to detect events that occur in less than a nanosecond [15]. There is a lot of experimental setups allowing us to perform ultrafast spectroscopy. These spectroscopies can be implemented for all phases of materials from solids to gaseous systems even for biological samples [16].

Resolving every event needs a detector with a time resolution greater than the time of that event. Thus, observing the events happening in the order of femtosecond needs a detector with such high time resolutions. One candidate is the use of streak Cameras with the time resolution that recently approach around 10 ps [17]. The expensive cost of the apparatus and low sensibility for the low- level signal made it useful for the very special cases of experiments like time-resolved photoluminescence. There is another technique that allows us to survey dynamics faster than a picosecond called pump-probe technique that will be explained below.

Basically, the pump-probe technique exploits two pulses, one for exciting an event and the second for observing the same event [15]. These excitation events can be electronic modification or structural changes of a material. The setup configurations and related details depend on the phenomena being observed. The wavelengths, intensity, temporal pulse duration, polarization and angular momentum of the pump and probe are the variables in the setup depending on the subject of study. In the following, we introduce some of the ultrafast spectroscopy setups. Also, we will explain the generation of the ultrashort laser pulses, which is the main element of the ultrafast spectroscopy [18].

2.2   Pump-Probe spectroscopy

2.2.1   Time-resolved Pump-probe spectroscopy

Time-resolved pump-probe spectroscopy is a well-known method to study the ultrafast dynamics of condensed matter, from the solid state like metal and semiconductor to biological and soft matter materials [19, 20]. The contactless measurement is a practical advantage of this method. Basically, this method consists of two short pulse trains with variable temporal delay such that one excites the sample and the other probes optical modification of it [15, 18]. In a simple mode, wavelengths of the pump and probe are the
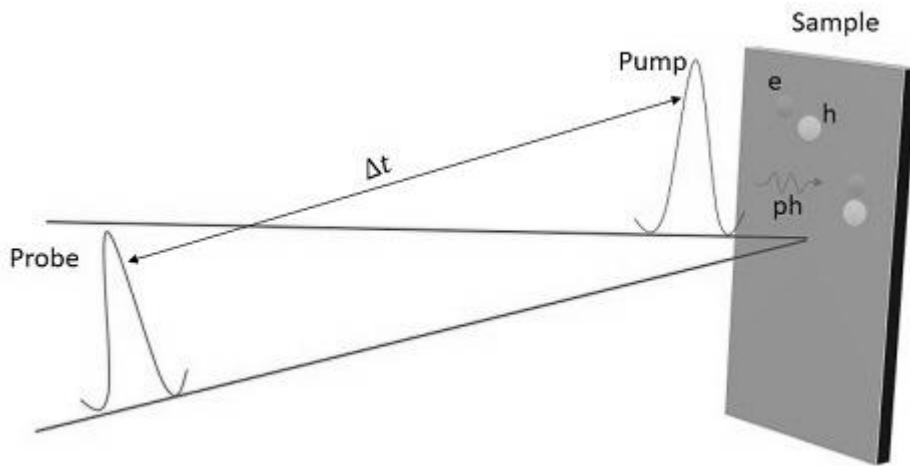
Figure 2.1: Schematic of a non-collinear pump-probe configuration configuration. A small angle and a temporal delay between the pump and probe are represented in this figure. Generation of pairs of electron-hole and induced phonons are the results of photon absorption.

same which is called degenerate pump-probe spectroscopy [21]. The optical properties variations made by the pump can be monitored by the probe in reflection or transmission modes. The major contribution of these variations come from changes in refractive index after excitation [22]. The main characteristic of the degenerate pump-probe spectroscopy is that the probe beam detects the optical changes in the same energy level of the excited electron. Non-degenerate pump-probe in which the synchronized pump and probe have different wavelengths gives more details about the dynamics of carriers at different levels of energy and reveal nonlinear optical properties like two-photon absorption [23, 21]. For

example, the population evolution of the electrons in bulk GaAs is studied independent of the hole dynamics using a non-degenerate pump-probe spectroscopy where a pump beam excites the electrons from the heavy hole and light hole band and a probe beam with higher energy (enough energy to excite electrons from the split-off band into the same states in the conduction where are populated already by the excited electrons) probes only the electron population because no holes are generated by the pump in the split-off band [24]. Not only electronic modifications in short time are detected by the pump-probe method, even the lattice modifications such excited phonon due to the light absorption can be observed via this method [25]. Excitation and dynamics of acoustic phonon in solids can be studied by this technique as well [25, 26]. The non-collinear pump-probe which is shown in Figure 2.1 is the most common arrangement of this kind of setup, while a collinear configuration is useful to investigate waveguide performance where one needs to inject the beams in the same direction [27]. Since the light propagation inside the materials with specific applications like waveguides or amplifiers is highly important, the process of pump-probe implementation is different such that the spatial and temporal variation of the optical properties of the medium along with the propagating light becomes the main subject of the study [28]. To this aim, heterodyne and interferometry methods are utilized to detect these induced changes [28, 29]. In another configuration, a continuous probe and a monochromator are used to measure the optical modification in a vast range of energy in a fixed time delay between the pump and probe beams [30]. The pump-probe technique can be used in Raman configuration to study time-resolved vibrational or electronic Raman structure [31]. The time-resolved electro-sampling, as well, is another technique which is performed with a pump-probe setup [32]. As it will be explained in detail later, one can determine the induced electro-optic effects made by the pump through the monitoring of the probe polarization variation after reflection of transmission from a sample.

2.2.2 Four-wave mixing spectroscopy

Four-wave mixing (FWM) is a nonlinear effect that is referred to the coherent effects made by short pulses absorption in a substance [33]. Actually, the interference of two or three beams in a phase-matched condition makes a nonlinear effect called self-diffraction

inside the material. Self-diffraction is a phenomena in which writing and reading of a grating which is made by the input beams occurs simultaneously [34]. In other words, the resultant interference pattern modulates the refraction index of the material spatially with the same form and finally the grating diffracts one of the input beams. The monitoring intensity of the diffracted beam, which is considered as a new beam by the time, is the principal part of FWM spectroscopy. In fact, the generation of the new beam is the consequence of energy and momentum conservation law and the nonlinear susceptibility of a material [35]. This technique allows us to study the excited coherent effects after light
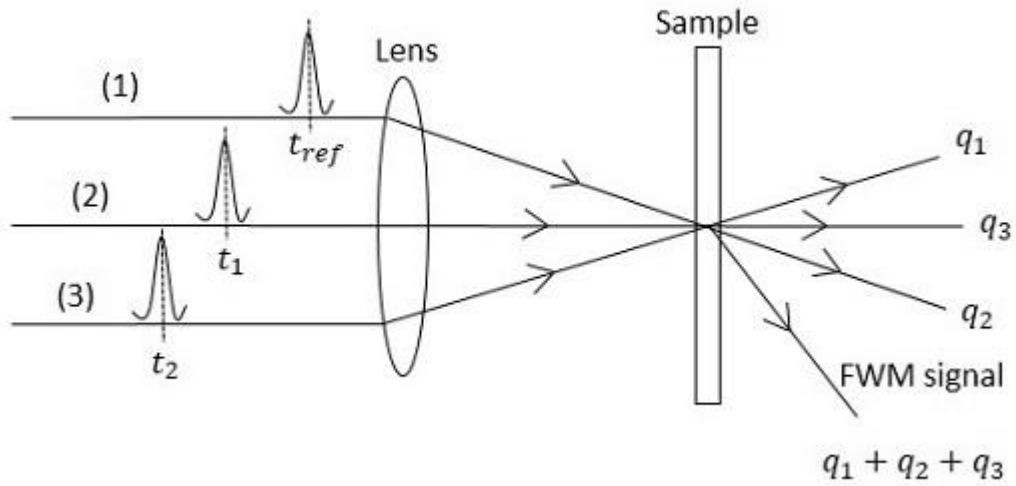
Figure 2.2: Scheme of the FWM setup. Three pulses in a phase matched condition make fourth beam due to the optical nonlinear effect in a sample [15].

absorption [36]. Indeed, the formation of the grating is due to a superposition of the input beams in the sample and then disappears after a characteristic time [15]. According to this model, this technique enables us to study the other coherent systems. For example, excitons are elementary particles with a dephasing times which can be measured by this coherent spectroscopic technique [37]. The short pulsed beams in this experiment allow us to control the temporal sequence and delay between them to monitor the dynamics of this effect. As shown in figure 2.2, the beams 1 and 2 make the coherent states and then the beam 3 with delay time hits the sample as a probe. A portion of the beam 3 is diffracted and recorded by a photodetector. The direction of the diffracted pulses is determined by the phase-matching condition $q_{FWM} = q_1 + q_2 + q_3$ where q_{FWM} is

diffracted pulse wavevector, q_1, q_2 and q_3 wavevectors of first, second and third pulses, respectively. The dynamics of self-diffracted signal unveil information about the dephasing of the coherent polarization made by first and second beams such that intensity of the diffracted beam determines the presence and efficiency of transient grating. This method is called the degenerate FWM, if this technique is performed by a laser source and using some beamsplitters to make different beamlines. Otherwise, an OPO laser is needed to produce beamlines with different wavelengths to perform a non-degenerate FWM spectroscopy. The elaborated configuration of FWM, called multidimensional coherent spectroscopy, is developed recently to study inhomogeneous broadened ensemble of carriers in time and frequency domain simultaneously [38].

2.2.3 Optical pump - THz probe Spectroscopy

The optical pump-probe method investigates carrier occupation in energy range that includes interband transition which is in order of visible and near-infrared light. Whereas, the optical pump-THz probe directly measures the intraband transition of the electrons in the conduction band due to the energy range of THz waves and, therefore, provides a good insight into the conductivity of condensed matter [39]. The response of the carriers to the EM pulses, regardless of the their energy, in the conduction band depends on the concentration and energy distribution of the carriers in those energy states that are being occupied by the photoexcited electrons. [40]. Also, the THz probe enables us to study the low energy excitons like unbound electron-hole pairs and many-body effects that appeared at the low temperatures or the confined states in materials [41]. Technically, the THz waves, which are the probe beam, are generated by the principal optical beam (can be considered the pump) [42]. As shown in Figure 2.3, a cavity is mounted in the pump arm with a THz emitter, in order to generate and amplify the THz waves. Then, the response of the sample, which is placed inside the cavity, to the THz beam can be detected with the optical beam (probe). The transmitted THz and optical beam recombine at the sensor surface where the THz waves induce the electro-optic effect. The induced electro-optic effect in the sensor changes the refractive index along two different directions. This change can be observed by measuring each polarization component(two perpendicular
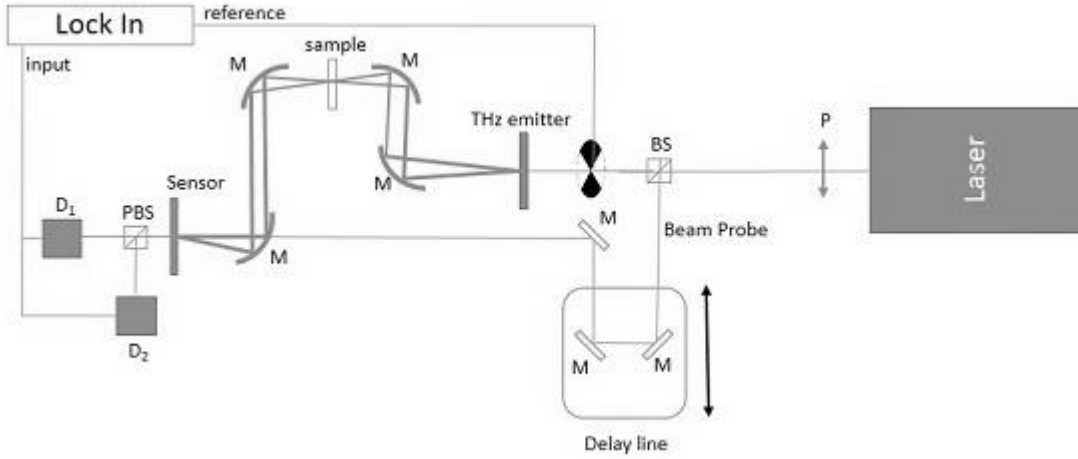
Figure 2.3: Scheme of optical pump - THz probe. In this image M: mirror, BS: beam splitter, PBS: polarization beam splitter, D: detector, P: polarizer. [42]

directions) of the transmitted optical probe. The separated components are provided by a polarization beam splitter and the intensities are recorded with two balanced detectors. Often a portion of the pump beam is sent directly in the cavity to excite the sample. By this method one can study the response of the excited electrons respect to the THz in the sample. A comprehensive information about generation, detection and applications of THz spectroscopy is given by T. Ozaki in the following paper [43].

2.2.4 Electro-Optic Sampling

This method enables us to observe the electro-optic (EO) effects that are induced by pump beam. Indeed, the pump beam changes refractive index in two directions, ordinary and extraordinary, for materials with large EO coefficient like GaAs which can be seen by the probe beam [44]. For example, the induced refractive index changes along two different crystal orientation ($[0\overline{11}]$ and $[0\overline{1}1]$) for GaAs are given by :

$$n_\perp - n_\| = n_0^3 r_{41} E_z, \tag{2.1}$$

where n_0 is isotropic refractive index, r_{41} the electro-optic coefficient and E_z the longitudinal electric surface field. When a polar semiconductor like GaAs is pumped with a short optical pulse, a transient screening and consequently a modulation with LO phonon frequency occur for the surface field [32]. Therefore, according to equation 2.1, one should

observe a modulated $n_\perp - n_\parallel$ value with LO phonon frequency. Thus, this detection manner is a useful technique to detect those optical phonons which are generated at surface or interface of semiconductors provided by the time resolution of pump-probe setup is less than the period time of the phonons [45]. For this aim, the probe beam after transmission or reflection from the sample passes through a polarization beam splitter to separate the probe into two orthogonal polarization components as shown in Figure 2.4. Each polar-
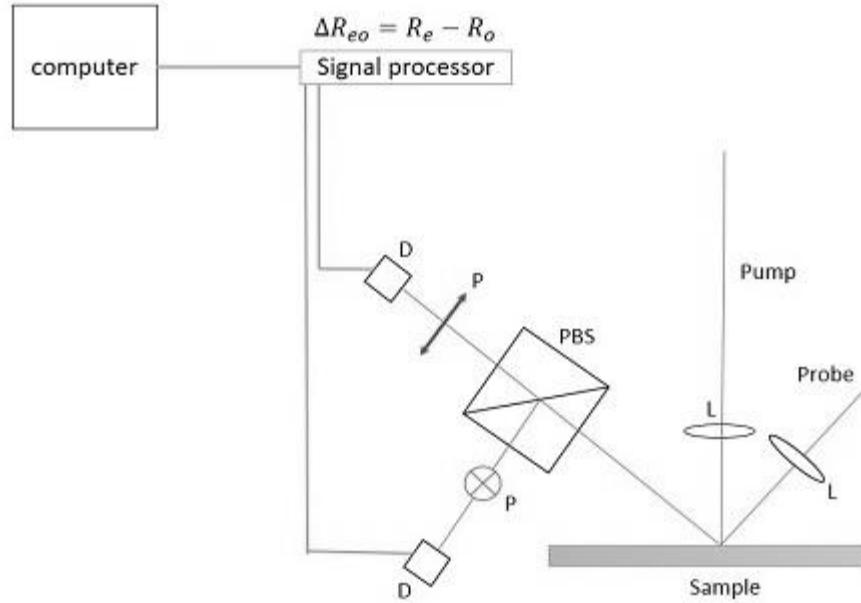
Figure 2.4: Scheme of the EO sampling. L is lens, P polarization direction, PBS polarization beam splitter and D detector. The cross and arrow after the PBS show the direction of the electric field.

ization intensity is measured by a detector and eventually subtracted from each other to approach to ΔR_{eo} value. Most often, the evolution of the relative value$\left(\frac{\Delta R_{eo}}{R}\right)$ gives information about the lifetime, frequency and dynamics of the Phonons. Also, the interface effects between different layers of heterostructures which is a crucial parameter in electronic performance of these devices can be studied with electro-optic sampling. Generation of carriers in semiconductors modifies the interface effect by inducing changes in the electric field at the surface or interface of semiconductors [46, 47].

2.2.5   Photoemission

This technique basically is as same as the above methods except that the probe wavelength is in the UV and X-ray region. Generation of short pulses with short wavelengths needs the high harmonic generation or the synchrotron facilities [48, 49]. Photoemission method
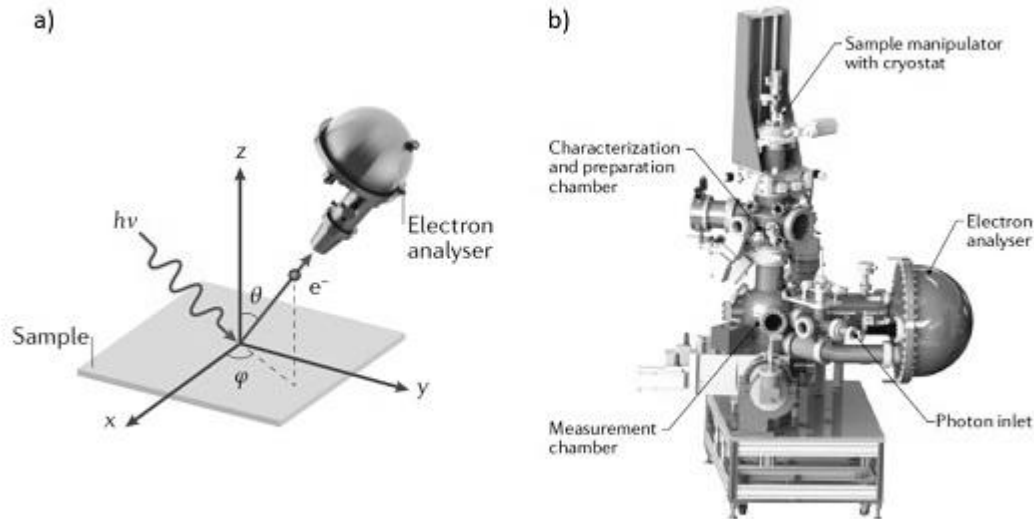
Figure 2.5: a) The illustration of the photoemission after the photon absorption and escaping electron from the surface sample and b) an actual system ARPES includes electron analyzer and some tools for sample manipulation [50]. The beams are not shown in this figure.

is based on measurement of the energy and momentum of the escaped electrons from the sample surface by the high energy photon absorption. In a pump-probe configuration, the electrons usually are subject of the study that are already excited in the conduction band by a pump beam and then are removed by a high energy probe beam. The time between the pump and probe (the high energy beam) is controlled to observe the dynamics of the emitted photoelectrons. This technique are performed in two different methods called Angle-Resolved Photoemission Spectroscopy (ARPES), shown in Figure 2.5 and Time-Resolved Photoemission Electron Microscopy (TR-PEEM) [50, 51]. The main difference difference between these two methods is ARPES gives the electron information in the momentum domain while the PEEM results are represented in the space domain. These methods give extremely valuable information about the band energy and the dynamics of electrons therein, in an intuitive presentation.

2.2.6 Streak Camera

Streak camera is an equipment to record a time-resolved signal directly rather than using pump-probe setup [52]. The technique has single-shot measurement advantage compared to pump-probe method in which one needs to take average over large number of measurements [53]. This apparatus can be utilized for different setups like photoluminescence, Raman and coherent anti-stokes Raman spectroscopy (CARS) [54, 55]. However, high cost, small collection photon area and sophisticated calibration (triggering with small portion of the input beam) are main disadvantages of streak cameras [56]. A streak cam-
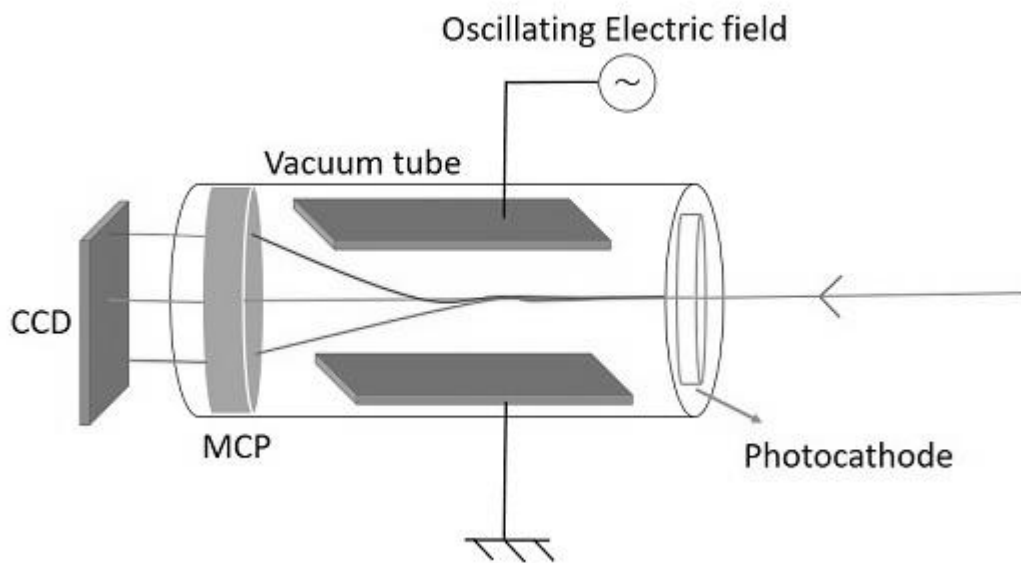
Figure 2.6: Scheme of streak camera. MCP: Micro-Channel Plate [57]. The beam enters inside the tube and absorb with the photocathode. The resultant electron beam lines from the photocathode are deflected by the oscillating electric field and recorded by the MCP and CCD.

era consists of a photocathode which transforms the absorption light to free electrons inside a vacuum tube. An electric field is applied to the tube, as shown in Figure 2.6, to separate electrons according to the time and energy. Those electrons hit to a phosphor screen to capture the data, such that each point at the screen is associated to a specific time. This technique is much faster than the fastest photodetectors have been built so far due to its detection mechanism. This is a useful method to observe the dephasing time of coherent states in semiconductor after excitation [15].

However, developing a appropriate pump-probe setup depends on the sample

and phenomena being studied. For example, using a broadband probe pulse allows us to detect a wide band of molecule transitions while the system is excited by short pulses [58]. Another example is the use beams having orbital angular momentum (OAM) in order to excite and study the excitations with specific spin [59]. Generally, in this technique one uses beams with Laguerre- Gaussian intensity profile, carrying different values of AOM that enables us to excite those transitions that were forbidden in pump-probe with the Gaussian mode laser [60]. Excitation with two pulses is another technique to manipulate or form different quasi-particles to make a pre-excited systems and study dynamics of possible coupling modes between elementary particles [61, 62].

2.3   How to make temporal delay between pulses

Technically, besides having short pulses, making temporal delay between two beams is a challenge in this type of setups. Here we mention two methods to implement delay time between two beams.

Mechanical base delay time

This method is based on exploiting two temporarily separated pulses such that the first pulse excites one sample and then the second pulse after a while probe modifications [18]. This delay time, made by a translation stage, moving alongside one arm and makes an optical path difference. Another way to make a delay time is using a shaker in one arm, pump or probe, to oscillate and cover a specific distance associated to a temporal window [63]. Signals are recorded for each period of the shaker oscillation and then after a short time a large number of data can be averaged and this increases the signal to noise instead of using modulation and Lock-In amplifier.

Electronic base delay time

Asynchronous optical sampling is a method in which instead of using a mechanical translation stage, an electronics system is exploited to make delay time [64, 65]. To this aim, firstly, two lasers should be synchronized and then by an electronic system make an offset repetition rate between them to make delay time. In this way, errors made by the move-

ments of a mechanical system would be eliminated. However, it is quite complicated and expensive to perform because it needs to synchronize **two femtosecond oscillators** and a triggering process for data acquisition [66].

2.4   How to produce ultrashort pulses

In this section, we are considering the formation of ultrashort pulses in the laser. Pumping source, cavity and gain medium are the main parts of a laser. In a classical prospective, light is considered like to be a wave propagating inside a cavity, between two mirrors, makes standing waves with discrete wavelength or longitudinal modes. This approach is as same as an oscillating string between two nodes which can oscillate only with specific frequencies. Superposition of waves with different frequencies inside the resonator with the length L results in the formation of net EM wave with the frequencies $\nu = m\frac{C}{2L}$, in which m is the positive integer number and C is the velocity of light in vacuum [67]. In
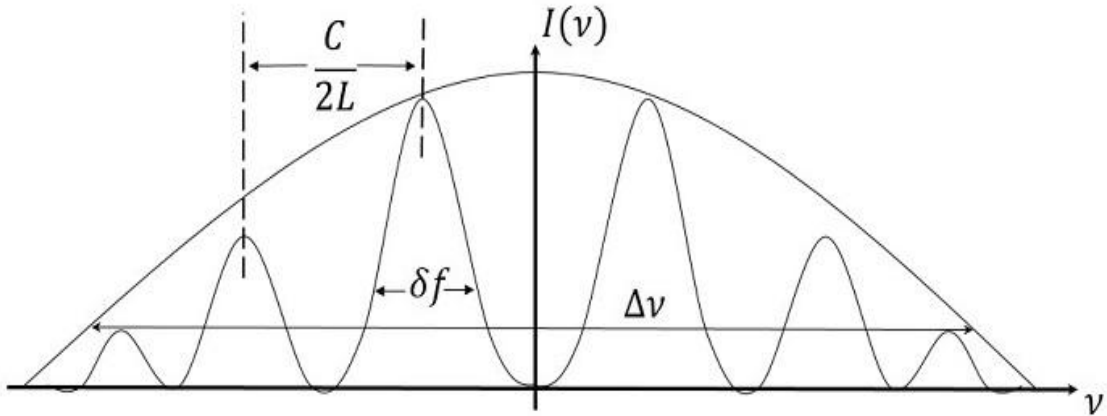
Figure 2.7: Frequency of domain of laser beam containing a series of frequencies with the total bandwidth $\Delta\nu$, the $\frac{C}{2L}$ difference between two consecutive frequencies and a bandwidth δf for each frequency. A Gaussian gain distribution changes weight of each frequency [68].

order to resolve the frequencies contributing in the final beam, one can use the Fourier transform of the laser intensity, illustrated in Figure 2.7. The peaks of the spectrum represent the light frequencies such as the adjacent frequencies have $\frac{C}{2L}$ space between them. δf is bandwidth of a frequency and depends on the finesse of the cavity and $\Delta\nu$

is the gain bandwidth of the laser which is dependent of the medium of the laser. Solid-

state, dye and semiconductor lasers have a relative large bandwidth which is proper for

producing the short pulses of order of picoseconds or less. [67].
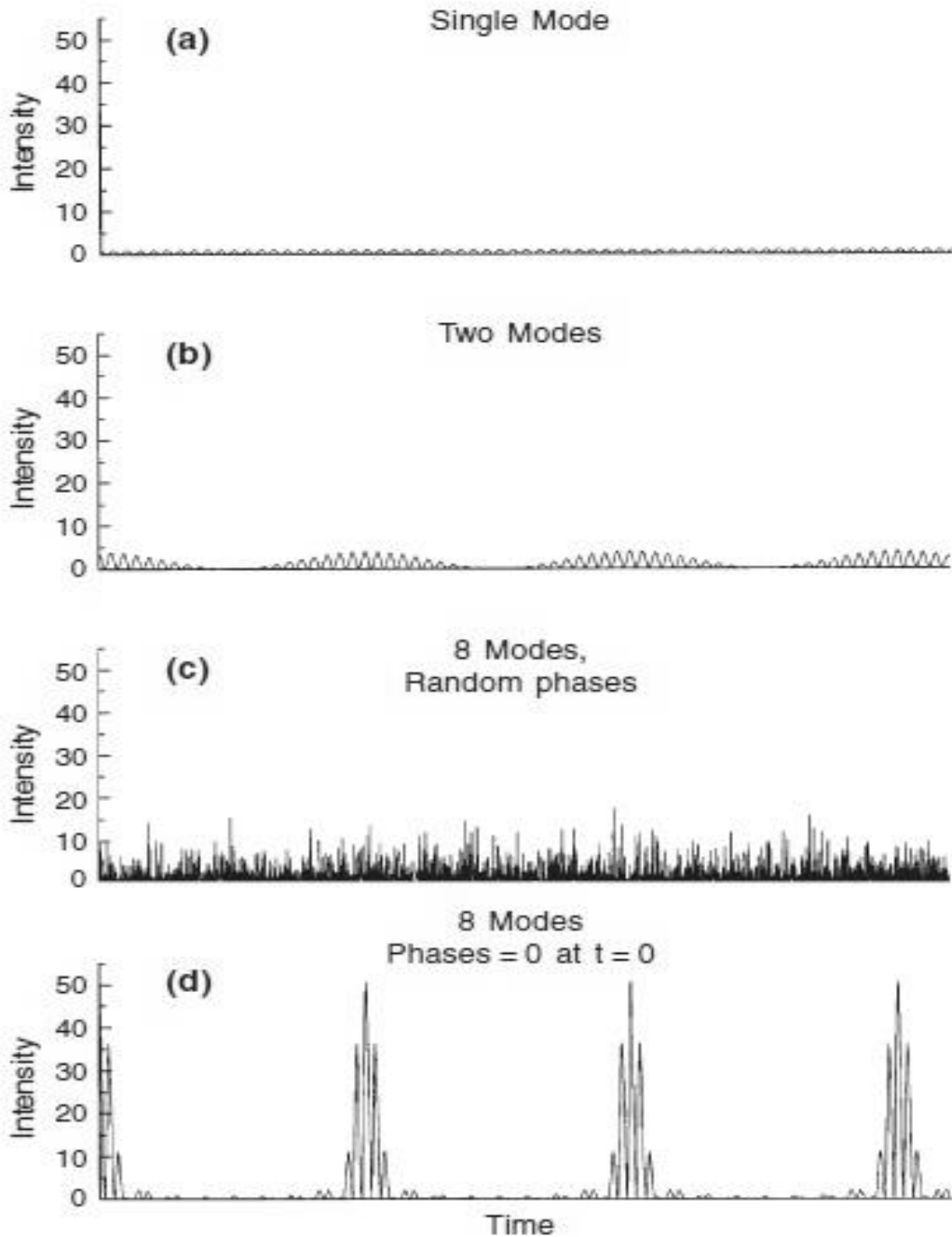
Figure 2.8: A schematic from effects of superposition the modes and the phase relation
between them. All the plots are in the time domain for a) a mode, b) two modes, c) 8
modes with undefined phase relation and d) superposition of 8 modes with well-defined
phase difference between them [67]

.

Now, suppose that we have a spectrum as shown in Figure 2.7, with large number

of frequencies. Superposition of these longitudinal modes make wave packs with short time

duration. However, in order to construct a short pulse, relative phases between the modes should be constant. Otherwise, the undefined phase between them gives rise a randomness behavior of the light intensity in the time domain and the pulsed beam will not be formed as represented in Figure 2.8.C.

It should be noted that the uncertainty principle limits the pulse time duration by relation $\Delta t \Delta \nu \geq \frac{1}{2}$ meaning that the shortening the pulse duration increases the bandwidth frequency respectively. In other words, to obtain the shortest possible pulse duration, the bandwidth should be enough large such that

$$\Delta t_{min} = \frac{1}{\Delta \nu}, \tag{2.2}$$

where Δt_{min} is the minimum achievable duration time. The temporal broadening of the pulses due to the dispersion of the group velocity in all components of the cavity is neglected in relation 2.2.

In the following we will describe briefly the methods for producing a pulsed beam.

2.4.1   Q-switching

Q-switching is a technique to increase the output power of a laser as the principal requirement for pulsed beam generation. The order of the magnitude power of a typical q-switched laser reaches hundreds of megawatts per pulse which is considerably greater than a CW laser power due to the high population inversions that are reached by Q-switching [69]. The technique is based on switching of the quality factor of the cavity called Q factor [68]. Q-factor parameter is expressed as the ratio of stored energy over the energy lost of a pulse in one cycle of oscillation times 2π in the cavity. This switching is made possible by introducing a modulator inside the cavity in order to modulate the losses of the cavity. When the shutter is off, the cavity stores more energy and then, when it is opened, the cavity releases huge amount of stored energy. Technically, there are many different ways to perform the Q-switching which can be generally, categorized into two main methods: Active Q-switching and Passive Q-switching. In active Q-switching, an external force is applied to a modulator inside the cavity to make Q-switching. Whereas,

in the passive method, one can use a nonlinear optical material, like saturable absorbers, to produce Q-switching.

2.4.2 Mode-locking

Suppose a laser emission containing a large number of longitudinal modes which provided by the resonator. Such pulses in the Fourier transformed domain have a large number of peaks associated with the frequencies. The mode-locking term comes from the idea stating that keeping the relative phases between the longitudinal modes constant to give an intensified intensity of the output laser [67, 68]. The mode-locking method enables us to generate pulses with time duration less than the round trip time of a pulse in the cavity. Therefore, once the modes are locked together, the larger the number of locked modes, the greater the pulse intensity and narrower the pulse duration. The locking process can be performed with two different methods.

Active mode-locking

In this way, a modulator is utilized inside the cavity to module the cavity losses. Basically, an Acousto-optic crystal which is driven at a radio frequency (RF) is placed inside the cavity. The modulated refractive index of the crystal deflects the light passing through it and induces a modulated loss in the cavity [70]. The care should be taken to the RF value
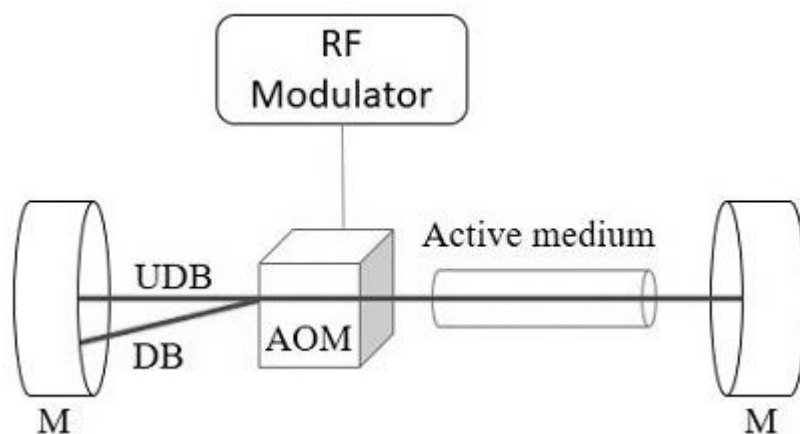
Figure 2.9: Schematic of modelocking in a cavity by an AOM (Acousto-optic modulator), M represents a mirror of cavity. The deflected and undeflected beam are DB and UDB, respectively.

and the repetition rate of the laser must be the same. However, the complexity of the accurate performance made the active mode-locking not a suitable method for producing pulses shorter than 500 fs time duration [18].

Passive mode-locking

In Passive mode-locking, one uses a Nonlinear crystal inside the cavity in order to utilize the optical nonlinearities of the crystal to generate intense mode-locked pulses. So far, four methods are introduced to perform the passive mode-locking [67, 68]. Kerr mode-locking is one of the these techniques, exploiting a Kerr crystal, a nonlinear crystal behaves like lens for intense beams due to self-focusing effect [71]. By a slit and an intracavity aperture in a proper position in the cavity, the separation of the mode-locked beam is possible as shown in figure 2.10 [69]. Indeed the crystal act like a pulse synchronizer such that sunchronization occurs in a cavity when two counterpropagating pulses arrive in the same time in the crystal [72] .The mode-locked beam has smaller spot size compared to non mode-locked one at the slit position. Fast saturable absorber, slow saturable absorber
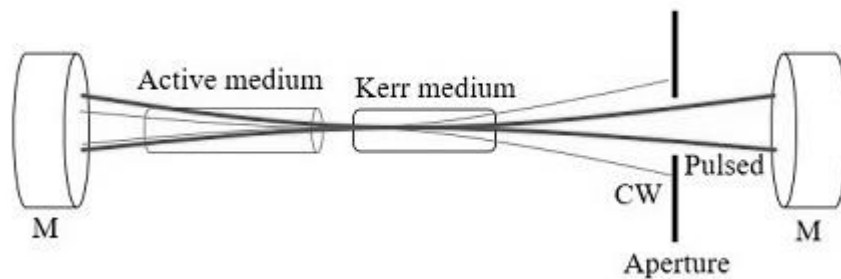
Figure 2.10: Kerr effect principle in a mode-locked cavity. Kerr medium converges the propagating light to a small diameter.

and additive pulse mode-locking are the other techniques to generate ultrashort pulses [68].

The wavelength selection is done by a sequence of prisms and a slit. The prisms disperse the pulses spatially and the slit is placed in a proper position to select the favorite wavelength.

Mode-locking and Q-switch methods provide EM fields coherently in a pulsed mode. Of course, design and fabricating ultrashort laser pulses depends on parameters

like the cavity size, technical details about the electric power and cooling system which is not, anyway, the main subject of this thesis.

3 Optical Properties of GaAs

3.1   Introduction

In this section we will describe the electronic, optical and atomic structure of GaAs that is the principal material used in this study. Then, a discussion about possible interactions between the elementary particles inside a semiconductor will be given. These interactions, carrier-carrier scattering and carrier-phonon scattering, have the pivotal roles in the dynamics of physical properties of sample. Also, we will address the question that what parameters would be measured in a pump-probe differential reflectivity and how the mentioned interactions affect the obtained parameters.

Gallium arsenide (GaAs) is a semiconductor compound of the III-V semiconductor group [73]. It is a direct band gap, non-centrosymmetric semiconductor with a zinc-blende structure as shown in 3.1. The high mobility and the direct band gap made the GaAs still as a good candidate for optoelectronics and THz applications [74, 75, 76]. Efficiency up to 30% is recorded for solar cells with a single junction made by GaAs [77, 78] and for multiple junction cells it reaches around 40% [79, 80]. Also, due to the large second-order susceptibility of GaAs, it has been used for nonlinear optical generation. For example, the bulk nonlinearity of GaAs has be used to realize relatively efficient intra-cavity sum frequency generation [81, 82]. Since the LO-phonon frequency of GaAs is around 10 THz, it can be a good candidate to generate THz waves to study molecular vibrations, spin waves and so on [83]. Also, the thin film of GaAs upon the ultrafast excitation can emit THz pulses [84]. The capability of being doped with other elements like Si and Be and the enhancement of electric properties make GaAs useful for electronics applications as well. Even, a semi-insulating behavior is observed in GaAs with resistivity higher than 10^6 ohm cm showing the capability of GaAs to have different electronic properties [86]. Moreover, the capability of forming GaAs with different geometries like nanowires, strained layers, quantum dots, thin films and the rolled sheet of GaAs gives us the potential to engineer the properties of GaAs to a tailored design [87, 88, 89]. Even
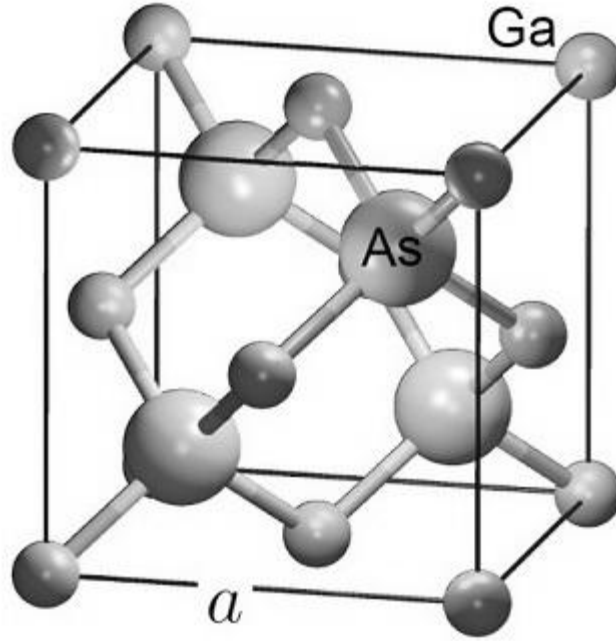
Figure 3.1: Zinc-blende structure of GaAs [85].

though, the doping of GaAs with a spatial modulated pattern is possible, introducing new subbands and the related resonance [90].

Vibrational modes in GaAs, like other binary compound such as InP and GaN, are divided into two branches optical and acoustic phonons due to presence of two atoms in unit cell of GaAs structure [73]. Both branches of phonons have significant role in dynamics of carriers in GaAs, which will be discussed in detail in this work [91].

In this work the optical features of the GaAs are of our interests after absorption of photon. Basically, semiconductors absorb a photon, if its energy is greater than the band gap energy, leading to formation of a pair of electron and hole in conduction and valence bands, respectively. The presence of electrons and holes can modify the refractive index of the GaAs. Therefore, knowing the dynamics of electrons and holes is important to understand the dynamics of the refractive index. The dynamics is strongly dependent on the band structure and phonon structure of the semiconductor. Interactions between electrons and holes with the phonons are important in this context. Thus knowing the electronics and phononic structure is essential for our purpose.

The figure 3.2 illustrates a schematic of the band structure of the GaAs. Of
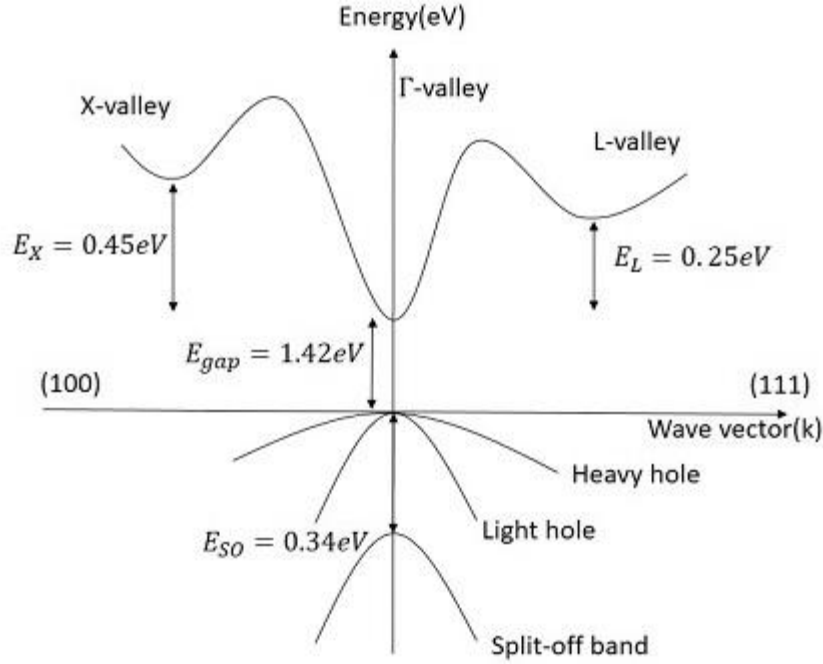
Figure 3.2: Band structure of GaAs at room temperature. The curvature of the bands are not precisely plotted [73].

course, the detailed structure is more complex and obtainable with numerical methods like k.p which is an approximated semi-empirical approach for calculating the band structure based on perturbation theory [92]. However, we want to mention some important features of the band structure of the GaAs. The curvature of the bands are inversely dependent on the effective mass of the electrons or holes. The effective masses of the electrons and holes are listed in table 3.1. There are three different energy bands in the valence band.

Table 3.1: Effective mass of carriers in different positions in band structure of the GaAs (m_0 is the free electron mass) [32].

Valley	Mass
Γ	$0.063m_0$
L	$0.11m_0$
X	$0.27m_0$
Light hole	$0.08m_0$
Heavy hole	$0.5m_0$
Split-off hole	$0.15m_0$

Two of them are degenerated in $k = 0$ which are the light hole and heavy hole bands. The other parameter that differentiates the two bands is the total angular momentum (m_j) such that for the heavy hole and light hole we have $m_j = \frac{3}{2}, \frac{1}{2}$, respectively [59]. Another energy band is the split-off band resulted from the spin-orbit interaction in the

GaAs. The interaction breaks degeneracy in $k = 0$ and lowers the energy of the valence band. The presence of other valleys in the conduction band showing that there are other transitions that are able to excite the electrons from the valence band to the conduction. On the other hand, the curvature of the valleys has an inverse relation with the density of state at each point. Since the curvatures of the L and X points are less than Γ point, then the electron populations in those points are more probable provided that the excitation have enough energy to allow these transitions to occur [32].
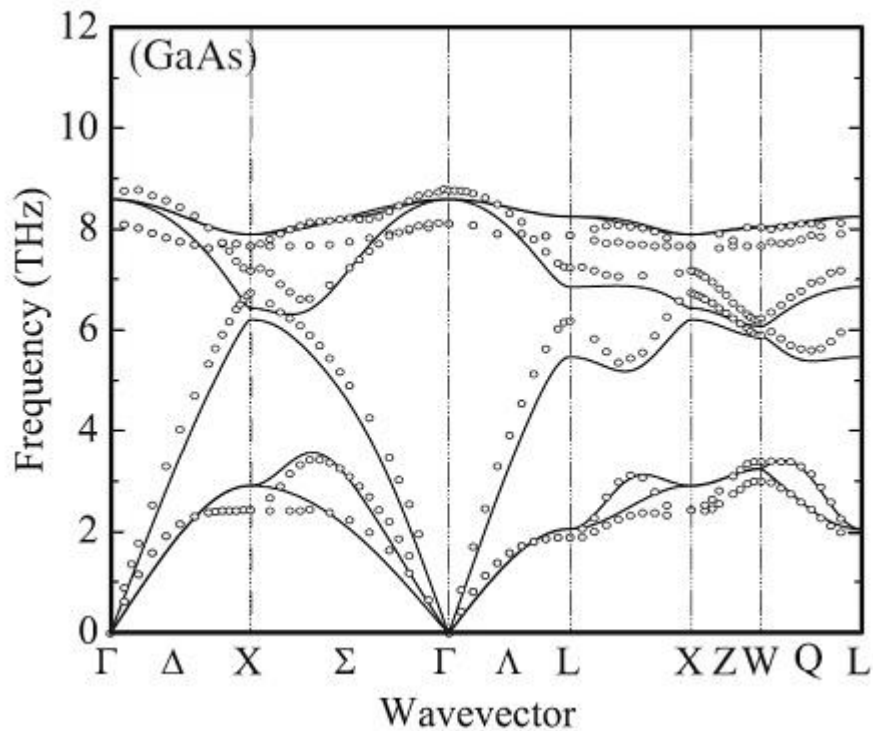
Figure 3.3: The lines present phonon band structure calculated using a two-parameter Keating model for GaAs [93]. Open circles are experimental data from Droner and Strauch [94].

To survey the phonon structure of the GaAs, we need the phonon dispersion relation of GaAs which is plotted in Figure 3.3 in which the optical branches have more energy compared to the acoustic ones [95]. The energy difference between the two branches is more obvious in $k = 0$ or Γ point where is called the zone-center. While the phonons at the wavenumbers X or L, called zone-edge phonons, have the minimum energy difference between two branches. The edge and center terms are referred to the center and edge of the Brillouin zone [93].

Now, we will explain the dynamics of carriers in the GaAs governed by the inter-

actions. Since our investigation is about the dynamics of the excited carriers, it is worth to propose the temporal regimes after the excitation in which certain mechanisms and interactions are probable to occur. Therefore, we introduce four regime time based on possible interactions. More details about the interactions are available in the next section.

3.1.1 Coherent Regime

A very short time after excitation (around 10 fs to 100 fs) coherent effects appear [15]. The coherency comes from a well-defined phase relationship between the ground states and excited states made by a laser beam [96]. Interference of these two states can generate macroscopic effects such as a transient grating in semiconductors [36]. The resultant grating is responsible for the FWM effects that explained in section 2.2.2. Dephasing of such a grating determines decoherence time in semiconductors. Coherency in semiconductors is destroyed by collisions between carriers. Therefore, we define coherent regime from excitation time until decoherency occurs. The resultant effects in this regime can be detected by nonlinear spectroscopy methods due to the distribution of oscillator frequencies called inhomogeneous broadening [96, 97]. This broadening causes suppressing the coherent effects in linear spectroscopy [98]. Some of the important methods to measure the quantum effects are multidimensional spectroscopies such as two-dimensional electronic spectroscopy (2DEG), two-dimensional fluoroscence spectroscopy and coherent four-dimensional electronic Raman spectroscopy [99, 100, 101].

3.1.2 Non-thermal regime

After the coherent regime, a non-thermal distribution occurs for carriers in which temperature is not defined [102]. In this time regime, carrier-carrier and carrier-phonon scattering happen in the sample to attain to a new equilibrium. Intervalley and intravalley scatterings are other mechanisms contributing to relaxation carriers and thermal distribution. In some cases the carriers remain in non-equilibrium states and release their energy where carrier- longitudinal optical phonon interaction is stronger than carrier-carrier interaction like GaN [103]. Whereas in GaAs, though with strong carrier-LO phonon, the carriers approach to an equilibrium distribution due to carrier-carrier scattering.

3.1.3 Thermalized carrier distribution

After the formation of a thermalized distribution of carriers, called hot carriers, the interaction of carriers and phonons becomes more effective to reach to a common temperature between the carriers and lattice [15]. This interaction involves all branches of phonon as acoustic phonons. This time regime is around 100 ps.

3.1.4 Recombination regime

After the equilibrium carriers and lattice and defining a common temperature between them, the excess electrons and holes begin to recombine together. This recombination can be radiative or non-radiative and finally, the system reaches total equilibrium until next photon absorption. Normally, it occurs in nanosecond regime after excitation [104].

3.2 Interactions

Formation of excited particles and quasi-particles are highly dependent of physical conditions, e.g. temperature, size and applied electric or magnetic field, of semiconductor. In bulk GaAs, at room temperature and without any applied field, the plasma (including electrons and holes and phonons) is main particles and quasi-particles. The dynamics of the system depends on knowing of the interaction between the mentioned elements. In this section, we will explain two types of interaction between carriers and between carriers and phonons.

3.2.1 Carrier-Carrier Interactions

In a general treatment, carrier-carrier interaction introduces some new phenomena in semiconductors like formation and dephasing of excitons [105, 106], band gap renormalization [107], scattering [108], screening of Coulomb potential between carriers [109] and collisional broadening of states [110]. Theoretically, carrier-carrier interaction can be expressed based on the Coulomb potential. Excitation of a large number of pairs of excited electron and hole form a state of matter called plasma, representing collective behaviors [111, 112]. For a detailed analysis, the density function formalism is needed to investigate

all the mentioned effects which can be seen in the following references [113, 114]. One can consider the plasma as a charged particle surrounded by a cloud of charged particle [112]. This approach is base of many-body theory for explaining a plasma system. However, parameters like sample specifications such as the dimension of GaAs and the sample temperature should be included in a precise analysis.

Scattering between the photoexcited carriers is inelastic which allows them to exchange momenta to attain a new equilibrium distribution. This mechanism called thermalization occurs in less than 100 fs for electrons. The thermalization time depends on the photon energy and density of excitation [115]. Also, owing to the different effective mass of electrons and holes in semiconductors, the themalization time for holes is shorter than the electrons ones and each forms a separated equilibrium distribution with different temperatures and dynamics. There are some experimental reports evaluating the effects of dynamics of electrons and holes separately on the optical properties of the GaAs [116, 117]. In the literature, we observe the simulations and experimental results showing that the temperature of the hole distribution does not change by the time due to vary fast thermalization of holes in semiconductors [24]. Thus, in this work, we will only focus on the interaction of the electrons with other system particles.

The electron-electron (e-e) interaction is highly dependent on the density of state of excited electrons such that the interaction for those electrons with low residual energy in the bottom of the conduction band is the main channel to destroy the coherency after excitation [118]. The e-e scattering rate is much higher than the scattering rate of LO phonon-electron due to the large difference in the masses, proving that the main channel for energy and momentum relaxation is e-e scattering after excitation [119]. In a high concentration of excited electrons, particularly when they have low residual energy, the e-e scattering becomes stronger compared to the electron-phonon interaction. If the excited electrons have enough energy such that they are allowed to transfer to other valleys, LO phonon-electron should be taken into account and becomes of the order of the e-e scattering rate. An increase in temperature can occur by electron-hole recombination which is another event that change the the dynamics of the electrons and holes slightly [120]. To observe such an effect, the energy (or temperature) of electron should be so low to
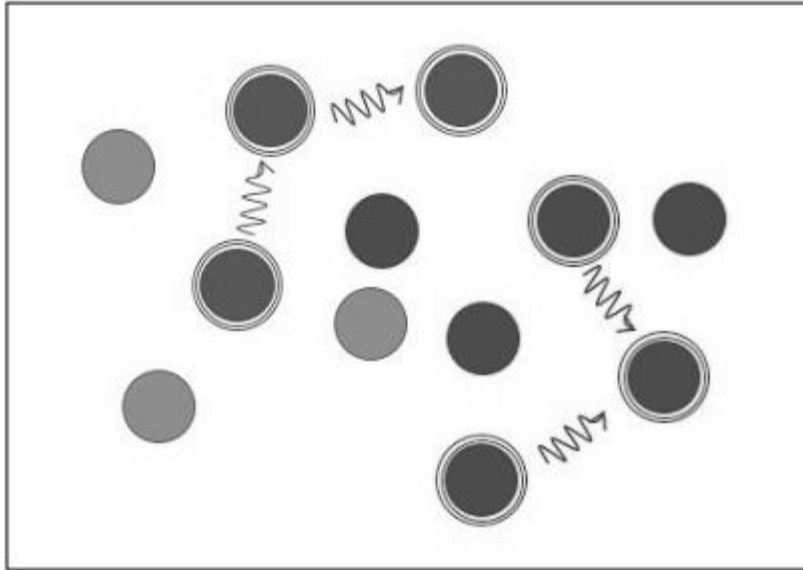
Figure 3.4: Schematic of scattering between electrons (red balls) and holes(blue balls). Initial thermalization occurs between electrons and hole by scattering between them separately.

the LO phonons do not contribute to the relaxation of electrons. However, recombination-induced heating will be ruled out due to the high energy electrons (the excited electrons have energy more then a LO phonon energy from the bottom of the conduction band) that will be studied in this work.

3.2.2   Electron-Phonon interaction

This interaction occurs between these two major components, electrons and phonons. The excited electrons normally after formation of a thermalized distribution begin to interact with the lattice [18, 15]. Generally, the interaction happens through emission or absorption of phonons carrying quanta of energy. The interaction changes the electron states in the conduction band until the electrons and the lattice reach a equilibrium situation. Therefore, the main mechanism of the relaxation of energy by the electron is electron-phonon (e-ph) interaction after the initial thermalization [121]. Excitation of electrons to the conduction band and then their relaxation by phonon emission can be considered as was to generate phonons. The time interaction is reported in a lot of papers and are of order of tens of picosecond [119]. It is found that the physical properties of

sample influnces on e-ph interaction such that the cooling rate of the hot electrons in GaAs quantum wells is much less than the bulk GaAs [122]. It should be noted that energy-loss rate through phonon emission is different for electrons and holes [123].

Phonon Generation

In this section, we briefly describe possible sources of phonons which afterward interact with electron and holes in a sample. A common source of phonons is the electron relaxation in the conduction band [3]. The energy relaxation of electrons rises up the phonon emission incoherently such that the specific phases relation between the emitted phonons are not defined and in turn will lead to the increasing lattice temperature [124]. One of the most common mechanism of coherent phonon generation is transient depletion field screening in doped polar semiconductors [125]. The field, which is the result of the Fermi pinning by doping, is depolarized by the local electric field that is made by pairs of electron-holes after light absorption. The fast depolarization of the surface electric filed triggers coherent phonons inside the sample and can be detected by the electro-optical sampling setup [32]. Other generation methods of coherent phonons are impulsive stimulated Raman scattering and displacive excitation mechanism of coherent phonon which firstly excite the phonons with specific symmetry and secondly the excitation wavelengths should match with electronic resonances of the sample [126, 127, 128]. Ultrafast pulses can make not only the coherent optical phonons but also they are able to excite coherent acoustic phonons by inducing mechanical stress [124, 129].

The e-ph interaction intensity highly depends on the type of involved phonons and their wavenumber, polarity of the lattice and symmetry of the initial and final states. Therefore, one can categorize these interactions as below.

Deformation Potential

Basically, the vibrations of the atomic structure of the lattice induce displacements on the unit cells [130]. Such movements can alter the interatomic potential and consequently change the energy level of the system. In a general form, one can express the Hamiltonian

for this interaction as the following,

$$H_{e-ion}(r_i, \delta R_j) = \sum_j (\frac{\partial H_e}{\partial R_j}).\delta R_j + ..., \tag{3.1}$$

where H is an unknown Hamiltonian of the interaction and R is the coordinate of the unit cells. Interaction amplitude from initial state(k) to the final state by absorption or emission of phonon(q) is given by $\langle k \pm q|H_1|k\rangle$, in which H_1 is the first order of Taylor series of 3.1 expression [131]. Obviously, in a great displacement, we expect that this Hamiltonian increasingly changes the energy levels. Now the question is how to make such a lattice displacement? As explained in carrier-carrier interaction section, photon absorption in semiconductor make an ensemble of electrons and holes and they form a plasma system oscillating with ω_p. Then the the kinetic energy of the plasma or electron gas transfers to the lattice and induces displacement. On the other hand, for having such an interaction considerable, the displacement should be induced by high energy (frequency) acoustic phonons. Low energy acoustic phonons, as can be seen in Figure 3.3, practically do not alter the energy levels of the system due to the very low energy of acoustic phonons in the zone-center. Piezoelectric effect is a well-known consequence of the interaction that occurs in materials that are non-centrosymmetric, leading to a coupling between the electric field and the excited electrons [130]. In piezoelectric materials, applying an oscillating electric field can drive a mechanical vibration and vice versa. It should be noted that zone-edge acoustic phonons are involved in this mechanism. Deformation potential can be induced even with optical phonon that its strength and mechanism of interaction depending on the polarity of the materials are different [15]. Deformation potential in nonpolar materials change the angle or length of a bond whereas in polar material another mechanism occurs that in the following will be described.

Frohlich Interaction

In materials with two atoms in their unit cell, the optical phonons with small wavenumbers induce a macroscopic oscillating polarization, leading a macroscopic field across the matter. The resultant field interacts with the electrons in conduction band and this interaction modifies the energy levels of the system [130]. This interaction is in contrast
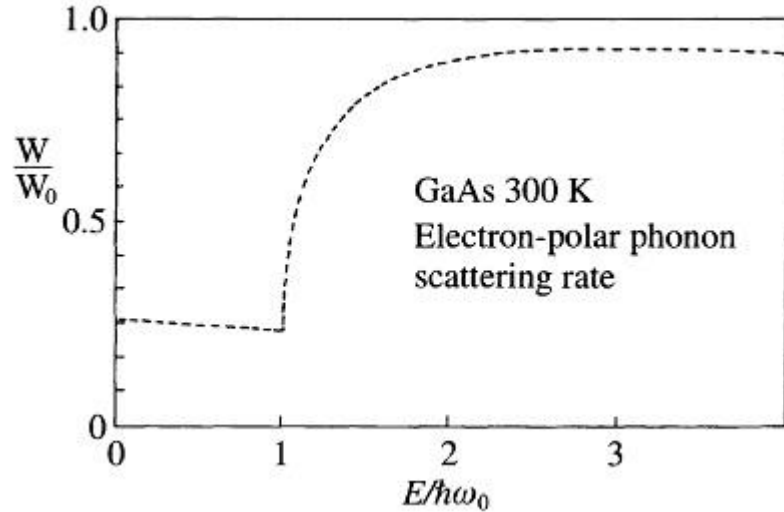
Figure 3.5: The scattering rate of Frohlich interaction versus the energy of the electrons [15].

to the previous case in which the acoustic phonons have a major role in the interactions. This interaction, called Frohlich interaction, is more pronounced in polar semiconductors like GaAs or InP, and thereby exchanges the energy between the electrons and lattice. Frohlich scattering is very important in the dynamics of the excited electrons as an effective channel of releasing their energy [93]. The transition rate of the scattering is given by [15]

$$W(E) = W_0 (\frac{\hbar\omega_{LO}}{E})^{\frac{1}{2}} N(\hbar\omega_{LO}) sinh^{-1}(\frac{E}{\hbar\omega_{LO}}) + [N(\hbar\omega_{LO}) + 1] sinh^{-1}[(\frac{E}{\hbar\omega_{LO}}) - 1] \quad (3.2)$$

and

$$W_0 = \frac{e^2 (2m\hbar\omega_{LO})^{\frac{1}{2}}}{4\pi\hbar^2} (\frac{1}{\epsilon_\infty} - \frac{1}{\epsilon_0}), \quad (3.3)$$

where W(E) is the transition rate of the scattering for those electrons that their energy lie between E and $E + \delta E$ energy interval, W_0 the transition rate for the electrons that are placed in the bottom of the conduction band, N is the phonon occupation number in the frequency ω_{LO} in which ω_{LO} is LO phonon frequency, ϵ_∞ and ϵ_0 the dielectric constants in high and low frequency applied field, e and m the electric charge and mass of electron respectively [15]. The term of $\frac{1}{\epsilon_\infty} - \frac{1}{\epsilon_0}$ in figure 3.3 is related to the polarity of a compound. The value W_0 for GaAs at the temperature 300 K is around 125 $(fs)^{-1}$. Figure 3.5 shows the behavior of expression of formula 3.2 versus $\frac{E}{\hbar\omega_0}$, where $\hbar\omega_0$ is the fundamental

band gap of the GaAs and E energy of the excited electrons. The graph represents the relative scattering rate of the electrons via the Frohlich interaction for different relative energy values demonstrating that for the energies just above the band gap the scattering probability increases drastically. A threshold relative energy is observed around 2 and thereafter a saturation trend occurs. It is turned out that the Frohlich interaction has a considerable growth in a specific energy range and after that it approaches to a constant value. On the other hand, as the Frohlich interaction is based on the Coulombian force and this force in Fourier space has $\frac{1}{q}$ dependency (q is the phonon wavenumber), thus the Frohlich interaction diverges as the q approaches to zero [130]. It means that those phonons with low value of q are more effective in the interaction.

It should be mentioned that the scattering of electrons with acoustic phonons is an elastic or quasi-elastic scattering in which the energy of the electrons remains constant after scattering. Thus, acoustic phonons have an important role in momentum relaxation, while scattering with optical phonons results in relaxation of energy and momentum of electrons. Nevertheless, recently some works show that the better understanding of the dynamics of the electrons needs models involving all types of phonon branches [132, 133].

Intervalley Scattering

Another type of interaction between electrons and phonons is the intervalley scattering in which the electrons are transferred between the conduction band valleys by assistance of phonons. This mechanism has an important role in optical properties of direct band gap semiconductor by the energy and momentum relaxation of hot electrons, transport properties in an indirect band gap semiconductors (like Si and Ge) [130]. Sufficient energy and phonon assistance are the main parameters to occur this scattering. For example, in the GaAs case as it is shown in Figure 3.6, the electrons should have an energy more than 0.25 eV (0.45 eV) in the conduction band to transfer to the L (X) valley. The changing of valley in the conduction band means that the electron change own its position in the molecular orbitals. Whereas releasing energy in the same valley called intravalley scattering can be considered a loosing energy way in the same molecular orbitals, as shown in Figure 3.7a.
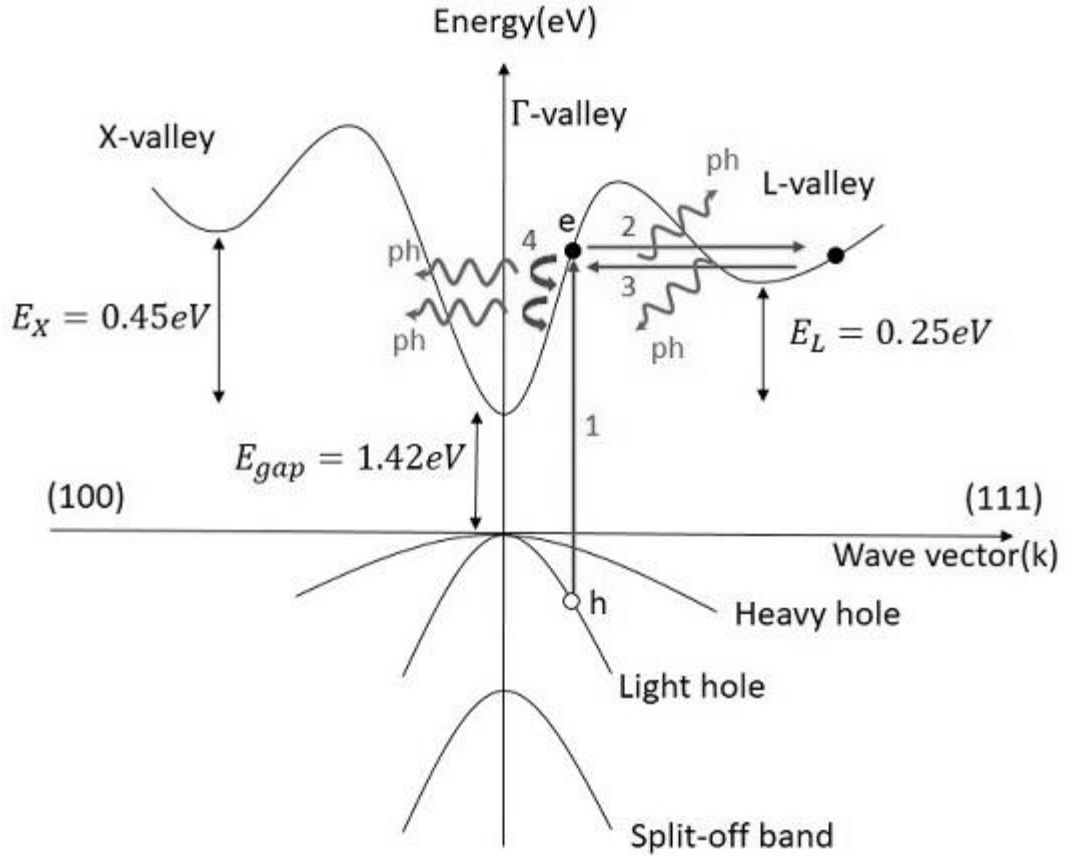
Figure 3.6: Intervalley mechanisms: 1- Excitation of electrons into CB. 2, 3: electron scattering to L valley and back scattering again to initial valley. 4- Relaxation of electron by losing its energy and phonon emission.

Redistribution of the excited electrons to the satellite valleys occurs less than tens of femtosecond after excitation while the backscattering to the principal valley happens until around 10 ps [135]. Intervalley scattering needs phonons with high momentum, technically zone-edge phonons, for electron transferring. A schematic of intervalley scattering and energy relaxation of excited electrons is depicted in Figure 3.6.

The zone-edge phonons have pivotal role in intervalley scattering due to the high momentum. On the other hand, since the difference energy between optical and acoustic phonon is quite small in the zone-edge region, the all possible phonons can participate in this scattering provided by the selection rule based on symmetry of the initial and final state are satisfied.
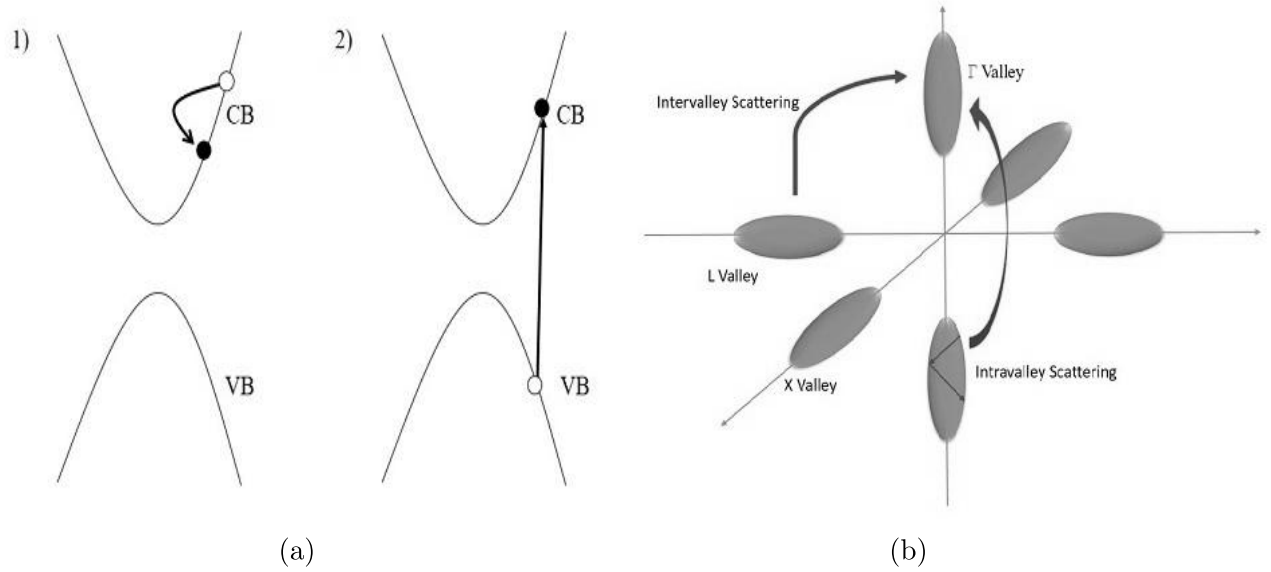
Figure 3.7: a) (1) an intravalley and (2) an intervalley transition in band diagram. CB and VB are conduction band and valence band, respectively. b) Illustration of intervalley and intravalley in an orbital space [134].

3.3 Many-body effects

This phenomena is attributed to the collective behavior of elementary particles, changing the optical or electronic properties of materials. The dynamics of these changes can be observed in a form of nonlinear behavior in optical coefficients like the refractive index or absorption coefficient [136]. These changes are observable through a time-resolved differential photoreflectivity measurement using a pump-probe setup [103]. Mathematically, these interactions change the complex number of refractive index and consequently the imaginary part related to the absorption coefficient. The induced changes can be detected by measuring the reflectivity changes and its dynamics by a time-resolved method. Intensity of the effects depends on the electronic structure of a sample, electron concentration and the energy of the states being studied. Also, it should be noted that the many-body interaction can occur under a quasi steady-state or excited states. We briefly introduce some of the most important many-body effects on direct band gap semiconductors considering a detailed mathematical description need a sophisticated formalism which is not the subject of this work.

The band filling that is a many-body effect which in turn, has the most effective role in the dynamics of the excited electrons and can be barely seen in a degenerate pump-probe setup, if the excitation energy and intensity are greater than the band gap

and a threshold intensity, respectively. This effect is the dominant mechanism in the optical nonlinearity of semiconductor particularly in room temperature [137]. Indeed, the band filling that makes a nonlinear absorption is due to the excited states becoming over-populated, yielding a saturation in absorption at the excitation energy. The absorption coefficient change due to the band filling can be expressed as the following

$$\alpha = \alpha_0(1 - f_e - f_h), \tag{3.4}$$

where α_0 is the linear absorption coefficient and $f_{e,h}$ are the distribution function of electrons and holes [21]. It is obvious from $R + T = 1$, where R and T are reflection and transmission coefficients in an interface of two compounds, that the saturation in absorption lead to an increase in the reflection of the sample. The time in which the states still are overpopulated is called band filling time and highly dependent on the energy and concentration of the excited electrons. In fact, the energy relaxation of the electron determines the band filling time and then after relaxation the induced change in the absorption diminish to the initial value.

The other important many-body interaction is the Coulomb enhancement, in which the coulomb potential between the carriers is enhanced by a factor and changes the absorption coefficient as the following [138]:

$$\alpha(\hbar\omega) = \alpha_0(\hbar\omega, \rho)F_C(\hbar\omega), \tag{3.5}$$

where $F_C(\hbar\omega)$ is the coulomb enhancement and $\alpha_0(\hbar\omega)$ the linear absorption coefficient. The coulomb enhancement factor is a result of the screening of coulomb interaction of the electrons and holes [139]. The enhancement values depend on the energy and concentration of the electrons changing the screening length.

Band gap renormalization or band gap shrinkage is the other effective many-body effect. This effect is a direct result of the electron screening in the conduction band, particularly in the bottom of it, due to the low density of state, decreasing the band gap. The same mechanism occurs for the holes except that it increases the energy of the valence band. These shifts in the bands causes shrinkage of the band gap. Wolf gave an

expression to calculate the band gap renormalization value such that [22]

$$\Delta E_g = -(\frac{e}{2\pi\epsilon_0\epsilon_\infty})(\frac{3}{\pi})^{\frac{1}{3}} N^{\frac{1}{3}}, \tag{3.6}$$

where N is the carrier concentration, ϵ_0 and ϵ_∞ dielectric constants in the low and high applied electric field. Of course, there are some modifications to improve the accuracy of relation (3.6), based on the actual situations such as the effective distance between electrons and holes and the correlation between them [140]. For example, the band gap renormalization is more weaker for 2D electron-hole plasma compared to the 3D one, due to the efficient screening in 3D systems [141].

All these effects change together the optical properties of a sample and the mentioned interactions between the carriers and lattice determine the strength, effective time and, in a general word, the dynamics of them. A comprehensive and detailed study of an interacting electron system can be found in [142], introducing an approach of the semiconductor Bloch equations to extract all the mentioned effects.

4 Pump-Probe differential reflectivity

In this chapter, we will explain the details of the samples and *in situ* analysis in sample growth and preparation. A detailed description of the setup including the introduction of the laser, data acquisition system will be given. Also, the calibration method and technical considerations will be discussed.

The samples are used in our work are a GaAs layer with different Si-doping levels. The samples are grown by molecular beam epitaxy (MBE). One of them is a 1 μm GaAs with 8×10^{18} cm^{-3} Si concentration is deposited on a GaAs substrate. Two 500 nm GaAs samples with two different doping concentrations, one 1×10^{18} cm^{-3} and the other 5×10^{17} cm^{-3}, are grown on two GaAs substrates, as well. These samples were made in Brazilian Nanotechnology National Laboratory (LNNano) in Campinas, Brazil. The samples details are listed in table 4.1 and thereafter we called the samples as they are named in the table. GaAs is chosen as the substrate to decrease the probability of the defects made by the lattice mismatch, and the strains on the interface [143]. For example, the considerable thermal expansion coefficient difference between GaAs and Si increase the probability of defects in the crystalline structure. As mentioned already, pump-probe setup is a contactless method to measure the dynamics of carriers. For example attaching a metal contact on GaAs surface to measure electronics properties generates a strong Schottky barrier while pump-probe does not need sample preparation [144].

Table 4.1: Sample specifications

Sample	Si-concentration(cm^{-3})	Thickness
A	8×10^{18}	1000 nm
B	1×10^{18}	500 nm
C	5×10^{17}	500 nm

In our setup, we use Mai Tai laser producing 100 fs pulses. The Mai Tai laser includes a mode-locked Ti:sapphire pulsed laser which is pumped by a Nd:YVO4 laser in CW mode. The CW laser, emitting 1064 nm beam, is pumped with a diode laser. Then a nonlinear crystal, lithium triborate (LBO) is used to convert 1064 nm to 532

nm with intensity greater than 10 W. After that, the 532 nm output pumps a mode-locked Ti: sapphire laser. The output wavelength is tunable from 690 nm to 1060 nm with a repetition rate of 80 MHz which in turn increases the signal to noise ration in our measurements. The broad range of the laser emission is due to the large absorption band(400 nm-600 nm) and the emission band(600 nm-1050 nm) of Ti:sapphire crystal which is illustrated in Figure 4.1. The sequence of producing the pulsed laser in Mai
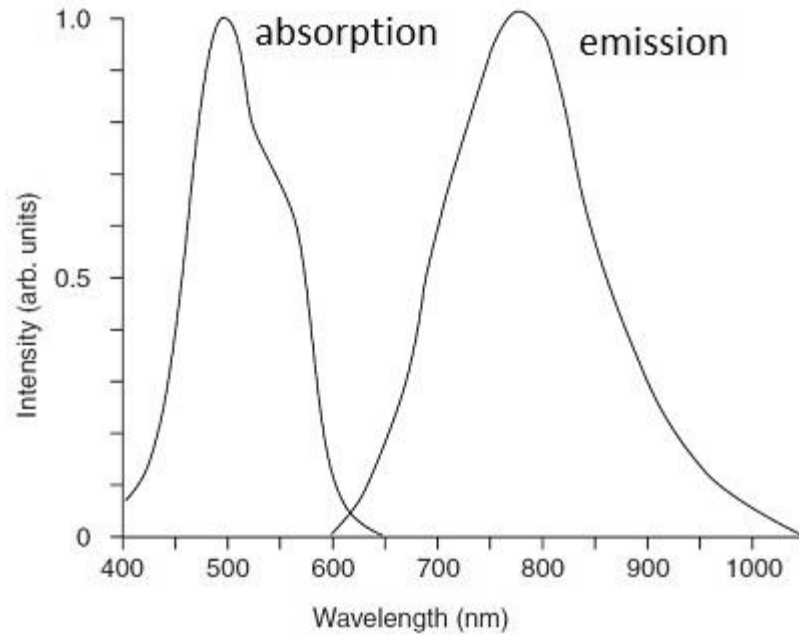
Figure 4.1: Energy level structure of Ti:sapphire crystal [145].

Tai is illustrated in figure 4.2a. The Mai Tai utilizes a combination of an acousto-optic modulator and Kerr lens effect to ensure reliable mode-locking operation even after the laser is off for a long time. Then the beam after escaping from the head case of the laser is divided by a beam splitter into two beams called pump and probe such that the intensity of pump is greater than probe. Before the beam splitter, a polarizer is placed to control the intensity of the laser. A translation stage is used for probe arm to change the optical path between the pump and probe. Movement of the stage is controlled by a stepper motor connected to a computer. Also to avoid detrimental coherent effect between the two beams at the sample, a $\frac{\lambda}{2}$ waveplate is used to set the polarization of the two beams perpendicular [146]. A schematic and a real picture from the setup are represented in Figure 4.3 and 4.4 respectively. The pump and probe beams are focalized to the sample

such that beam spots are 30 μm^2 and $15 \mu m^2$ respectively.

<div align="center">(a)   (b)</div>
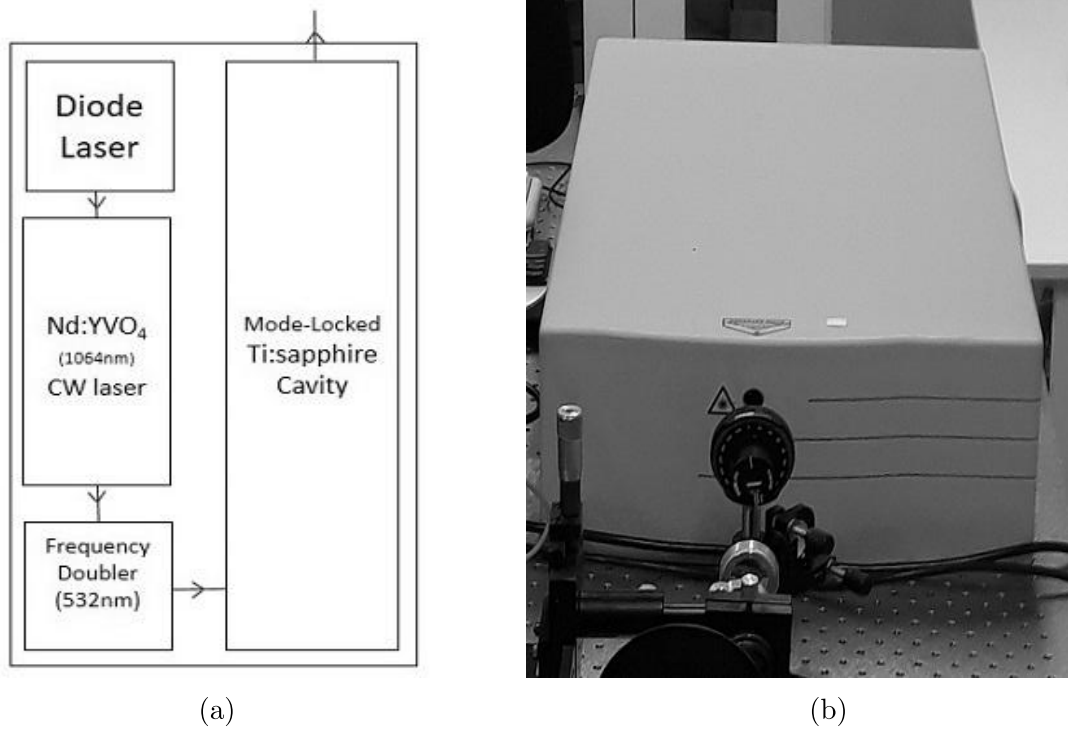
Figure 4.2: (a) Scheme of Mai Tai Laser. Diode laser pumps $Nd : YVO_4$. Then output frequency (1064 nm) is doubled and finally 532 nm CW laser enters into the cavity of Ti:Sapphire laser to produce 100 fs mode-locked pulses [147]. (b) A phot from the laser head and the polarizer in front of it to control the intensity.

It should be mentioned that spot size of the probe must be smaller than the pump in order to see a homogeneous distribution of variation made by the pump. Both beams have a small angle between them and then the reflected probe beam from the sample is fed to the detector. A mechanical chopper and a lock in amplifier are utilized to amplify the signal. In this setup, we modulate both beams with different frequencies and the detector is locked to the Lock-in system with the sum of frequencies of the pump and probe [148]. This technique called double modulating is performed by a mechanical chopper but a blade with two different aperture ratios as shown in figure 4.5a. The pump and probe frequencies and the frequency of the reference for the Lock-in is controlled by the controller shown in Figure 4.5b. Besides, since the angle between the two beams is so tight, thus reflection of the pump and probe can overlap. Even by placing an aperture, the dual modulation is necessary to ensure that the pump reflection does not any interference with the signal in the detector.

Frequencies 1200 Hz and 1500 Hz are chosen for the pump and probe respectively.
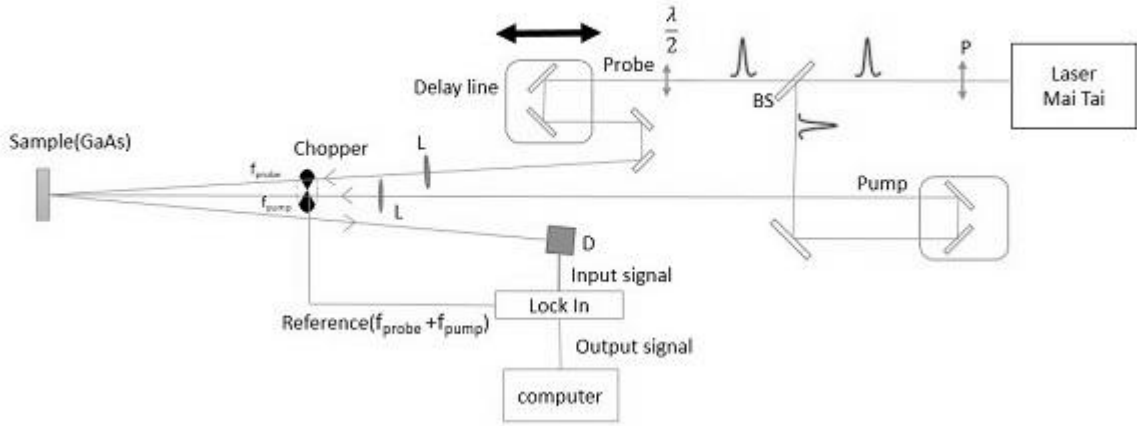
Figure 4.3: Scheme of time-resolved differential reflectivity in where P: polarizer, BS: beam splitter, L: lens, D: detector, $\frac{\lambda}{2}$: half-wave plate, f_{pump} and f_{probe} are modulation frequency of pump and probe, respectively.
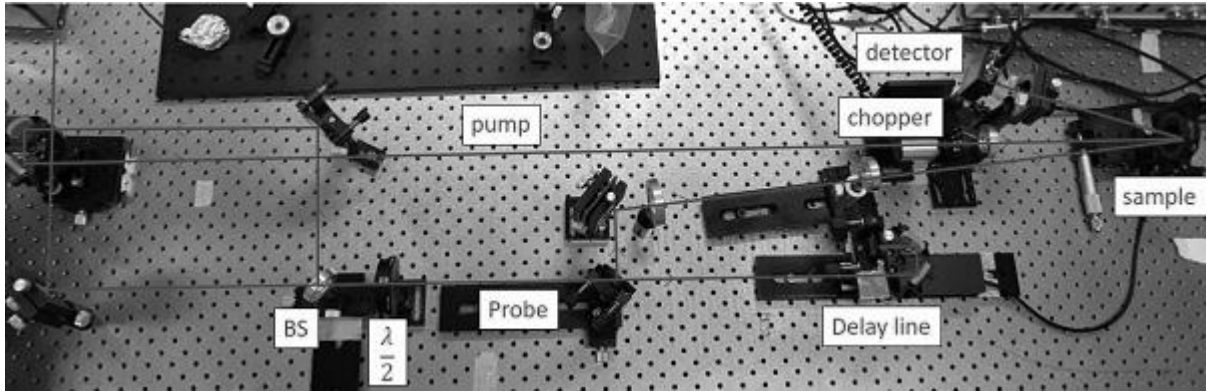
Figure 4.4: A photo from the setup. The laser path is highlighted by red lines. $\frac{\lambda}{2}$: half-wave plate and BS: beam splitter.

The measurements are carried out in the room temperature. The output signal of the Lock-in amplifier, called $DeltaV$, is relevant to the induced change of optical reflectivity of the sample. We will explain the relation between this quantity and optical reflectivity in section 4.2.

The delay stage is a MTS50-Z8 Thorlabs translation stage, shown in Figure 4.6a, which is controlled by a stepped motor, brushed motor controller- Thorlabs KDC 101 which is presented in Figure 4.6b. The minimum achievable movement for the stage is 0.05 μm, associated with 0.32 fs. Also, the maximum distance can be covered is 5 cm which means the maximum temporal window is 0.3 ns. It should be noted that the temporal window after excitation (the zero delay time) will practically be shorter, because
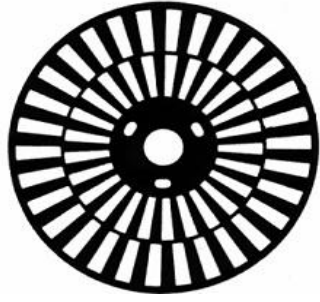
(a)   (b)

Figure 4.5: (a) The chopper blade used in the setup with two different apertures and modulated frequencies. The pump is modulated with the inner part of the blade and the probe by the outer part. (b) The modulator controller and the f_{sum} status that is chosen as the reference frequency. The frequency is driven by selecting a proper socket shown in the red frame [149].
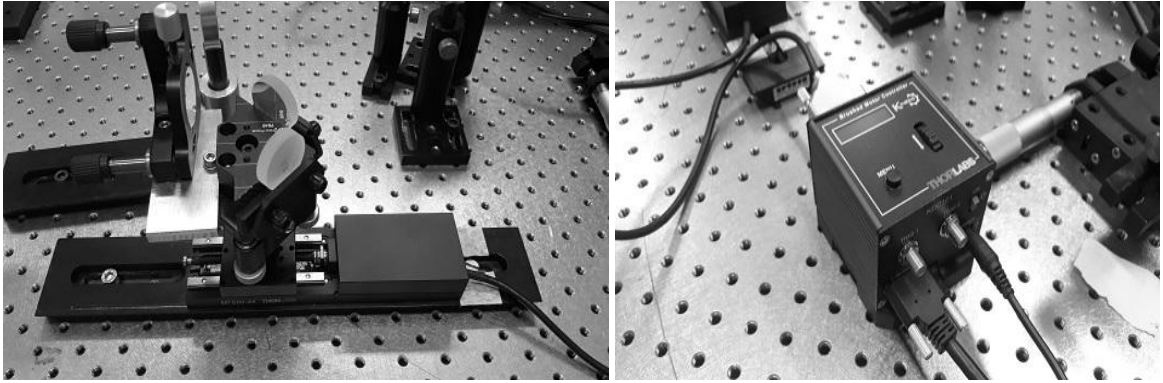
(a)   (b)

Figure 4.6: photos of the components used in this thesis.(a) The mirrors are mounted on the translation stage to make a delayed probe. (b) The motor controller that is connected to the translation stage.

we need to record the signal before the zero delay time. However, temporal resolution in this setup is determined by the temporal pulse width and the minimum step movement of the translation stage.

The minimum movement of the stage could be less than 100 fs. However, we choose a movement making 140 fs to avoid temporal overlap of the pump and probe pulses.

4.1 Calibration Process - Finding Zero Point

This is the most important step for calibrating the system to find where the two pulses (the pump and probe) reach at the sample surface in the same time. Two consecutive

pulses in the laser with 80 MHz repetition rate have 12.5 ns time difference as shown in Figure 4.7. The probe pulses have the same temporal distance between them but different delay time respect to the pump pulses. In calibration method, one needs to find the pump and probe pulses in the overlapped condition in temporal domain.

The Second harmonic generation (SHG) in a nonlinear crystal occurs when the phase-matching conditions meet in the sample [33]. The phase-matching conditions are the temporal and spatial circumstances that should be satisfied for both beams in the crystal. The phase-matching conditions are the straightforward results of the energy and momentum conservation. The amplitude of the second harmonic generated beam is given by

$$E_{SHG}(t) \propto E_{pump}(t) \times E_{probe}(t - \tau), \tag{4.1}$$

where $E_{SHG,pump,probe}$ are the electric fields of the SHG, pump and probe beams respectively and τ the temporal delay between the two beams. When the time difference between
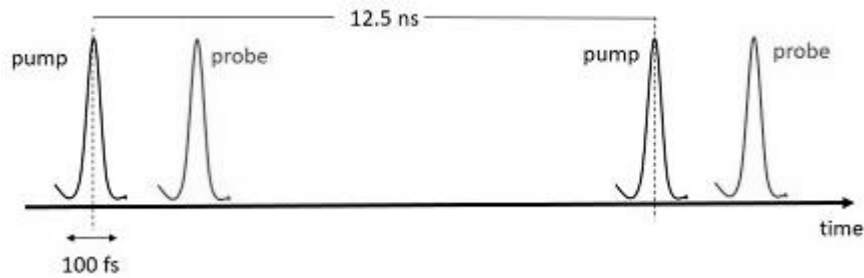
Figure 4.7: Schematic of delayed pulses. Temporal distance between pump pulses is fixed and determined by repetition rate. The relative temporal delay between the pump and probe is induced by a translation stage.

two pulses is zero, $\tau = 0$, the intensity of the doubled frequency $I_{SHG} = |E(t)^2|$ is maximum, meaning that the second harmonic is generated in the sample. Other parameters that should be considered here are the polar and azimuthal angles of the beams with the optical crystal axis. These angles should be set such that the phase matching condition be satisfied. Second harmonic generation with two beams can be implemented in two different geometries called collinear and non-collinear geometry. The former occurs when the incident beams propagate in the same direction and the latter happens when two beams are not parallel and cross each other in the sample. The collinear configuration
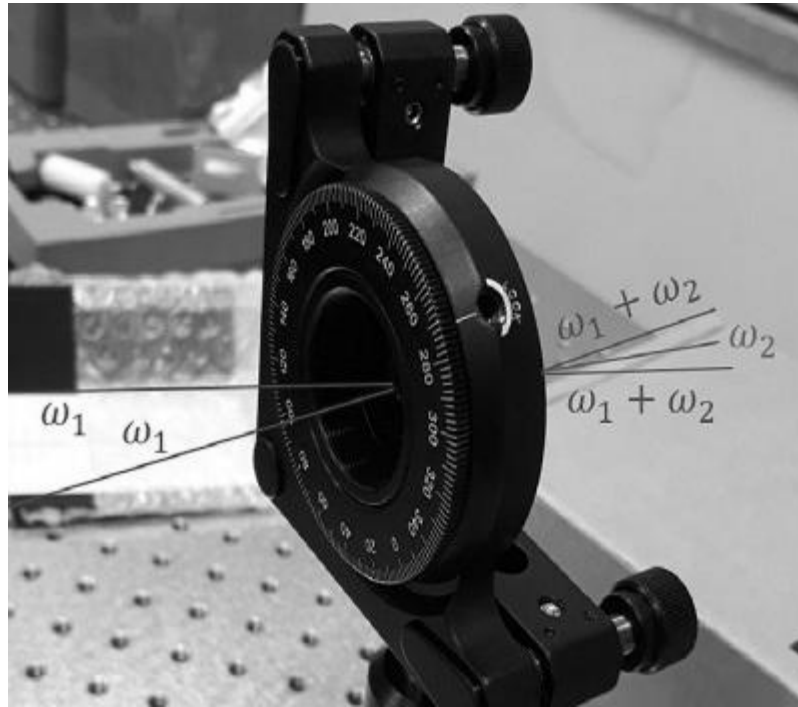
Figure 4.8: The incident beams with wavelength $\omega_1 = 800$ nm are overlaped at the BIBO crystal in a non-collinear configuration. The third beam with $\omega_2 = 400$ nm wavelength will appear when two input beams have no delay time between them. The lines are exaggeratedly drawn to clear the relative position of the beams. The holder have different freedom degrees to control the optical axis of the crystal. Those input beams after passing the crystal have principal and doubled frequencies, showed by $\omega_1 + \omega_2$ in this figure.

is more efficient in the second harmonic generation, however, the non-collinear has the advantage that it is more sensitive to the τ value [150].

For calibrating our setup, a BIBO crystal, which is a nonlinear crystal, is placed in a holder in which the polar and azimuth rotation is available in order to set the crystal in the proper angle respect to the input beams [151]. The pump and probe with 800 nm wavelength recombine at the BIBO surface. When the output beams colour being changing to purple it means that the angles are almost in the right positions. The purple color is due to the mix of the principal beams(red) and the doubled frequency beam(blue). Then we have to find the zero delay time between the beams by changing optical path of one the beams via the translation stage. Once the optical paths beams are equal then the third beam, doubled frequency, will appear between two input beams as shown in figure 4.8.

4.2   Data acquisition

The signals are recorded by a Thorlabs- PDA 100A-EC Si with switchable gain detector, showed in Figure 4.9a. The operational wavelength range is between 340 nm-1100 nm. In order to reduce the noise, we selected the zero gain for the detector to avoid the

<div align="center">(a)   (b)</div>

Figure 4.9: Photos of (a) photodetector, and (b) A/D converter. Model: National Instrument USB 6008

noise appearance due to the amplification. The final results are averaged over 10 times measurements for each point of the samples. To avoid any local effects of the sample on our results, we have measured three different points at the samples. As shown in figure 4.10 the probe intensity without the pump is V_0, which is measured directly by the detector, whereas the induced probe intensity variation made by the pump, called ΔV, is the output signal of Lock-in amplifier. The ratio of the probe variation on the probe intensity without pump is given by

$$\frac{\Delta V}{V_0} = \frac{\Delta R}{R}, \tag{4.2}$$

where R is reflectivity of the sample without the pump and ΔR is the reflection change due to the pump. On the other hand, the ratio is proportion to the refractive index modification and can be written as the following [18]

$$\frac{\Delta R}{R} = \frac{4\Delta n_2(\hbar\omega_{probe}, t)}{n_2^2(\hbar\omega_{probe}, t) - 1}, \tag{4.3}$$
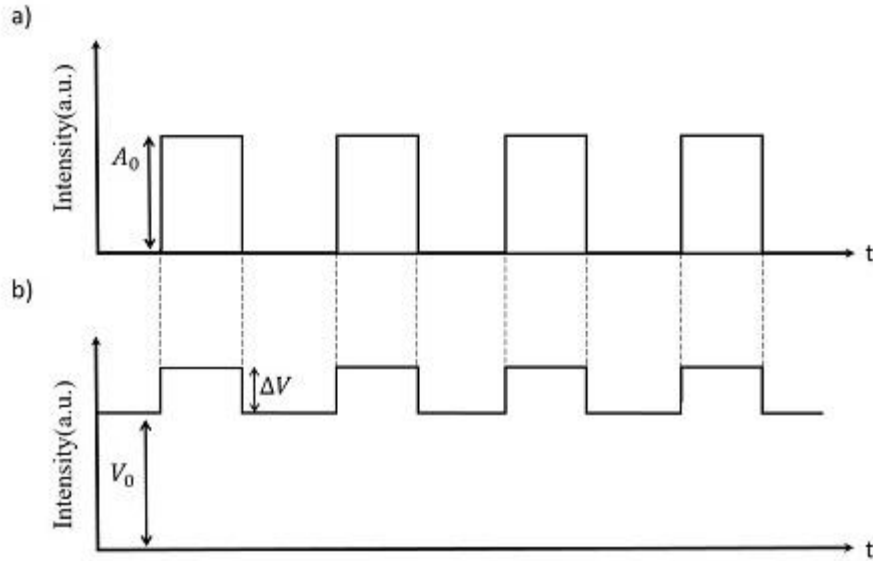
Figure 4.10: Temporal profile of a) pump and b) probe intensity in an amplification system by a Lock-In. The induced variation (ΔV) of the probe caused by the pump beam [18].

where n_2 and Δn are sample refractive index and its variation. The measurement procedure and data recording is controlled by a Labview program. As it is mentioned in description of mechanical part, the translation stage is controlled by the Labview as well. The minimum displacement for the delay line stage is $21 \mu m$ making a 140 fs delay time between the pump and probe. For each step, the stage remains in the fixed position for one second to capture the data. The one second data can be monitored in the signal scope in the control panel. Then the signal will be averaged in each step and stored versus time. This result can be seen in the real time signal in the control panel. The stop time for each position is chosen based on the time constant of the Lock-in amplifier.

Due to stabilizing of the Lock-in output signal we choose normally an acquisition time, two or three times greater than the constant time of the Lock-in to make sure that the signal is stable. The Lock-in output signal is captured by a computer through an analogue to digital (A/D) converter shown in 4.9b. The sampling number and rate of the A/D converter are 1000 and 1000 Hz, respectively. The multiplication of the sampling number and sampling rate gives the time acquisition of the A/D converter where can be modified by the DAQ assistance of the Labview as shown in Figure 4.11. Indeed, this value determines how much time the translation stage stays in a fixed position to take data.
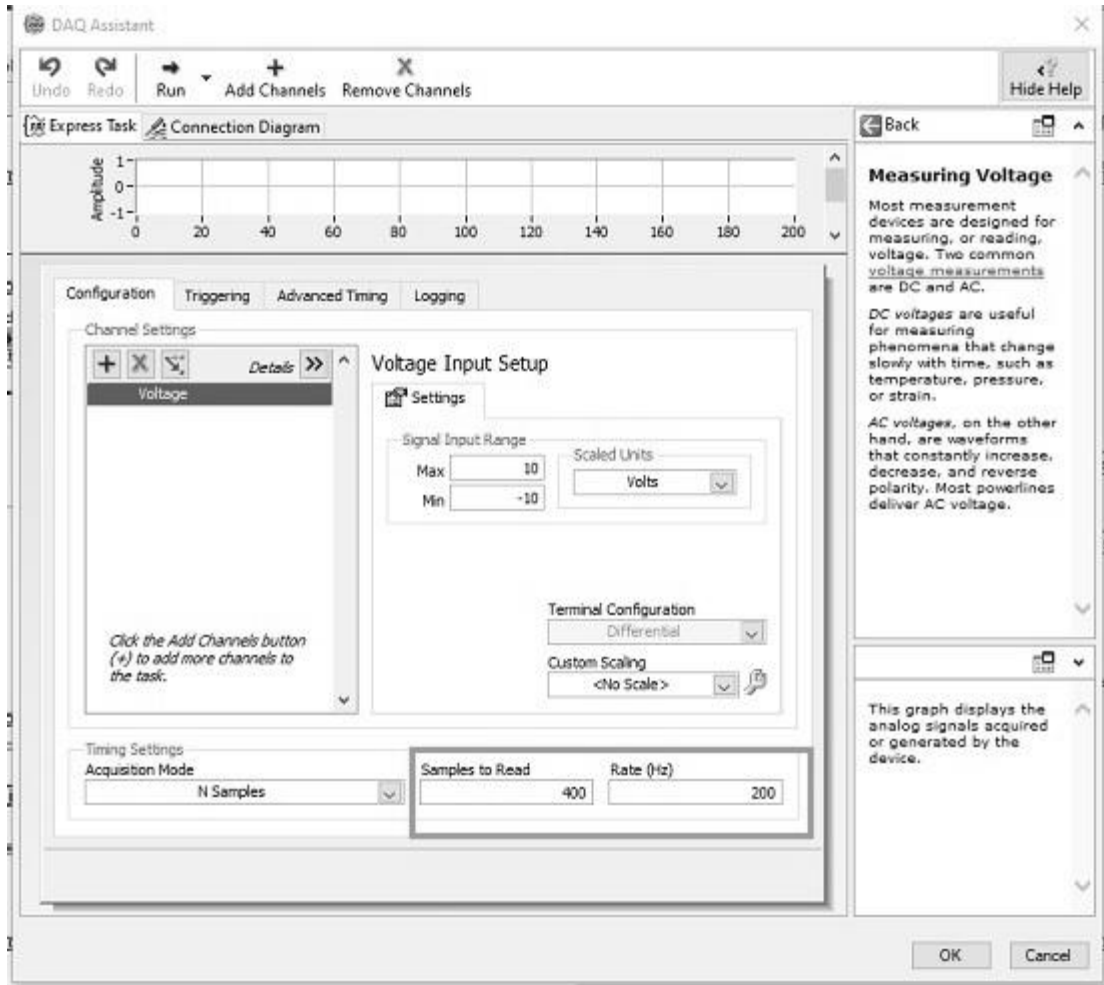
Figure 4.11: A screenshot from the DAQ setting of the control panel of the setup. The "sample to read" and "rate (Hz)" of the DAQ can be selected via the DAQ assistance.

4.3 Measurement Procedure

In this section, we will consider the measurement process like the wavelength selection and delay time control. For wavelength selection, we have to take care about the absorption coefficient of the sample, such that the beams should not penetrate inside the substrate. This consideration guarantees that the samples are supposed to be bulk system without presence of any interface. Regarding to the movement of the translation stage, the care should be taken that the initial point must be before the zero point which we have already found through the calibration process to ensure not lose the zero delay point between the pump and probe. The control panel of the setup is shown in Figure 4.12. The total delay time, the temporal resolution and the initial point can be selected by filling the point number, step size and initial position filed in the control panel respectively as presented
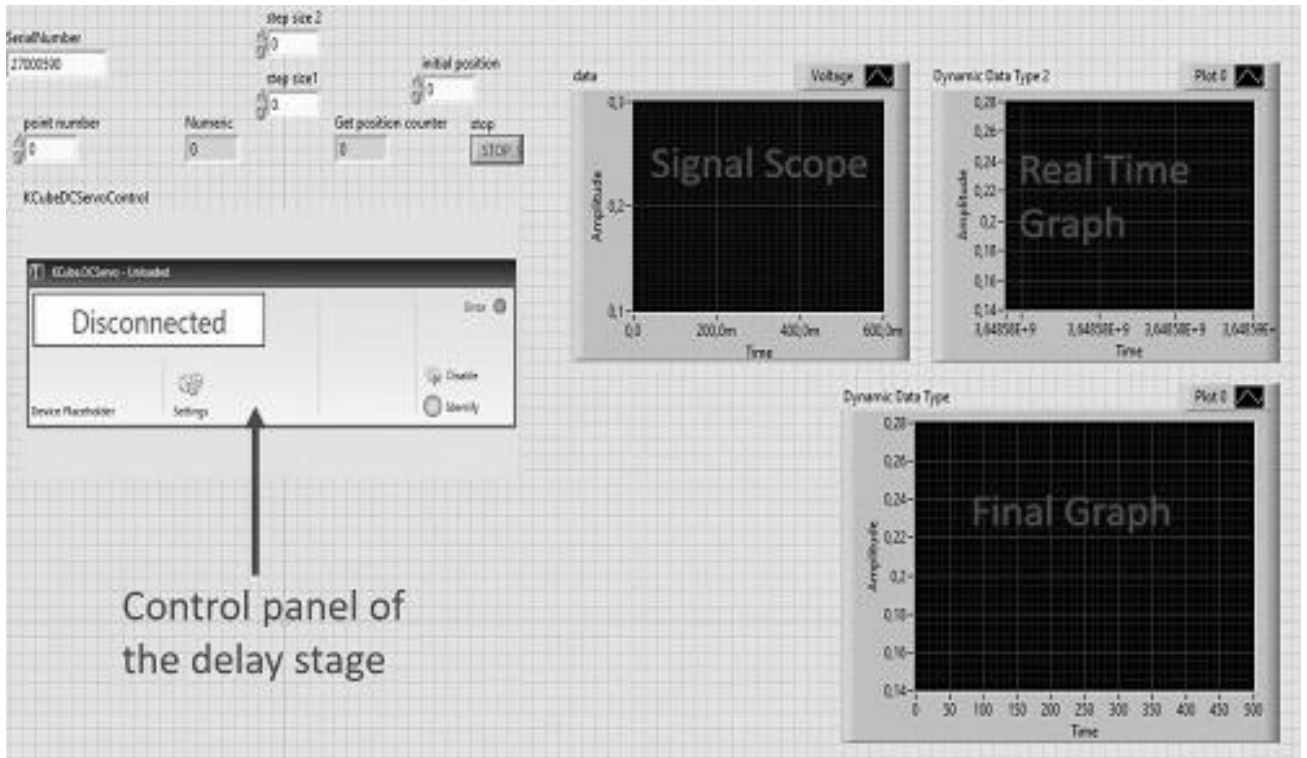
Figure 4.12: A screenshot from the control panel of the setup. Three scopes show signal in each delay versus time, real time signal and final signal. The blank fields are controllers in order to determine a time step and maximum delay time for a measurement.

in Figure 4.12.

Another technical consideration is the polarization of the pump and probe. The growth direction of the samples is (001) meaning that the growth direction is perpendicular to the sample surface. This geometry has planes including the same of atoms as shown in fig.4.13. The signal intensity is independent of the pump polarization because the GaAs bulk is nearly optically isotropic. However, an anisotropy could be arisen due to the surface effects. There is a method to check the macroscopic isotropy of the surface called Reflection high-energy electron diffraction (RHEED) [152]. Moreover, the capturing mode of the probe is independent of the probe polarization. In some experiments like the EO sampling which is based on the polarization of the probe, the probe polarization is important. The pump-probe techniques were used to study the dynamics of photo-carriers in GaAs with different preparation like ion-irradiated and low-temperature grown crystal [153, 154].
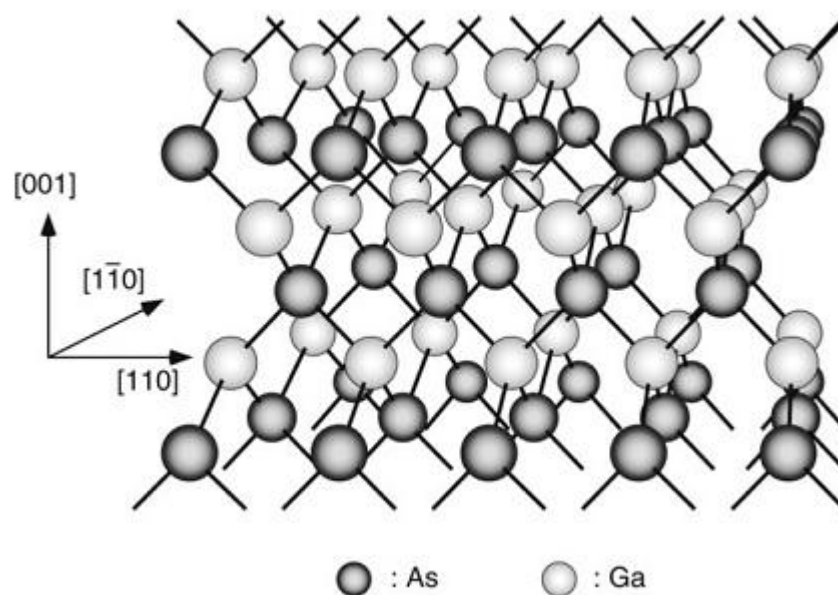
Figure 4.13: Atomic structure of GaAs. (001) GaAs have planes with the same atoms [152].

5 Results and discussions

This chapter is divided into two parts. First part shows the results of simulations that are carried out to study diffusion of carriers in GaAs. In this section after presenting the result, we focus more on the idea that how diffusion effects can be observed in a degenerate pump-probe setup. Second part demonstrates the experimental results obtained by the time-resolved differential reflectivity setup at different situations to investigate the roles of different parameters on the dynamics of the optical and electronic properties of GaAs.

5.1 Diffusion

Diffusion is a key factor in the dynamics of photo-excited carriers in semiconductors. The main reason that diffusion is taken into account is that the samples are bulk of GaAs and the absence of any interface with quantum wells or barriers eliminate the possibility of charge trapping, allowing the diffusion occurs without any perturbation until the carriers reach a uniform distribution. The presence of the barriers and interfaces capture the charged particles and reduce the life time of the electrons and holes [155]. Since the effective mass of electrons and holes are different in semiconductors, we need to utilize an approach that takes into account these features and describes the diffusion behavior of the electrons and holes. A well-known model called the ambipolar diffusion model is considered that includes the mentioned points [156]. An exact solution of the diffusion equation can be written as the follows [157]

$$N(z,t) = \frac{N_0}{2}e^{\alpha^2 Dt}[e^{-\alpha z}erfc(\frac{2\alpha Dt + z}{\sqrt{4Dt}}) + e^{\alpha z}erfc(\frac{2\alpha Dt - z}{\sqrt{4Dt}})], \qquad (5.1)$$

where *erfc* is the complementary error function, N the carrier concentration, N_0 initial carrier concentration, α absorption coefficient, D the diffusion coefficient, t and z time and position in the sample along the growth direction, respectively. Since the mobility of the electrons and holes are different, we have to define an alternative value called ambipolar

diffusion constant and given by

$$D_{am} = (D_e \mu_h + D_h \mu_e)/(\mu_e + \mu_h), \qquad (5.2)$$

where D and μ are diffusivity constant and mobility of electron and hole that are represented by e and h indices, respectively. The carrier concentrations based on Equation
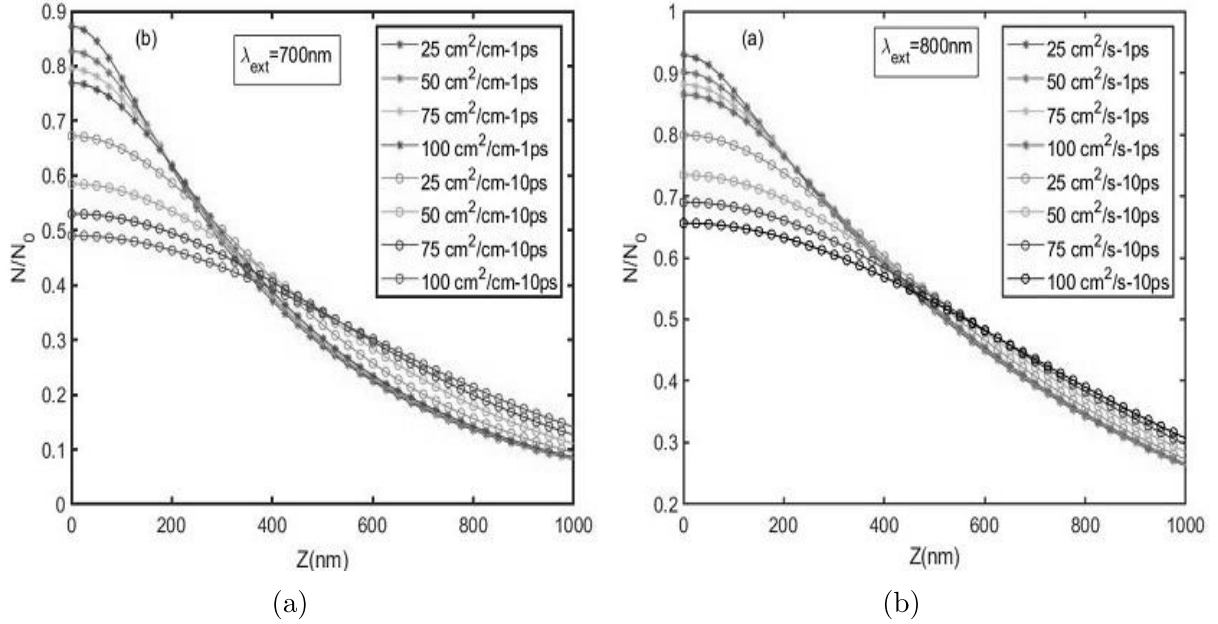
Figure 5.1: Profile of carrier concentration inside the sample and along the sample growth direction for 1 ps and 10 ps after excitation. a) Excited by 700 nm and b) excited by 800 nm at four different values of diffusivity.

5.1 versus penetration depth of the GaAs for 1 ps and 10 ps after excitation are shown in Figure 5.1. Also, the temporal evolution of carrier concentrations for two different excitation energies are depicted in Figure 5.2 and 5.3. Four ambipolar diffusion constants are taken from 25 cm^2/s to 100 cm^2/s for the simulations [32, 158]. Two kind of plots are represented in this work such that each shows the variation of carrier concentration, one versus the depth of the sample in two different times after excitation (1 ps and 10 ps), Figure 5.1, and the other is versus the time after excitation at two fixed position inside it (Figures 5.2 and 5.3). According to equation 5.1, one expects that carrier concentration reduces with time as seen in Figures 5.1, 5.2a and 5.3a. Temporal evolution of carrier concentrations are shown in Figure 5.2 and 5.3 for different depths of GaAs along the growth direction. As mentioned in this chapter introduction, our focus is on observable

parameters which may change in a degenerate pump-probe setup, particularly with our setup configurations. The Figure 5.1 shows the carriers are more localized when they are excited by shorter wavelengths. Moreover, the decrease of carrier concentration at the surface is more evident in 700 nm compared to 800 nm. The diffusion effects are more
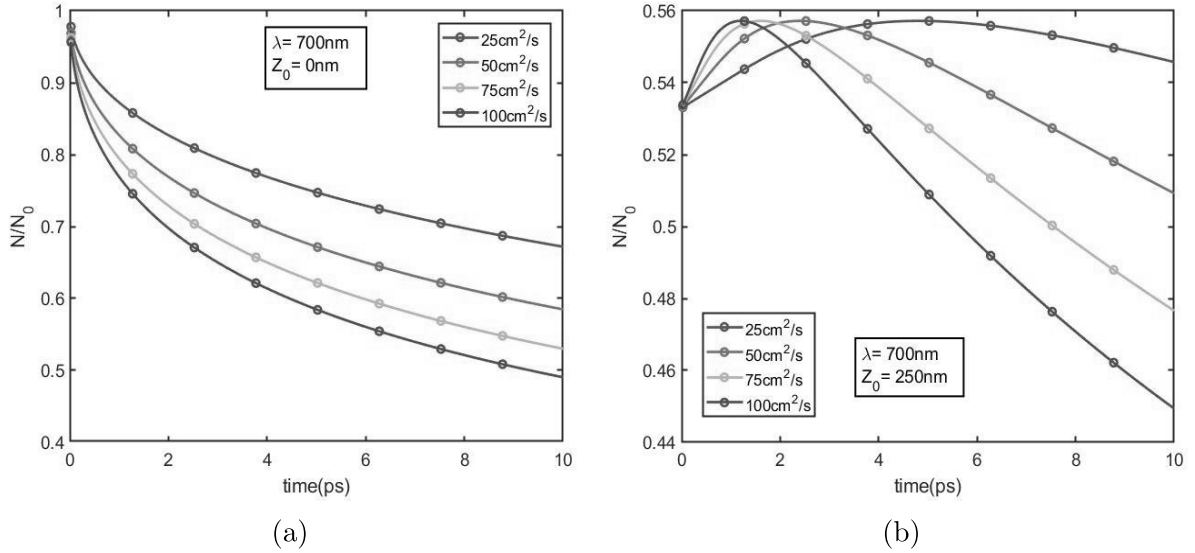
Figure 5.2: Temporal evolution of normalized concentration of carriers excited by 700 nm at a) the surface of sample and b) 250 nm inside the sample with four values of diffusivity.

evident when we use a degenerate pump-probe setup. On one hand, the spatial carrier concentrations are highly dependent on the pump wavelength. On the other hand, the maximum thickness that the probe beam could be covered is wavelength dependent due to the dependence of the absorption coefficient of GaAs on wavelength. Furthermore, it should be noted that in reflection mode of pump-probe setup the penetration depth of the probe becomes half of the pump. For instance, the pump penetration depths for wavelengths 700 nm and 800 nm are around 500 nm and 800 nm, respectively. Thus, for a similar initial carrier concentration for both wavelengths, the generated carriers made by 700 nm are more localized near the surface in the GaAs. The carrier distribution with higher Diffusion constant and long times after excitation have slower slopes and consequently are more stable. Also, as shown in Figure 5.1, the carrier distribution with higher diffusion constant and long times after excitation have slower slopes and consequently are more uniform. It implies that the diffusion effects are less considerable after 10 ps in the ultrafast dynamics of the carriers, at least in the mentioned wavelengths. Moreover, 700 nm probe can just detect $\frac{500nm}{2} = 250nm$ beneath the surface where the concen-
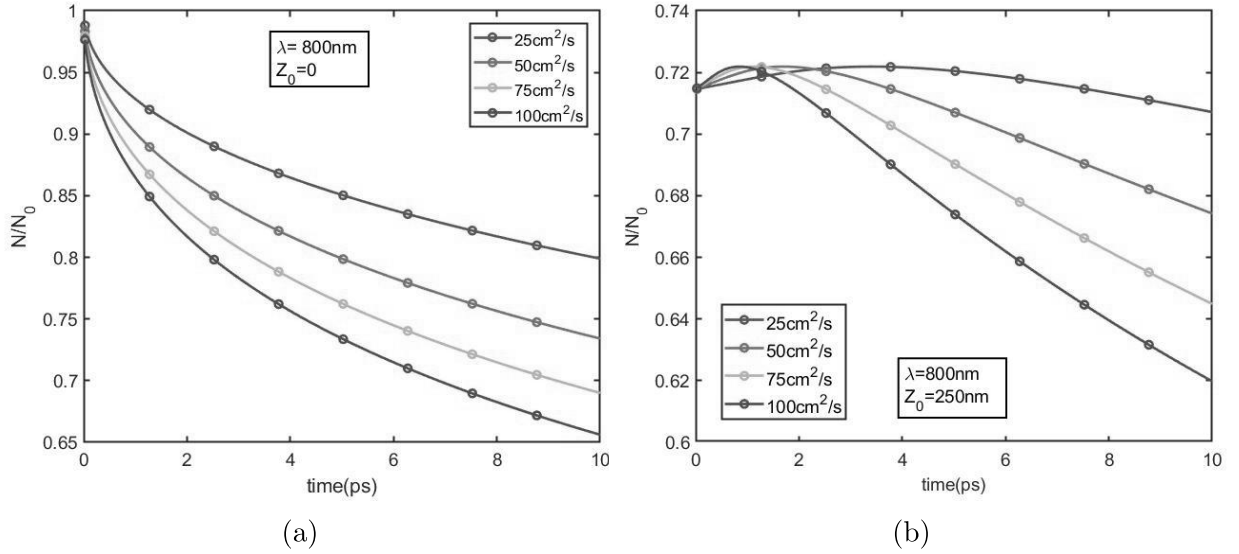
Figure 5.3: Temporal evolution of normalized concentration of carriers excited by 800 nm at a) the surface of sample and b) 250 nm inside the sample with four values of diffusivity.

tration variations are more intense as can be seen in Figures 5.2b and 5.3b. Whereas the maximum penetration for 800 nm probe is around 400 nm, where the changes are smooth. Therefore, in a pump-probe setup, changes in a probe intensity should be more pronounced in shorter wavelengths due to dynamics that is induced by the diffusion.

5.2 Experimental Results

In this section, we present the experimental results and discuss all details of data and show that our results have good agreements with theoretical calculations reported elsewhere and other experimental results that have been obtained with other setups [8, 9, 93, 132, 153, 154]. We divide the results of time-resolved differential reflectivity into three subsections in which different situations are investigated for the samples. Firstly, we will show the effects of the excitation wavelength on the differential reflectivity of the samples related to the dynamics of excited carriers. Indeed, change of the excitation wavelength varies the residual energy of excited electrons in the conduction band and we want to understand the relation of the dynamics of the carriers with their energy. Then we will show the investigation results of the effects of the doping levels on the dynamics and optical properties by performing the same measurement procedure for three different doped GaAs samples. Finally, the results that are obtained at different pump intensities will be

presented for one sample to determine the effects of the excited carrier concentration on their dynamics.

5.2.1   Effects of the Pump Energy

Sample A is excited by four wavelengths 800, 750, 720 and 700 nm. As explained in Chapter 2, results are presented by $\frac{\Delta R}{R}$ versus time showing the changes of the optical reflectivity induced by the excitation. We will concentrate on two main features of the signals, the time of peaks and the followed decay.

As shown in figure 5.4, the probe intensities, which have the wavelength as same as the pump, begin to rise up at the zero delay time for all excitation wavelengths. It means that even at the non-resonance energy excitations this nonlinear absorption occurs. The main reason of the transient peaks is band filling in the conduction band, giving rise the absorption saturation and as a result of that it increases the reflectivity in the zero time [159]. The plots in figure 5.4 show that the peak times are dependent on the excitation wavelength. For example, in sample A, the peak time is around 3 ps for 800 and 750 nm. Whereas the signals reach their peaks around 10 ps for 720 nm and 5 ps for 700 nm. Surprisingly the peak time after a considerable increase at 720 nm returns back to the lower value for 700 nm.

We attribute the increase of the peak time for 720 nm to the intervalley scattering. Excitation with 720 nm, which is a threshold energy, generates electrons with enough energy to scatter into L valley in GaAs. The electrons remain in L valley for a while, of the order of 10 ps and then they come back to the main valley. Similar values for the intervalley transition from L to Γ valley are reported through FWM spectroscopy and time resolved luminescence which were around 8 and 10 ps [160, 161]. Most of the electrons which are staying in L valley repopulate the initial states in Γ valley and keep the state filled and consequently increases the band filling time. It should be mentioned that the electrons in the satellite valleys have almost no influence on the optical properties due to heavier effective masses. However, in 700 nm where we expected to observe the intervalley scattering effects more effectively, the rise time returns around 5 ps. According to the energy band of GaAs, the 700 nm excitation beam has enough energy to excite the
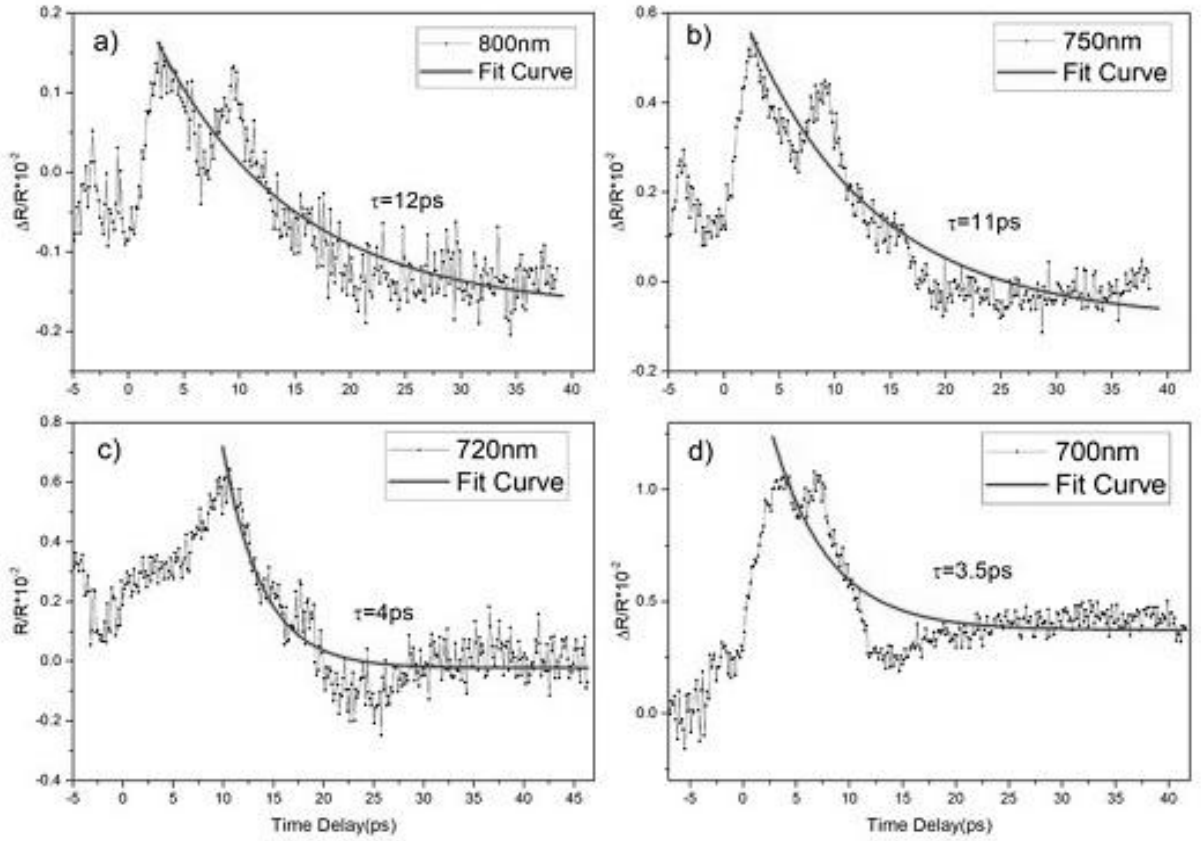
Figure 5.4: Differential reflectivity is obtained for sample A at a) 800 nm, b) 750 nm, c) 720 nm and d) 700 nm. The relaxation times (τ), which re obtained from the fit equation 5.3, are represented in each plot.

electrons from the split-off band to the conduction band. The contributions of excited electrons are almost 40%, 40% and 20% for heavy holes, light holes and split-off bands respectively [9]. In contrast to the electrons in L valley, the excited electrons from the split-off band occupy states in the bottom of Γ valley with effective effects on absorption changes. This redistribution of electrons has yielded to the reduction of transient time due to the introduction of new occupied states in the conduction band which in turn decrease band filling and consequently the peak time. Indeed, the allowed interband transition from the split-off band redistributes the filled states in the conduction band [159]. One more explanation for the reduction of the band filling time can be based on the diffusion effects. As discussed in the section 5.1, the diffusion effects are more obvious for short wavelengths in a degenerate pump-probe setup. As shown in figure 5.2, the carrier density drops considerably where the probe can cover spatially. It means that the diffusion
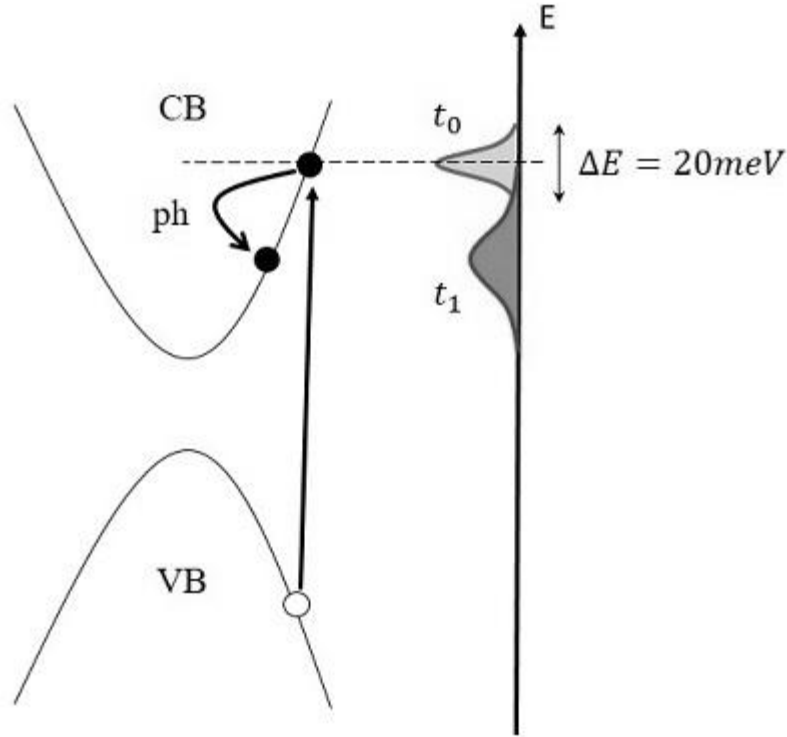
Figure 5.5: Blue shade: the electron distribution at the excitation time t_0; and red shade: the broadened distribution t_1 time after the excitation. $\Delta E = 20 \ meV$ is the energy bandwidth of the pump and probe which is the same as the energy distribution of electron at t_0. If an excited electron lose its energy by emission of one LO phonon, containing energy more than 20 meV, it is removed from the detection of the probe.

suppresses the band filling and localized carrier effects and therefore the transient time returns back around 5 ps.

Now, we analyze the the signal decay followed after the transient peaks. The signal decay is related to the electron relaxation in the conduction band which is expressed based on electron-electron and electron-phonon interactions phenomena which are addressed in chapter 3. The generated electrons have a distribution in the conduction band as a result of the finite bandwidth of the pump beam which is around 20 meV as shown in figure 5.5. Then these distributions are broaden and shifted into lower energy due to the electron-electron and electron-phonon scatterings, respectively. The dynamics of the excited electron distribution can be detected by the probe beam. Therefore, the decay part of signals is fitted by a bi-exponential function which is given by

$$\frac{\Delta R}{R}(t) = Ae^{-t/\tau_1} + Be^{-t/\tau_2}, \tag{5.3}$$
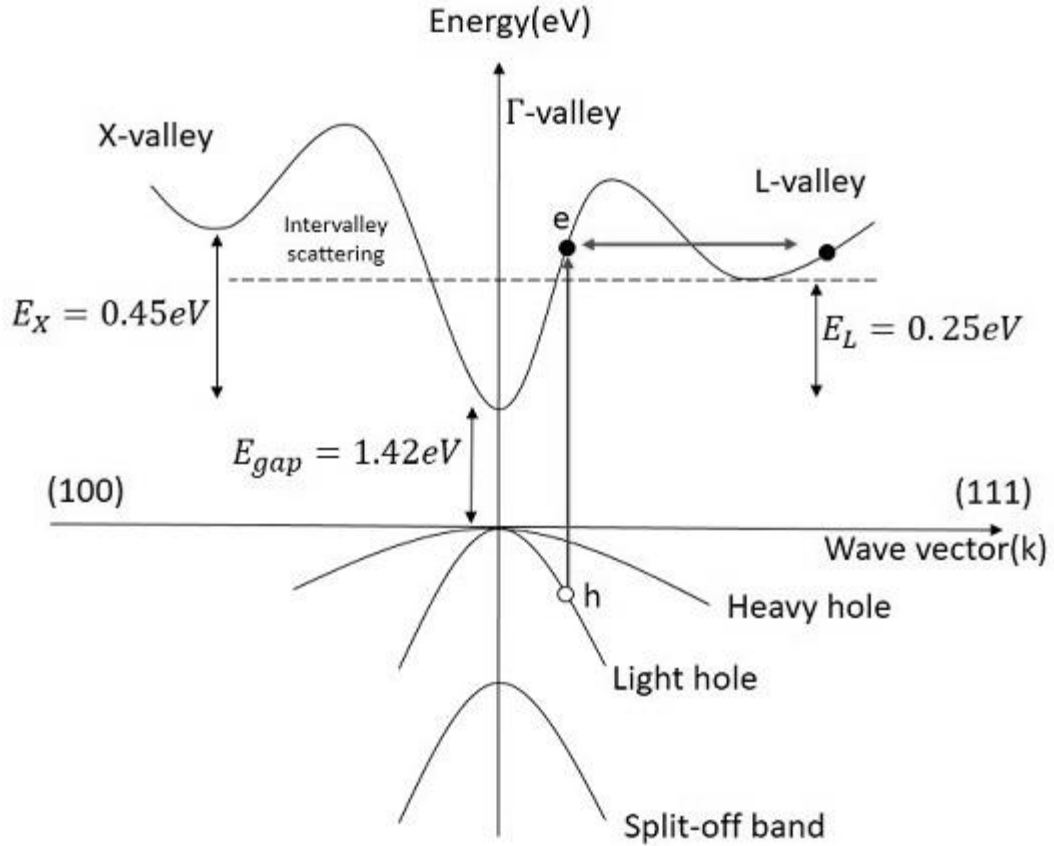
Figure 5.6: Energy diagram of GaAs. The dash line shows the threshold energy indicating that the excited electrons with energy higher than the threshold value are available to scatter into L valley. The details of energy band are given in 3.2.

where A and B are constants and related to intensity of each decay and τ_1 and τ_2 the time parameters related to the main mechanisms of the electron relaxation of electron-electron and electron-phonon scatterings, respectively [162]. In most of our signals, the output fit parameters showed that the two time constants are the same. It is because the limited time resolution of the setup does not permit to observe electron-electron scattering with the time interaction of less than 100 fs. Moreover, increasing the excited electron concentration leads to a faster decay in electron-electron relaxation channel and thus, it makes resolving such a fast event more difficult [163]. Decay with a single exponential is in agreement with recent theoretical work determining thermal relaxation of electrons in semiconductors [91]. Therefore, we are able to find just the time parameter relevant to the electron-phonon interaction.

For sample A, the results show that by increasing the energy of the pump beam, the relaxation times are reduced such that for 800 nm and 750 nm the relaxation times are
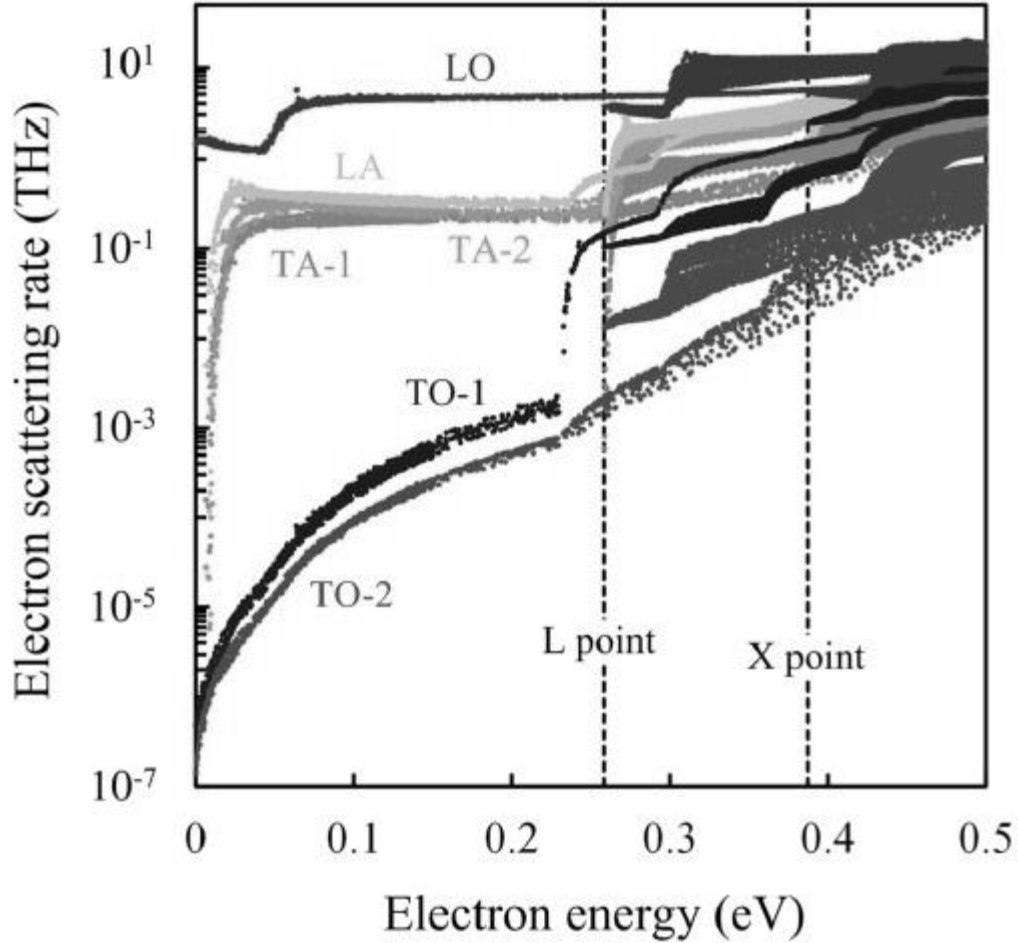
Figure 5.7: The simulated scattering rate of electrons due to each phonon mode versus energy [164]. TA-1 and TA-2 are transverse acoustic phonons with energies 1.8 and 2.4 THz, respectively. Also, TO-1 and TO-2 are transverse optical phonon with energies of 7.84 and 7.56 THz. L point and X point are the necessarily energies for intervalley transition into L and X point.

12 ps and 11 ps, respectively. In this energy range the main process of electron relaxation is electron-phonon interaction such as Frohlich interaction and coupling of optical and acoustic phonons with electrons. As explained in chapter 3, in the Frohlich interaction, as the energy of the excited electrons increases in the conduction band, the probability of scattering between electrons and phonons is reinforced and therefore, the electrons lose their energy more rapidly. However, a relaxation time related to the Frohlich interaction is around 125 fs which is much lower than our calculated values. Because the electrons interact with other branches of phonons instead of only LO phonons and often these interaction are considered underestimated in dynamics of electrons [165]. Recently, more accurate studies have been conducted to investigate effects of TO, LA and TA phonons

on dynamics of electrons through deformation potential formalism [132, 164]. For this aim, the simulations based on Boltzmann transport equation (BTE), a model describing transport of electrons in a lattice [166], are provided to consider all of phonon modes in calculating relaxation time of the electrons. Figure 5.7 presents the simulated scattering rate of electrons in a mode-by-mode phonon demonstration revealing lower electron scattering rates with acoustic phonons compared to LO phonon. Moreover, transverse optical phonons have the lowest scattering rate between phonon modes. Therefore, dynamics of phonons becomes more important because each phonon depending to energy, wavenumber and being acoustic or optical mode has its contribution on dynamics of electrons.

Decay of the zone-center LO phonon to other branches of phonons is one the most common aspect of dynamics of phonons [167]. Different mechanisms are introduced so far to describe dynamics of LO phonons. For example, Klemens and Ridley channels are the most important mechanisms of phonon decay such that the former is referred to decay of a LO phonon into two LA phonons with opposite wavenumber and the latter is attributed decay of a LO phonon into a TO and a LA phonons [168, 169]. Specifically, in GaAs case, another decay channel is introduced by Vallee in which a zone-center LO phonon decays into a zone-edge LO and a TA phonon [170]. Moreover, in this work, a 3 ps lifetime is measured for LO phonons in GaAs at the room temperature. According to this lifetime value for LO phonon, we can conclude that in our signal after 3 ps most of LO phonons decay into other phonon modes. It means that the resultant phonons should be taken into account in interaction with electrons. Therefore, those phonons are dominant roles in long relaxation time of the excited electrons in 800 and 750 nm. It should be mentioned that in GaAs decay to LA phonons is less probable due to low density states of phonons in that range of energy where for other III-VI semiconductor compounds different decay channel can occur [167].

A strong reduction in the relaxation times of electrons are observed for 720 nm and 700 nm such that τs approach around 4 ps and 3.5 ps respectively. This behavior can be explained by the intervalley scattering which is provided by large wavenumber or the edge-zone phonons. Presence of these of phonons, as explained already, is due to the decay of LO phonons. The backscattering into the main valley and the zone-edge phonon

emission provide a effective manner for the electrons to lose the energy. Energy of the zone-edge phonons whether optical or acoustic are similar according to phonon dispersion energy of GaAs. The excited electrons having more than 0.25 eV (the difference between minima in Γ and L valley) in the conduction band are able to be scattered to the L valley and thus, the Frohlich interaction or deformation potential will not be the only mechanisms of the electron relaxation in this range of energy. Moreover, electron-LO phonon interactions whether in form or Frohlich interaction or deformation potential are weakened for high energy as can be seen in figure 3.5 and figure 5.7. Therefore, in the mentioned range of excitation electron energy, two different channels of energy dispersion reduce the relaxation time of the electrons. The electrons need at least 0.45 eV energy in the conduction band provided by a pump beam with 660 nm wavelength to scatter to X valley.

The summarized relaxation time (RT) for sample A is listed in table 5.1 versus the wavelength and the excess energy is calculated with

$$E_{exc} = E_{pump} - E_{gap}, \tag{5.4}$$

where E_{exc} is the excess energy of electrons in the conduction band, E_{pump} the energy of the pump and E_{gap} band gap energy of GaAs that is taken 1.42 eV. In this approximation the curvature of bands are not considered. Our results show very good agreement with

Table 5.1: The RT of the excited electron for sample A at different wavelengths

Wavelength	Excess Energy	RT
800 nm	0.13 eV	12 ps
750 nm	0.23 eV	11 ps
720 nm	0.30 eV	4 ps
700 nm	0.35 eV	3.5 ps

reported data obtained experimentally and from simulation. For example, an ab-initio simulation is performed in ref.[132], showing that there are two specific energies associated to the minimum energy to occur the intervalley scattering to L and X valley that strong decays are observed as shown in Figure 5.8. Moreover, a decreasing behavior in the life time of electron is predicted by increasing the electron energy in this work.

Besides, the same reduction in life time of electrons in the conduction band have
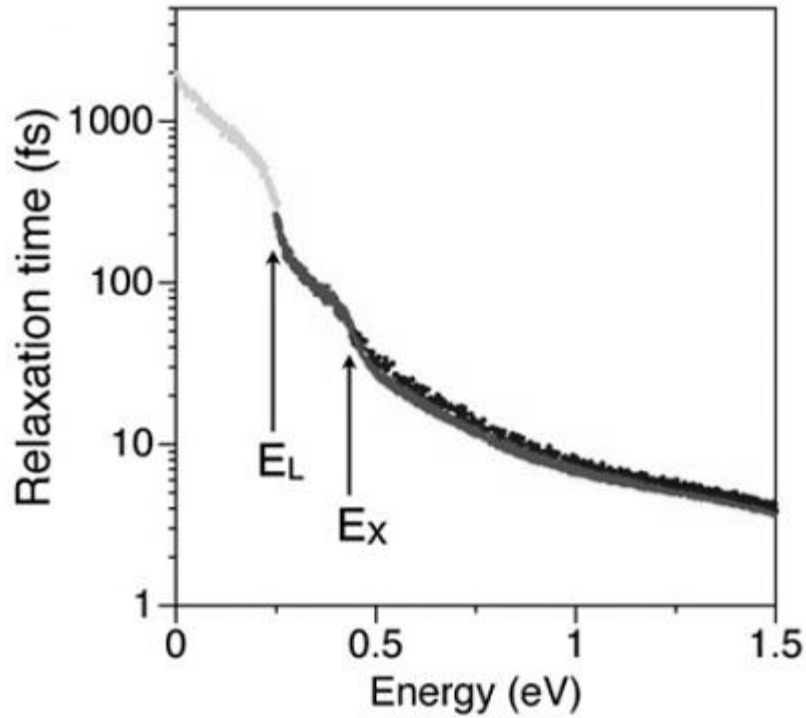
Figure 5.8: The simulated relaxation times of electrons versus energy in GaAs. [132]. The reduction tendency of relaxation time by energy is clear in this figure. E_L and E_X are the necessary energies for intervalley scattering from Γ valley to L and X valley, respectively. Also, yellow line is relevant to RT of the electrons in Γ valley. The Green line is related to the energy range in which scattering to L valley occurs together with the associated RT. The blue and red line present the relaxation time of scattered electron in L and X valley, respectively.

(a)

(b)
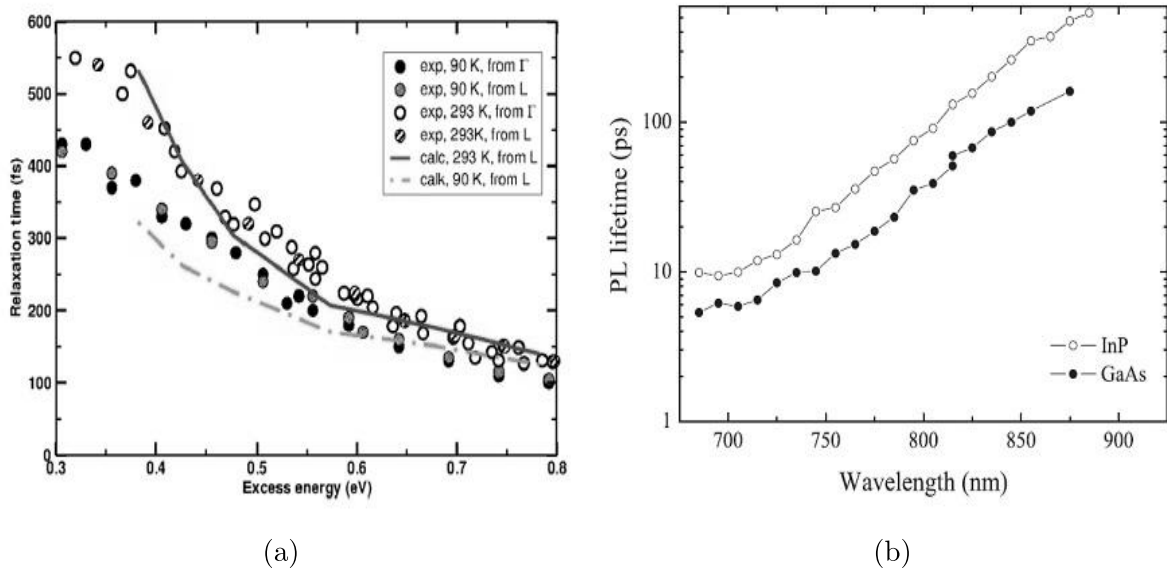
Figure 5.9: (a) The relaxation time measurement using photoemission method [119] and (b) the lifetime of the photoluminescence of GaAs shows the high rate of energy relaxation of the electrons by increasing the excitation energy [132].

been reported using the photoemission method [121] in Figure 5.9a and the time-resolved

photoluminescence [93] in Figure 5.9b.

5.2.2   Effects of the doping levels

The same measurements are conducted for the other samples containing different doping

levels. Notice that the thickness of samples are different from sample A and the care

should be taken that the pump does not penetrate inside the substrate. Therefore, 720

nm and 700 nm are used for the excitation and probe beams for the samples. Similar to

the results shown in Figure 5.4, one can observe a transient rise of the signal after the zero

delay time due to band filling and then a decay followed the peak which is understood

as energy relaxation. The obtained fit parameters show that a decay time around 4.5 ps
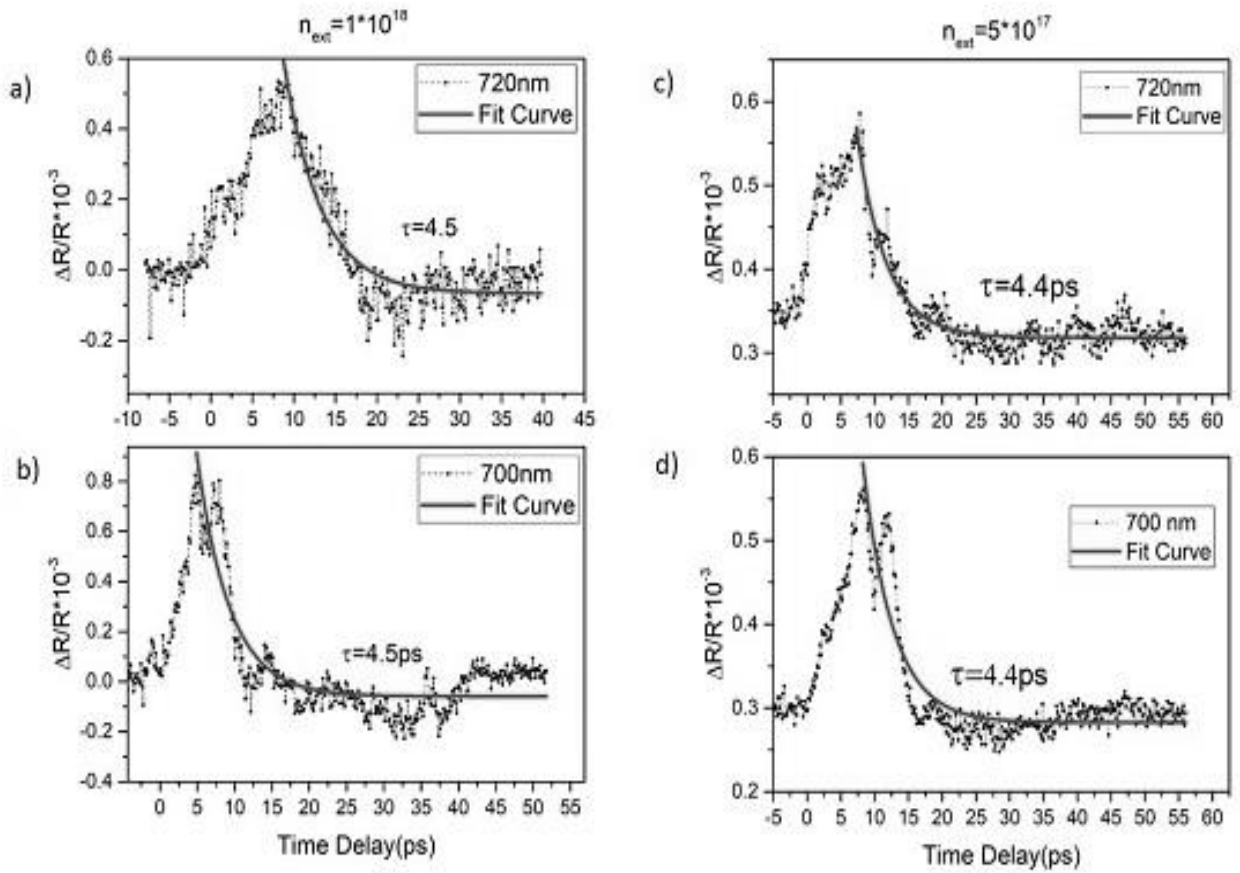
Figure 5.10: Differential reflectivity for GaAs: a)720 nm and b)700 nm for sample B and c)720 nm and d)700 nm for sample C.

for sample B and C, revealing the doping level does not make significant effects on the

relaxation time of the excited electrons, at least in the intermediate-level of concentration.

Also, it is found that the relaxation time is less dependent on the excitation wavelength comparison with sample A, as the results show quite same values for 700 nm and 720 nm. Interestingly, still the rise times are dependent on the excitation energy and the same tendency is observed from a 10 ps for 720 nm to 5 ps for 700 nm. In the same explanation for sample A, we believe the intervalley scattering is the main reason for this behavior.

To find a description for interpretation of the results of this section, a basic approach based on the Fermi energy is given. We already know that doping a semiconductor with other elements whether electron donor or acceptor, changes the Fermi level of energy such that

$$E_f - E_i = k_\beta T ln(\frac{n}{n_i}),\tag{5.5}$$

where E_f and E_i are Fermi level after and before of doping, k_β Boltzmann constant, T temperature, n doping concentration and n_i intrinsic electron concentration for a given semiconductor, respectively, which is shown in Figure 5.11. The Fermi level change due to doping level for samples A, B and C are 0.75 eV, 0.69 eV and 0.67 eV respectively. According to the GaAs band gap, the new Fermi energy for sample A lies in conduction
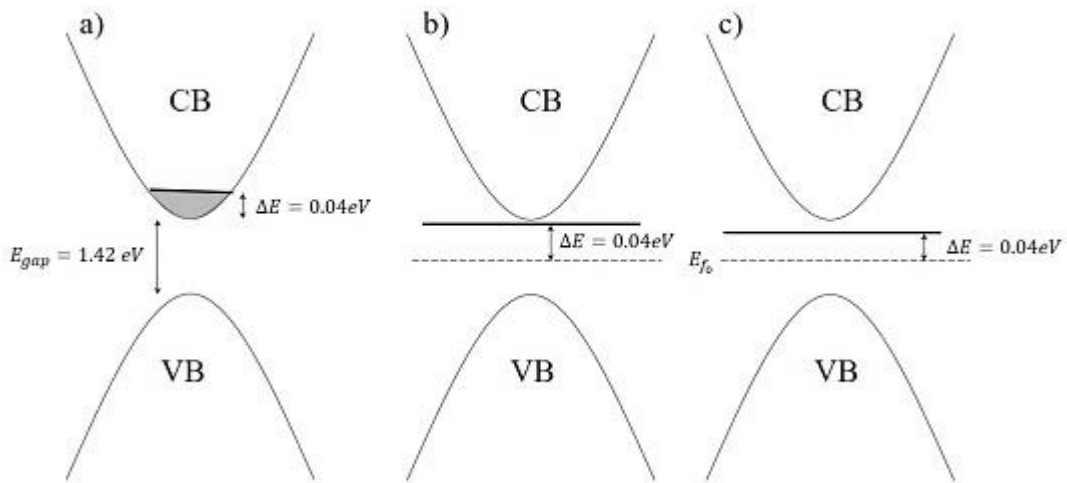
Figure 5.11: The energy band of the doped GaAs. The dash lines are the Fermi level without doping and the solid lines new Fermi levels.

band whereas for sample B and C the Fermi levels are still in the middle of band gap. We attribute the behavior to two possible mechanisms. The first one is that the excited

electrons and doped electrons interact together in a short time after the excitation. Since this interaction occurs in less than 100 fs, the setup is not able to resolve this scattering and its effects. The second idea is based on the large difference between the Fermi level and energy of the hot electrons. These two systems suggest the formation of two separated ensemble of electrons with different temperatures. The electron ensemble with high temperature release their energy by interaction with the lattice and add to the Fermi sea of electron energy states.

There is another work showing the same behavior for GaAs (110) by secondary electron (SE) method [50]. It is understood that remaining electrons in the conduction band and the excited electrons, particularly those with high energy, do not interact with each other which can be a proof for the second mentioned suggestion.

In summary, based on the results listed in table 5.2, it is turned out that residual energy has major contribution on the relaxation time of electrons and doping levels and consequently Fermi level of energy does not play an important role in the dynamics of the high energy electrons.

Table 5.2: The relaxation time of the excited electron for three different doping levels of GaAs at different wavelengths

Sample	RT at 720 nm	RT at 700 nm
A	4 ps	3.5 ps
B	4.5 ps	4.5 ps
C	4.4 ps	4.4 ps

5.2.3   Effects of the pump intensity

Figure 5.12 Shows $\frac{\Delta R}{R}$ of sample A for different pump intensities for 720 nm and 700 nm wavelength excitation. We pump the sample with different intensities to make different excited electron concentrations and study the effects of the density of electrons in the dynamics of them. Density of the excited electrons after light absorption is given by

$$n_{ext} = (1 - R)\frac{Q\alpha}{\pi d^2}, \tag{5.6}$$

where R is the reflectivity, Q the number of incident photons, α absorption coefficient and d beam radius. The n_{ext} for 720 nm at three different intensities 400 mw, 500 mw and 600 mw are approximately 8×10^{17} cm^{-3}, 1×10^{18} cm^{-3} and 1.2×10^{18} cm^{-3} and for 700 nm at intensities of 400 mw and 500 mw are 1×10^{18} cm^{-3} and 1.2×10^{18} cm^{-3} respectively. Sample A is selected because we are interested in studying the sample that the doping level and the generated electron density are of the same order. It is worth to note that thermal excitation even in high intensity is totally negligible because the absorbed density energy is low. Also, in this analysis the nonlinear absorption due to the band filling is neglected. It should be noted that the energy of the excited electrons is not as enough as that impact ionization or Auger recombination occurs. Impact ionization is a process in which a high energetic electron generates a pair of electron-hole [119]. A reduction in the decay times is observed as the pump intensity increases. This reduction for 700 nm is more intense such that the relaxation time is decreased from 6 ps to 1.5 ps for 400 mw and 500 mw. However, the relaxation times for 720 nm at 400 mw, 500 mw and 600 mw are 9 ps, 4 ps and 3.5 ps respectively. Also, the recovery of the signals to the initial value becomes more pronounced by the pump intensity increasing. This recovery is more obvious for 700 nm excitation.

We conclude that the decay time and the signal recovery are dependent on the density of the excited electrons. An explanation is that by increasing electron concentration, a band gap renormalization occurrs, reducing the band gap. As a result of that the electron need less energy to cross from the band gap and this increases the residual energy of the excited electrons. As stated in the electron-phonon interaction section, the higher the residual energy of the excited electrons, the faster energy relaxation of them. The form of recovery of signals show that for the lower intensity the signal has the negative values, while for the higher intensities the signal values are less negative or even positive. This behavior may be due to the many-body which is highly depend on the carrier concentration like band gap renormalization and Coulomb enhancement which reduce the signal value and band filling increasing the reflectivity [103]. Coulomb enhancement factor (CEF) is one the many-body effects in semiconductors that could be effective in the dynamics of the electrons. The theoretical surveys of CEF determine that

(a)   (b)
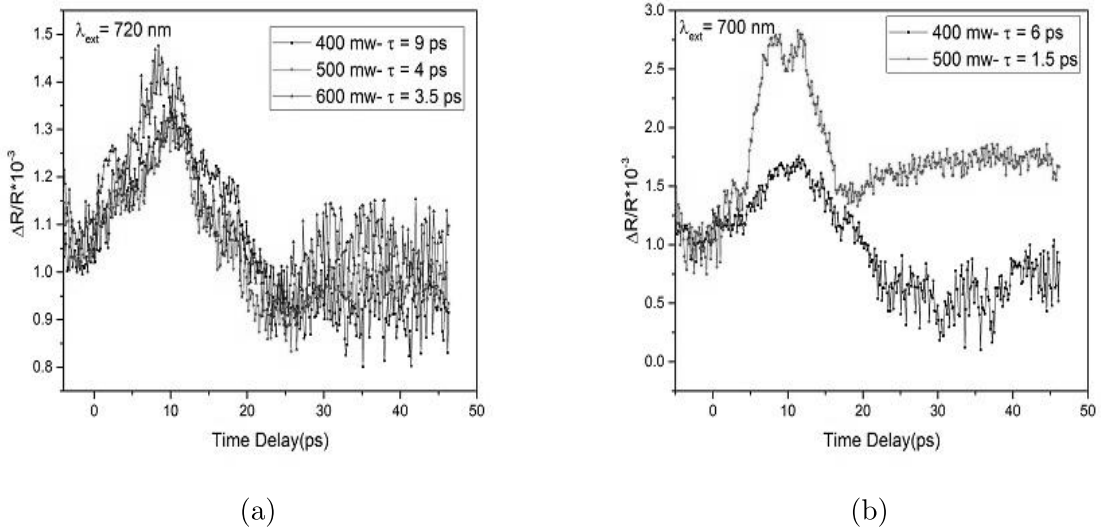
Figure 5.12: Differential reflectivity for sample A at different intensities, excited by a) 720 nm and b) 700 nm.

by increasing the electron energy this effect is decreased and becomes less dependent on the electron concentration as well [138]. Since the probe energy at 720 nm and 700 nm are far enough from the bottom of the conduction band the CEF is completely independent of carrier concentration. It means that we should not expect any change in the signals by variation of electron concentration made by CEF. However, the CEF leads to a small change in the $\frac{\Delta R}{R}$ values from 700 nm to 720 nm. The many-body effects which appeared due to the electrons in the bottom of the conduction band can be amplified for 700 nm excitation. Because the photons with this energy excite the electrons from the split-off band to the bottom of the conduction band. Therefore, short time after excitation the electron concentration in the low energy level is relatively high. Also, it is shown in some reports that the band-filling time is dependent of excitation density. The results represent values around 2 ps for redistribution of the carriers after excitation [158, 159].

Band gap renormalization and band filling is not distinguishable in our setup. Therefore, two effects have their roles in the dynamics of the electron simultaneously. The net signal which is highly depends on the electron concentration, the energy of the electrons, wavelength of the probe and the structure of energy band is a complex mix of all mentioned effects.

5.3   Summary

In the first section of this chapter, the simulations are performed to investigate the evolution of carrier concentration inside the sample by the time. For this aim, an ambipolar model is considered for diffusion of carrier in order to take in account the different mobility of electrons and holes in GaAs. The results show that in a degenerate pump-probe spectroscopy, the effects of diffusion is more remarkable with the pump and probe with shorter wavelength.

The result of time-resolved photoreflectivity for the sample with the high doping level reveal that the relaxation time of the excited electrons are highly depend on the energy of the electrons. The result show that the relaxation time decrease when the electrons excited with higher energy. Also, the relaxation time drops accelerate when the energy of electrons reach a minimum energy to scatter to the satellite valleys in the conduction band. In the second set of measurements, it is figured out that doping levels of GaAs with Si, providing more electrons inside the semiconductor, have no significant role in the energy relaxation of electrons. In the third part of experiment, the effects of excited electron concentration are studied in the GaAs sample. As the excited electron density increase, the relaxation time is reduced. This reduction is more pronounced in 700 nm excitation. The recovery of the induced changes in the reflectivity is another parameter that influenced by the electron density. The higher density of electron, the faster recovery of the signal.

As the measurement are performed in room temperature some effects like the exciton absorption is neglected in the result interpretations. In temperatures higher than the exciton formation temperature, the exciton spectrum are broadened and have so weak contribution on the optical properties [171].

6 Conclusion

A time-resolved differential reflectivity method is carried out to study the dynamics of the carriers in GaAs. To this aim, a pulsed laser with a 100 fs pulse duration is used in a pump-probe configuration to observe the happening events in samples in picosecond and sub-picosecond time regime. The samples are n-type GaAs grown on a GaAs substrate. The doping levels for samples are $5 \times 10^{17} \ cm^{-3}$, $1 \times 10^{18} \ cm^{-3}$ and $8 \times 10^{18} \ cm^{-3}$ Si concentration in order to investigate the effects of the doping levels on the dynamics of the electrons. Also, influences of the variation of the excitation energy and consequently the energy of the electron in the conduction band show that the relaxation time of the excited electrons decreases by increasing the energy of the electrons. The pump and probe have the same wavelength but with different intensities such that the pump intensity is so much higher than the probe one. The recorded changes in the probe intensity made by the pump beam reflect the optical modifications due to the excited electrons. The changes in the energy of electrons are applied with the variation of the pump wavelength. The selected wavelengths are based on the thickness of the samples and the energy band of GaAs. 800 nm, 750 nm, 720 nm and 700 nm are wavelengths which are used in the pump-probe setup for the sample with $1\mu m$ thickness. The result, for the sample with the highest doping, show a relaxation time reduction from 12 ps for 800 nm to 4 ps for 700 nm. The reduction of relaxation time becomes intensified for the wavelengths shorter than 720 nm where the electron transition from Γ valley to L valley is allowed. This transition, called intervalley scattering, accelerates the energy relaxation the electrons while for the wavelengths greater than 720 nm LO phonon-electron Frohlich interaction is the dominant mechanism for energy relaxation.

The other feature of the signals is the band filling time of the samples after excitation. The intervalley scatterings have influences on both the peak times or band filling time and the decay time, providing to the excitation energy is greater than the threshold value ($E_{\lambda_{800nm}}$). It is turned out that intervalley scattering keeps the electron more time in the satellite valleys but on the other hand increases the relaxation time of

them. Whereas the band filling time for 700 nm is around 5 ps. We suggest two possible mechanisms to explain such behavior. The first is the the excitation of electrons from the spilt-off valence band to the minimum point of the conduction band. The presence of electrons at the bottom of the main valley changes the electron distribution across the conduction band and weakens the band filling effect. The second interpretation is based on the diffusion effects which are more pronounced in shorter wavelength in a pump-probe setup. A theoretical investigation on diffusion of carriers in bulks GaAs is performed by the simulation. The simulations are realized with emphasis on an ambipolar model and the pump-probe setup specifications. Therefore, the effective concentration of carriers in the sample decrease remarkably near the surface samples and as a result of that reduces the band filling probability.

Besides, It is figured out that the doping levels of Si in the GaAs samples have no considerable effect on the dynamics of the excited electrons, particularly in the peak time and decay of the signals. We suggest that the difference energy between the Fermi levels formed by doping and the excited electrons is so high to interact to each other.

The other investigated factor is the concentration of the excited electrons. The high density of excited electron decreases considerably the relaxation time. Another effect of the excited electron density is the recovery of the nonlinear effects which is more pronounced in the high density.

If we consider GaAs as a main medium in a energy harvesting application, a trade off should be taken between the wavelength and intensity of excitation to improve the efficiency of the sample for carrier generation. An electron ensemble which excited by the energy near to band gap has the longer life time compared with those that are excited with the higher energy. Whereas the increasing density of electron can reduce the lifetime of the excited electrons. Also, the energy near to the transition from Γ and L point is found a crucial energy where the band filling time is around 10 ps, 2 times more than the other excitation energies. This higher time, keeps the sample in a saturated absorption situation and prevents more carrier generation. However, this feature can be useful for those applications in which a longtime optical nonlinearity is needed.

Appendices

A Solution to the diffusion equation

Let consider an infinitive half space where $x > 0$ correspond to the inner part of a material and $x < 0$ is vacuum. The diffusion equation for such system in given by [157]

$$\frac{\partial}{\partial t} N(x,t) = D\frac{\partial^2}{\partial x^2} N(x,t) \tag{A.1}$$

where N is carrier concentration, x and t are space and time, respectively. Now, the boundary should be satisfied as follows:

1- carriers should be in the $x > 0$ region. This condition can be performed mathematically such that:

$$\frac{\partial N(x = 0^+, t)}{\partial x} = 0. \tag{A.2}$$

2-Carrier density decrease exponentially from the sample surface which is given by:

$$N(x,0) = N_0 e^{-\alpha x} \tag{A.3}$$

With the mentioned boundary conditions, equation A.1 can be solved using Fourier/Laplace transform techniques, and the final solution is given by

$$N(x,t) = \frac{N_0}{2} e^{\alpha^2 Dt} [e^{-\alpha x} erfc(\frac{2\alpha Dt - x}{\sqrt{4Dt}}) + e^{\alpha x} erfc(\frac{2\alpha Dt + x}{\sqrt{4Dt}})] \tag{A.4}$$

where erfc is the complementary error function.

B Published and submitted articles
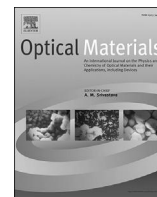
The effect of excitation intensity variation and silver nanoparticle codoping on nonlinear optical properties of mixed tellurite and zinc oxide glass doped with Nd_2O_3 studied through ultrafast z-scan spectroscopy

L. Moreira [a], R.F. Falci [a], H. Darabian [a], V. Anjos [a], M.J.V. Bell [a, *], L.R.P. Kassab [b], C.D.S. Bordon [c], J.L. Doualan [d], P. Camy [d], R. Moncorgé [d]

[a] Laboratório de Espectroscopia de Materiais, Departamento de Física, Universidade Federal de Juiz de Fora, Juiz de Fora-MG, Brazil
[b] Laboratório de Tecnologia em Materiais Fotônicos e Optoeletrônicos, Faculdade de Tecnologia de São Paulo, CEETEPS/UNESP, São Paulo, Brazil
[c] Departamento de Engenharia de Sistemas Eletrônicos, Escola Politécnica da USP, São Paulo, SP, Brazil
[d] Centre de recherche sur les Ions, les Matériaux et la Photonique (CIMAP), UMR, CNRS-CEA-Ensicaen, Universite de Caen, 6 Boulevard Maréchal Juin, F-14050, Caen, France

ABSTRACT

The research on Nd^{3+} doped new solid-state laser hosts with specific thermo-mechanical and optical properties is very active. Nd^{3+} doped tellurite glasses are suitable for these applications. They have high linear and nonlinear refraction index, wide transmittance range. The TeO_2-ZnO (TZO) glass considered in the present work combines all those features and the nonlinear optical properties can be used for the development of Kerr-lens mode-locked sub picosecond lasers. Recently the laser performance of Nd^{3+} doped TZO glass and was reported and laser slope efficiency of 21% was observed. We investigate how the intensity variation and the silver nanoparticles codoping affects the nonlinear optical properties of Nd^{3+} doped TZO glasses. Intensity dependent nonlinear refraction indices coefficients at 750, 800 and 850 nm were observed. The nonlinear optical features were obtained through ultrafast single beam z-scan technique with excitations at 750, 800 and 850 nm and are up to two orders of magnitude higher than those reported in the literature.

© 2018 Elsevier B.V. All rights reserved.

1. Introduction

Nd^{3+} doped laser materials have a wide variety of applications such as short pulse with high peak power laser systems. Thus, they are very attractive and extensively studied. Also, they have a very interesting ensemble of features, namely, easier 4-levels laser operation mode and usually higher gain cross sections if compared to Yb^{3+} doped laser materials [1]. Even though laser action of Nd^{3+} has been observed in a many solid media such as Nd:YAG systems, the research on Nd^{3+} doped new solid-state laser hosts with specific thermo-mechanical and optical properties is very active. This is the case of some Nd doped nonlinear tellurite glasses [2–8]. They have a conjunction of good thermo-mechanical properties, typical

of crystals, and broad-band spectral properties, typical of glasses. Also, a very interesting combination of large nonlinear refraction index (25 times larger than that of silica), wide transmittance range [9].

Usually, crystalline laser hosts lead to higher absorption and emission cross sections, while glasses are produced in larger volumes with optimal optical quality at lower cost. In order to minimize the non-radiative multiphonon relaxations and to optimize the quantum efficiency of the $^4F_{3/2} \rightarrow {}^4I_{11/2}$ emission of Nd^{3+}, it is also suitable to work with Nd^{3+} doped host materials with low contents of OH impurities. In that sense, laser emission of Nd^{3+} in glasses has been reported in fluorides [10–12], chalcogenides [13], aluminosilicates [14], germinates [15], and, as just mentioned, in tellurite glasses [2–6]. Among oxi-tellurites, the TeO_2-ZnO glass which is considered here in the present article combines good mechanical stability, chemical durability, high linear refraction index together with a wide transmission window (0.4–6 μm) and a

---

high rare-earth solubility [10,16,17]. The large linear refraction index (1.97) [18] of this tellurite glass imply large stimulated emission cross-sections, sometimes larger than for phosphate glasses [19]. These glasses also have high nonlinear optical properties, which can be used advantageously for the development of Kerr-lens mode-locked sub picosecond lasers.

These tellurite glasses have been also studied recently for the possibility of using thin films for the fabrication of rib waveguides [20]. The possibility of increasing the luminescent quantum yield of rare-earth ions by codoping TeO_2-ZnO glasses with silver nanoparticles [21,22] showed that they are potential materials for photonic devices applications. Recently it was demonstrated the reversible memory phenomena in Au-nanoparticles-incorporated TeO_2−ZnO films [23]. Also, encouraging improvements have been reported regarding the laser performance of a Nd^{3+} doped TZO (TeO2-ZnO) glass [24,25]. In this work, laser slope efficiency of 21% was observed. Thermo-optical properties of tellurite glasses codoped with rare Earth ions and metallic nanoparticles have also been reported [26–28].

These results motivated the present study that reports how the incident intensity variation and the silver nanoparticles codoping affects the nonlinear optical properties of Nd^{3+} doped TZO glasses.

Measurements were carried out with the Z-scan technique. The results displayed high intensity dependent nonlinear refraction indices at the wavelength range of 750−850 nm, at 80 MHz repetition rate and 100 fs pulses.

2. Experimental details

Glasses with the composition 85%TeO2-15%ZnO (wt.) (TZO) were obtained with the addition of 1% Nd_2O_3 and 1% $AgNO_3$ (wt.) (TZO:1%Nd:1%Ag). Also a sample without $AgNO_3$ (TZO:1%Nd) was prepared to be used as reference Reagents were melted at 800 °C in an platinum crucible for 20 min, quenched in a pre-heated brass mold, annealed at 325 °C for 2 h, and cooled down to room temperature during 2 h to avoid internal stresses. At the end of the fabrication process, an additional heat treatment was performed for 24 h, to the sample produced with $AgNO_3$ to thermally reduce the Ag^+ ions to Ag^0 and nucleate silver nanoparticles, following the procedure already reported [21,22]. Through this procedure it was possible to obtain high quality samples, with even distribution of the dopants within the glass matrix (TZO).

Absorption spectra were measured in a Perkin-Elmer LAMBDA 9 spectrophotometer in wavelength range from 350 to 1000 nm.

A 200 kV transmission electron microscope (TEM) was employed to investigate the presence of nanoparticles in the samples.

The nonlinear optical features were obtained through ultrafast single beam z-scan setup displayed in Fig. 1. The excitation beam is a Mai Tai HP, Ti:Sapphire NIR, 100 fs, 80 MHz pulsed Gaussian beam linearly polarized. A Glan-Laser linear polarizer (GL5) positioned at the laser output controls the output intensity. Just after the GL5, a lens focuses the excitation beam in the sample posed on a displacement stage. After crossing the sample the beam goes through the aperture that is set either open or partially (50%) closed depending on the experiment needs − nonlinear refraction demands closed aperture, while nonlinear absorption demands open aperture. Then, the beam crosses a lens that collimates the signal into a silicon detector connected to a computer, by which the data acquisition is performed.

3. Absorption spectra and TEM imaging

The UV-VIS-NIR absorption (absorption coefficient) spectrum of the samples, registered between 350 nm and 950 nm is shown in Fig. 2. The features corresponding to the main absorption transitions of Nd^{3+} from $^4I_{9/2}$ fundamental level to excited levels $^4F_{3/2}$(890 nm), $^4F_{5/2}+^2H_{9/2}$(808 nm), $^4F_{7/2}+^4S_{3/2}$(750 nm), $^4F_{9/2}$(690 nm), $^4G_{5/2}+^2G_{7/2}$(580 nm) and $^4G_{7/2}+^4G_{9/2}+^2K_{13/2}$ have been identified and highlighted in the figure. As expected for a glass, the absorption features appear as broad bands. Also it is interesting to notice that the addition of silver nanoparticles (TZO:1%Nd:1%Ag) to the initial composition (TZO:1%Nd) have resulted in a reasonable enhancement of the absorption. This effect may be attributed to the
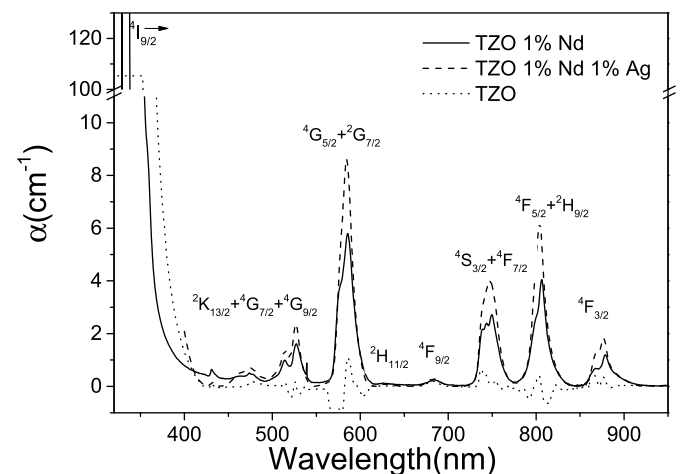

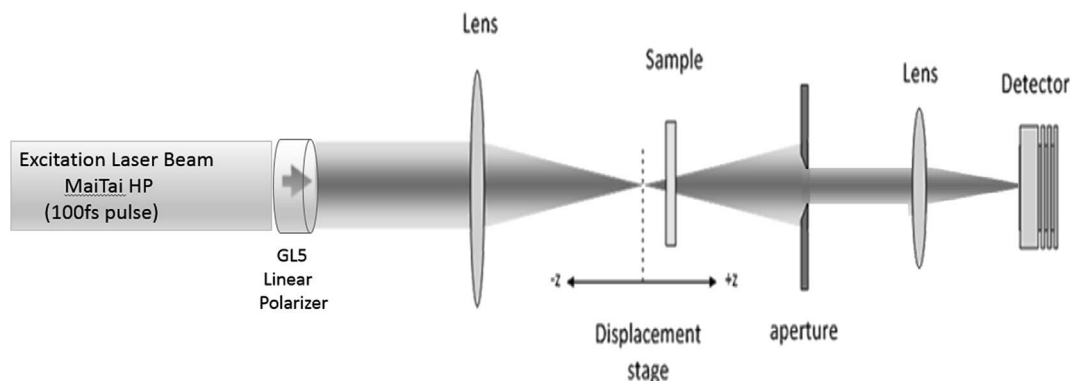Fig. 2. UV−Vis−NIR absorption spectra for TZO doped and undoped samples.

Fig. 1. Z-scan experimental setup [28].

Table 1
TZO samples parameters.

Sample	Thickness l(mm)	Linear absorption coefficient α_0(cm^{-1})	Wavelength (nm)
TZO:1%Nd	1,65	2,64	750
		2,61	800
		0	850
TZO:1%Nd:1%Ag	2,98	3,91	750
		4,94	800
		0	850

modification of the Nd^{3+} ion environment due to the presence of Ag nanoparticles. 29 Furthermore, when the TZO:1%Nd and TZO:1%Nd:1%Ag samples are compared with the matrix (TZO) it is possible to notice the absence of optical absorption above 500 nm. The linear absorption coefficients (α) correspondent to the chosen excitation wavelength for each sample can be found at Table 1.

Fig. 3 (left) presents TEM images of TZO:1%Nd:1%Ag sample that assures the existence of the silver nanoparticles. We observe isolated silver nanoparticles with average size of 20 nm. Fig. 3 (right) shows the simulated absorption spectra for 20 nm silver nanoparticles embedded TZO glass, where two resonant plasmons at 425 and 500 nm are evidenced [30].

4. Nonlinear refraction

Nonlinear refraction of the samples was examined with the aid of the z-scan setup depicted on Fig. 1. To evaluate the nonlinear refraction of a transparent medium the aperture should be set partially closed, thus known as closed aperture (C.A.) experiment. Namely, the aperture is set open by 40%, to let only the center of the spot at far field pass to the detector.

Figs. 4–6 display the normalized transmittance for the samples TZO:1%Nd and TZO:1%Nd1%Ag. Since the TZO sample has not shown any optical nonlinear behavior for the wavelengths analyzed here, there is no available data. The experiments were carried for the excitation intensities within the range 0.05–0.45 GW/cm^2. No higher intensity was available due to limitations of the system, including the damage limit threshold for the samples TZO:1%Nd and TZO:1%Nd1%Ag. The samples were excited at 750, 800 and 850 nm. The different wavelengths used for excitation and presented in Figs. 4–6 have been based on the nonlinear optical

refraction responses detected. The TZO:1%Nd sample showed higher sensitivity at 750 and 800 nm, whereas TZO:1%Nd:1%Ag at 800 and 850 nm. This difference can be attributed to the silver nanoparticles interaction with the matrix TZO.

The 3rd order nonlinear refraction effect could be observed just for the TZO:1%Nd and TZO:1%Nd1%Ag samples. Additionally, no relevant nonlinear absorption was observed at any of the tested samples. Thus, the data obtained from these measurements were fitted to the following expression [31,32]:

$$\Delta T_{PV} \cong 0,406(1 - S)^{0,27}|\Delta\Phi_0| \tag{1}$$

$$\Delta\Phi_0 = \left(\frac{2\pi}{\lambda}\right)Z_0 I_0 n_2 l_{eff}, \quad l_{eff} = \frac{1 - e^{-\alpha l}}{\alpha}, \quad Z_0 = \frac{\pi\omega_0^2}{\lambda} \tag{2}$$

where $\Delta T_{PV} = T_P - T_V$ is the change in transmittance between the peak and valley, and T_P and T_V are the normalized peak and valley transmittances, $\Delta\Phi_0$ is the nonlinear phase with the sample at the focus, Z_0 is the Rayleigh length, Z the sample position relative to the focus (Z = 0 mm), λ is the excitation laser wavelength, n_2 is the 3rd order nonlinear refraction index and I_0 is the peak intensity, ω_0 is the beam waist at the focus, S is the transmittance of the aperture in the absence of a sample, here $S = 0,4$.

Figs. 4–6 show a similar nonlinear behavior of the samples, self-focusing Kerr lenses in all cases studied. The amplitude of the signal denotes the value $\Delta\Phi_0$. The TZO:1%Nd results at 750 nm (Fig. 6A) and 800 nm (Fig. 5A), evidence that $\Delta\Phi_0$ increases with rise of the excitation intensity, but for 850 nm (Fig. 4A) the reverse situation is observed. The TZO:1%Nd1%Ag sample exhibits the same nonlinear optical behavior for the three excitation wavelengths but with higher amplitudes, indicating that the presence of the silver nanoparticles in the TZO:1%Nd 1%Ag enhanced the nonlinear optical features.

The results of the 3rd order nonlinear refraction index (n_2) as function of the excitation intensity, are shown in Fig. 7. It is possible to notice that n_2 shows an exponential decay behavior with the rise of I_0. We observe high values for n_2 that reaches 4×10^{-12} cm^2/W, at 850 nm (0.05 GW/cm^2), for the sample with silver nanoparticles whereas in the absence of silver nanoparticles n_2 is significantly lower, around 2×10^{-13} cm^2/W. It was observed enhancement of about 50%, in the presence of silver nanoparticles, at 800 nm, for the same excitation intensity (0.3 GW/cm^2). Furthermore, a fitting
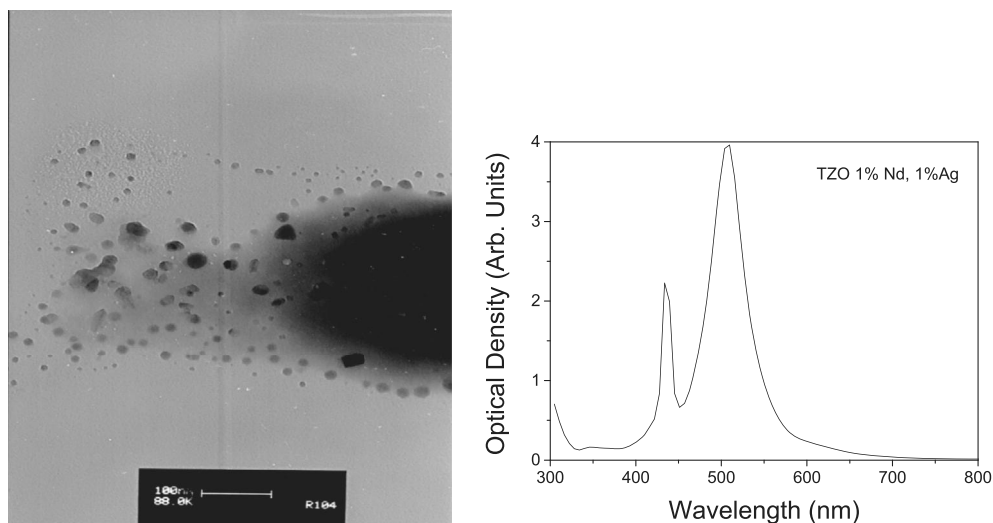
Fig. 3. TEM Image of the TZO:1%Nd:1%Ag (left) and the Simulated absorption spectra for 20 nm Silver Nanoparticles embedded at TZO glass [29](right).
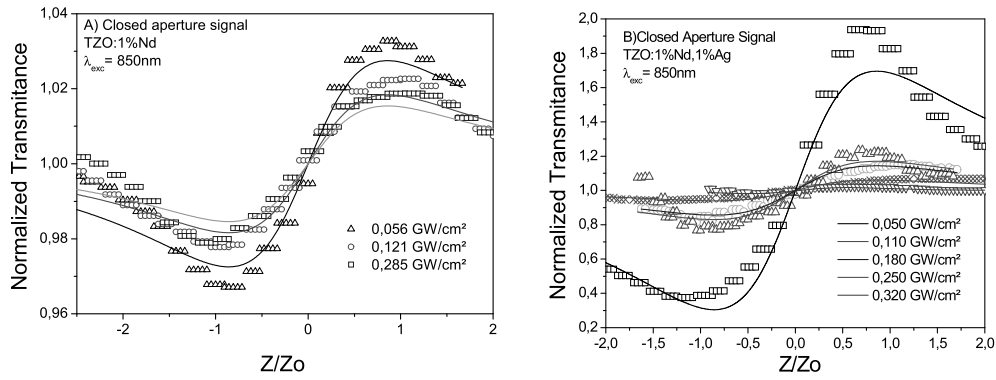
Fig. 4. Closed Aperture (C.A.) Z-scan signal at 850 nm **for different excitation intensities.**
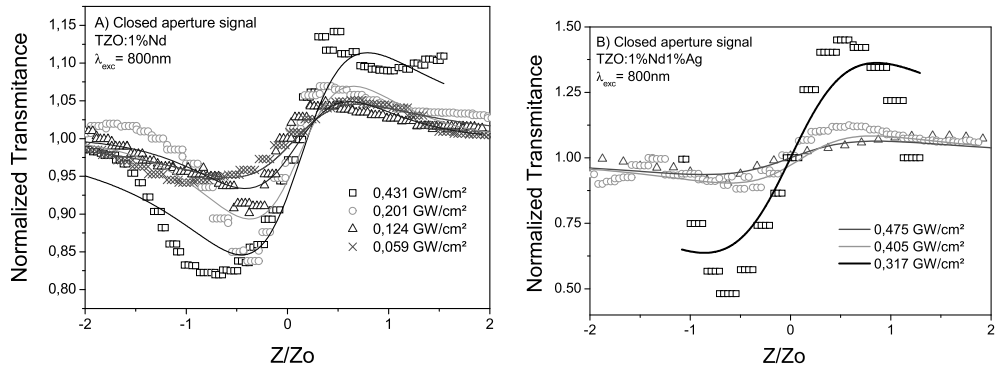
Fig. 5. Closed Aperture (C.A.) Z-scan signals at 800 nm **for different excitation intensities.**

was performed using the empirical expression (3) in order to obtain the 3rd order nonlinear refraction indices for high intensity excitation, $n_{2,\infty}$. The results are displayed in Table 2.

$$n_2(I_0) = n_{2,I} \exp(-I_0/I_{n2}) + n_{2,\infty} \tag{3}$$

In the equation above $n_2(I_0)$ is the 3rd order nonlinear refraction index as function of the excitation intensity I_0, $n_{2,I}$ is the amplitude, I_{n2} is the decay constant and $n_{2,\infty}$ is the 3rd order nonlinear refraction index at high intensity excitation.

Regarding the $n_{2,\infty}$, it is possible to observe a significant rise at 850 nm with addition of silver nanoparticles. However, for the lower excitation wavelengths, $n_{2,\infty}$ is diminished roughly by half. Even though this result is unexpected, we should consider the fact that the addition of metallic nanoparticles to an emission media,

should favor radiative transitions over other energy transfer processes. In fact, 750 nm and 800 nm lay among pumping wavelengths for the Nd^{3+} ion, as can be seen in Fig. 1. Thus it is possible to expect a significant enhancement in emission, when silver nanoparticles are added.

The evolution of the nonlinear indices with the increasing intensity have been observed and discussed before, even if not analyzed mathematically. The behavior of n_2 variation due to increasing excitation intensities have been reported by A.S. Reyna and C. B. de Araujo [33] and also by R.A.Ganeev et al. [34]. They reported as the most likely reasons for the n_2 changes due to excitation rise:

(1) Interband transitions taking into account the possibility of two-photon process [34]. This process can be taken into
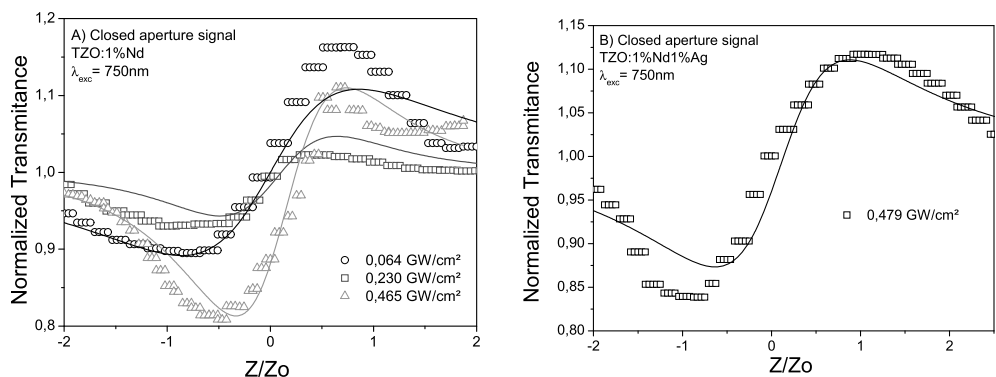
Fig. 6. Closed Aperture (C.A.) Z-scan signals at 750 nm **for different excitation intensities.**
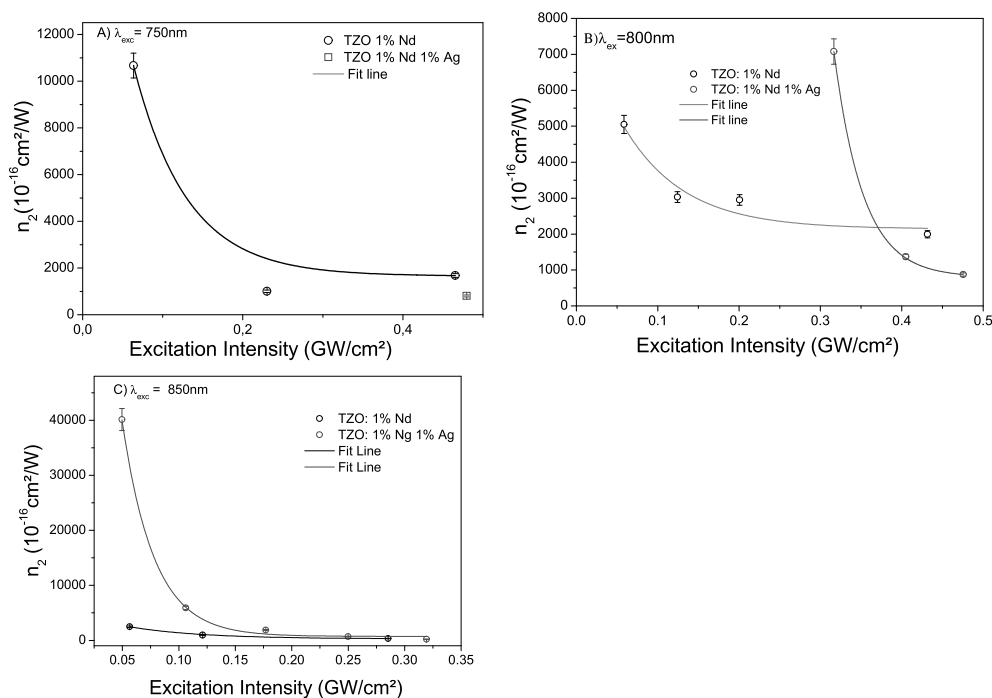
Fig. 7. **Nonlinear Refraction Index (n$_2$)** as Function of the Excitation Intensity at A) 750 nm, B) 800 nm, C) 850 nm.

Table 2
TZO nonlinear refraction indices (n$_2$) as function of the excitation intensity (I$_0$).

$n_2(I_0) = n_{2,I}\exp(-I_0/I_{n2}) + n_{2,\infty}$

Sample	Wavelength(nm)	$n_{2,\infty}(10^{-14}\,cm^2/W)$	$n_{2,I}(10^{-13}\,cm^2/W)$	I$_{n2}$(GW)
TZO:Nd	750	16,584	23,356	0,067
	800	21,411	6275	0,045
	850	2655	5355	0,063
TZO:Nd:Ag	750	8073		
	800	8008	4.383,840	0,036
	850	7188	229,350	0,028

consideration for the TZO:1%Nd1%Ag sample since it has shown resonance plasmon at 425 nm and was excited at 850 nm.

(2) Thermal effect. Positive contribution to the nonlinear refractive index can be caused by thermal effect, which can be considered as a result of energy transfer from heated dopant to surrounding dielectric matrix. However, the time necessary for this process to be important corresponds to a few nanoseconds, whereas the pulse duration was five orders shorter (100 fs), which diminishes the influence of the thermal effect causing the acoustic-induced variation of density and refractive index of matrix [34].

(3) The irreversible change of n$_2$ caused by laser radiation. This effect was analyzed in several studies of composite materials doped with copper and silver nanoparticles. The mechanism responsible for the change was a photochemical reaction, which produced a silver-oxide layer on the surface of nano-clusters. The irreversible changes in both studies were caused by a thermal influence produced by high pulse repetition rate radiation [33]. In our case, the Z-scans had a good reproducibility in time, so the influence of irreversible changes can be easily excluded.

It also possible to evaluate the results of *n$_2$* for similar materials.

S.K.Mahajan reported $n_2 = 1.21 \times 10^{-15}\,cm^2/W$, at 800 nm, 100 fs, 80 MHz, for a Er^{3+} doped TeO_2-Li_2O-WO_3 glass [35]. Nonlinear refraction indices of PbO-Nb_2O_5-TeO_2 glasses at 800 nm,90 fs, 1 kHz were studied recently; nonlinear refraction indices in the range 1.42-$1.78 \times 10^{-14}\,cm^2/W$ were obtained for different concentration of PbO-Nb_2O_5-TeO_2. Another interesting result has been obtained by K. Kato [36], who studied the optical nonlinearities of $20Ag_2O$–$80TeO_2$ glasses, their highest value was $n_2 = 8.75 \times 10^{-15}\,cm^2/W$, at 800 nm,90 fs,1 kHz.

D.Linda observed the role of silver nanoparticles on nonlinear optical properties at TeO_2–Ti_2O–Ag_2O and TeO_2–ZnO–Ag_2O ternary systems [37]. The silver nanoparticles increased the energy transfer among the ions that build the matrix generating enhancement of *n$_2$* ranging from 28 to $40 \times 10^{-14}\,cm^2/W$ at 800 nm, 90 fs, 1 KHz. Goméz observed the nonlinearities of silver nanoparticles in colloidal media, and obtained *n$_2$* around $10^{-15}\,cm^2/W$(533 nm,8ns, 10 Hz) and linear absorption peak around 500 nm [38]. In the present study we have added 20 nm silver nanoparticles to the original composition of TZO:1%Nd. Through simulation [29] it was possible to obtain the nanoparticles absorption spectrum embedded in TZO:1%Nd medium, available at Fig. 6. We can observe two peaks, around 425 nm and 500 nm. This would justify the enhanced sensibility at 850 nm, for the sample prepared with silver nanoparticles.

Then comparing the results recently reported we conclude that the samples presented in this work have nonlinear refraction indices that are at the same order or up to two orders of magnitude higher than those reported to tellurite glasses in the 750—850 nm range.

5. Conclusion

The nonlinear optical properties of Nd^{3+} doped TZO glasses with and without silver nanoparticles is studied. The nonlinear optical features were obtained through ultrafast single beam z-scan technique. The samples were excited at 750, 800 and 850 nm. The 3rd order nonlinear refraction index (n_2) shows an exponential decay behavior with the rise of the excitation intensity. Then it reaches a constant value at high intensity values. In comparison to the glasses available in the literature, the samples presented in this work have nonlinear refraction indices that at the same order or up to two orders of magnitude higher than those reported to tellurite glasses in the 750—850 nm range. The enhanced nonlinear refraction index due to the increased local field that surrounds the silver nanoparticles could be observed. The high nonlinear properties of the samples presented here make them good candidates for subpico Kerr effect based lasers. Likewise, they demand further examinations such as recovery time and damage threshold to better define the potential for possible applications.

References

[1] Solid-State Lasers/Nd lasersF. Träger (Ed.), Handbook of Lasers and Optics, Springer, New-York, 2007, pp. 636—648.
[2] J.C. Michel, D. Morin, F. Auzel, Propriétés spectroscopiques et effet laser d'un verre tellurite et d'un verre phosphate dopés en néodyme, Rev. Phys. Appl. 13 (1978) 859.
[3] A. Miguel, J. Azkargorta, R. Morea, I. Iparraguirre, J. Gonzalo, J. Fermamdez, R. Balda, Spectral study of the stimulated emission of Nd3+ in fluorotellurite bulk glass, Opt. Expr. 21 (2013), 009298.
[4] H. Kalaycioglu, H. Cankaya, G. Ozen, L. Ovecoglu, A. Sennaroglu, Lasing at 1065 nm in bulk Nd3+-doped telluride-tungstate glass, Opt. Commun. 281 (24) (2008) 6056—6060.
[5] I. Iparraguirre, J. Azkargorta, J.M. Fernández-Navarro, M. Al-Saleh, J. Fernández, R. Balda, Laser action and upconversion of Nd3+ in tellurite bulk glass, J. Non Cryst. Solids 353 (8—10) (2007) 990—992.
[6] N. Lei, B. Xu, Z.H. Jiang, Ti-sapphire laser pumped Nd-tellurite glass laser, Opt. Commun. 127 (4—6) (1996) 263—265.
[7] W. Ryba-Romanowski, S. Golab, L. Cichosz, B.J. Ttzebiatowska, Influence of temperature and acceptor concentration on energy transfer from Nd3+ to Yb3+ and from Yb3+ to Er3+ in tellurite glass, J. Non Cryst. Solids 105 (295) (1988) 15.
[8] J.S. Wang, E.M. Vogel, E. Snitzer, J.L. Jackel, V.L. da Silva, Y. Silberberg, 1.3 μm emission of neodymium and praseodymium in tellurite-based glasses, J. Non Cryst. Solids 178 (1994) 109.
[9] R.A.H. El-Mallawany, Tellurite Glasses Handbook-physical Properties and Data, CRC, Boca Raton, FL, 2001.
[10] R.R. Petrin, M.L. Kliewer, J.T. Beasley, R.C. Powell, I.D. Aggarwal, R.C. Ginther, Spectroscopy and laser operation of Nd:ZBAN glass, IEEE J. Quant. Electron. 27 (4) (1991) 1031—1038.
[11] J. Azkargorta, I. Iparraguirre, R. Balda, J. Fernández, E. Dénoue, J.L. Adam,

[12] J. Azkargorta, I. Iparraguirre, R. Balda, J. Fernández, On the origin of bichromatic laser emission in Nd3+-doped fluoride glasses, Opt. Expr. 16 (16) (2008) 11894—11906.
[13] T. Schweizer, D.W. Hewak, D.N. Payne, T. Jensen, G. Huber, Rare-earthdoped chalcogenide glass laser, Electron. Lett. 32 (7) (1996) 666—667.
[14] D.F. de Sousa, L.A.O. Nunes, J.H. Rohling, M.L. Baesso, Laser emission at 1077 nm in Nd3+-doped calcium aluminosilicate glass, Appl. Phys. B 77 (2003) 59—63.
[15] J. Fernandez, I. Iparraguirre, R. Balda, J. Azkargorta, M. Voda, J.M. Fernandez-Navarro, Laser action and upconversion of Nd3+ in lead-niobium-germanate bulk glass, Opt. Mater. 25 (2) (2004) 185—191.
[16] J.S. Wang, E.M. Vogel, E. Snitzer, Tellurite glass: a new candidate for fiber devices, Opt. Mater. 3 (3) (1994) 187—203.
[17] A. Jha, S. Shen, M. Naftaly, Structural origin of spectral broadening of 1.5-μm emission in Er3+ doped tellurite glasses, Phys. Rev. B 62 (10) (2000) 6215—6227.
[18] H.A.A. Sidek, S. Rosmawati, Z.A. Talib, M.K. Halimah, W.M. Daud, Synthesis and optical properties of ZnO-TeO2 glass system, Am. J. Appl. Sci. 6 (8) (2009) 1489—1494.
[19] M.J. Weber, Science and technology of laser glass, J. Non Cryst. Solids 123 (1—3) (1990) 208—222.
[20] V.D. Del Cacho, A.L. Siarkowsi, N. Morimoto, H.V. Borges, L.R.P. Kassab, Fabrication and characterization of TeO2-ZnO rib waveguides, ECS Trans. 31 (1) (2010) 219.
[21] L.R.P. Kassab, L.F. Freitas, T.A.A. de Assumpção, D.M. da Silva, C.B. de Araújo, Frequency upconversion properties of Ag: TeO2—ZnO nanocomposites codoped with Yb3+ and Tm3+ ions, Appl. Phys. B 104 (2011) 1029.
[22] T.A.A. de Assumpção, M.E. Camilo, L.R.P. Kassab, A.S.L. Gomes, C.B. de Araújo, N.U. Wetter, Frequency upconversion properties of Tm3+ doped TeO2—ZnO glasses containing silver nanoparticles, J. Alloys Compd. 536 (2012) S504—S506.
[23] L. Bontempo, S.G. dos Santos Filho, L.R.P. Kassab, Thin Solid Films 611 (2016) 21—26.
[24] M.J.V. Bell, V. Anjos, L.M. Moreira, R.F. Falci, L.R.P. Kassab, D.S. da Silva, J.L. Doualan, P. Camy, R. Moncorgé, Laser emission of a Nd-doped mixed tellurite and zinc oxide glass, J. Opt. Soc. Am. B 31 (7) (July 2014) 1590—1594.
[25] M.J.V. Bell, V. Anjos, L.M. Moreira, R.F. Falci, L.R.P. Kassab, D.S. da Silva, J.L. Doualan, P. Camy, R. Moncorgé, The effects of Nd2O3 concentration in the laser emission of TeO2-ZnO glasses, Opt. Mater. 58 (2016) 84—88.
[26] A.P. Carmo, M.J.V. Bell, V. Anjos, R. De Almeida, D.M. Da Silva, L.R.P. Kassab, Thermo-optical properties of tellurite glasses doped with Eu3+ and Au nanoparticles, J. Phys. D Appl. Phys. 42 (2011), 155404.
[27] A.P. Silva, A.P. Carmo, V. Anjos, M.J.V. Bell, L.R.P. Kassab, R. de Almeida Pinto, Temperature coefficient of optical path of tellurite glasses doped with gold nanoparticles, Opt. Mater. 34 (1) (2009) 239—243.
[28] E.A. Carvalho, A.P. Carmo, M.J.V. Bell, V. Anjos, L.R.P. Kassab, D.M. da Silva, Optical and thermal investigation of GeO 2—PbO thin films doped with Au and Ag nanoparticles, Thin Solid Films 520 (7) (2012) 2667—2671.
[29] Asmahani Awang, S.K. Ghoshal, M.R. Sahar, R. Arifin, Gold nanoparticles assisted structural and spectroscopic modification in Er3+-doped zinc sodium tellurite glass, Opt. Mater. 42 (2015) 495—505.
[30] Jon Camden, George C. Schatz, Nanosphere Optics Lab, 2016, https://doi.org/10.4231/D3Q814T3N. https://nanohub.org/resources/nsoptics.
[31] M. Sheik-Bahae, et al., IEEE J. Quant. Electron. 26 (1990) 760.
[32] E.W. Van Stryland, M. Sheik-Bahae, in: M.G. Kuzyk, C.W. Dirk (Eds.), Characterization Techniques and Tabulations for Organic Nonlinear Materials, Marcel Dekker, Inc., 1998, pp. 655—692.
[33] A.S. Reyna, C.B. De Araujo, High-order optical nonlinearities in plasmonic nanocomposites—a review", Adv. Opt. Photon 9 (4) (December 2017).
[34] R.A. Ganeev, et al., Saturated absorption and nonlinear refraction of silicate glasses doped with silver nanoparticles at 532 nm, Opt. Quant. Electron. 36 (2004) 949—960. Kluwer Academic Publishers. Printed in the Netherlands.
[35] Raouf A.H. El-Mallawan, Tellurite Glasses Handbook: Physical Properties and Data, second ed., CRC Press, 2016, p. 148.
[36] K. Kato, T. Hayakawa, Y. Kasuya, P. Thomas, J. Non Cryst. Solids 431 (2016) 97.
[37] D. Linda, et al., Optical properties of tellurite glasses elaborated within the TeO2—Tl2O—Ag2O and TeO2—ZnO—Ag2O ternary systems, J Alloys Compd. 561 (2013) 151—160.
[38] Goméz, et al., Influence of stabilizing agents on the nonlinear susceptibility of silver nanoparticles, J. Opt. Soc. Am. B 24 (9) (September 2007).

Thermal and nonlinear optical properties of Tm^{3+}-doped tellurite glasses

M. Seshadri[1] · M. Radha[1] · H. Darabian[1] · L. C. Barbosa[2] · M. J. V. Bell[1] · V. Anjos[1]

Abstract

In the present work, thermal and nonlinear properties of tellurite glasses doped with Tm_2O_3 were investigated by means of thermal lens, thermal relaxation and z-scan measurements. The composition of the samples was $(78 - x)$ TeO_2 + 4.5 Bi_2O_3 + 5.5 ZnO + 10.5 Li_2O + 1.5 Nb_2O_5 + xTm_2O_3 (x = 0.05, 0.1, 0.5, 1.0 and 1.5 mol%). Thermal diffusivity (D), specific heat (ρc), thermal conductivity (K) and optical path change with temperature (ds/dT) were determined as a function of Tm^{3+} concentration. Concerning thermal–optical properties, our results show that the 0.5 mol% Tm doped is the most suitable sample for laser applications as it presented the lowest ds/dT and highest thermal diffusivity (conductivity). Third-order nonlinearities were observed and discussed in 1.0 and 1.5 mol% samples. The nonlinear indices (n_2) found were 1.16×10^{-13} and 3.89×10^{-13} cm^2 W^{-1}, respectively. The data obtained show that the Tm^{3+}-doped TBZLN glasses have potential for future opto-electronic devices.

Keywords Tellurite glass · Thermal diffusivity · Thermal conductivity · Nonlinear refractive index

Introduction

Tellurium oxide (TeO_2)-based glasses are potential candidates for opto-electronic applications due to their unique characteristics, such as low phonon energy (750 cm^{-1}), high rare earth (RE) ion solubility, good transparency up to 5 μm and high optical nonlinearities compared with other host glasses [1, 2]. TeO_2 is a conditional glass former, as it does not form a glass itself [3]. Therefore, intermediate/network modifiers (ZnO, WO_3, Nb_2O_5, Bi_2O_3, Na_2O, etc.) are mixed with TeO_2 forming a wide range of glass types. The addition of modifiers significantly influences the electronic polarizability (or hyper-polarizability) of a lone pair of electrons in the Te^{4+} ions and the progressive transformation of TeO_4–TeO_3 units through intermediate TeO_{3+1} structural units. The pertinence of such a glass lattice modifiers is that they affect the nature of their third-order nonlinear (TONL) properties.

In recent years, the development of Er^{3+}-, Tm^{3+}- and Ho^{3+}-doped tellurite bulk glasses and fibres for radiation emission at wavelengths around 1.0, 1.5, 1.8-μm to longer than 2.0-μm region has significant interest for applications, such as telecommunications, eye-safe lasers, remote sensing, environmental monitoring and nonlinear optics [4–10]. Normally, the average output power obtained from solid-state laser diminishes due to heating of the gain element by nonradiative relaxation, which occurs during the pumping/oscillation cycle. The generation of heat also significantly reduces the efficiency of laser operation through thermo-optical aberrations, lensing and birefringence [11]. Therefore, in order to obtain efficient solid-state lasers, high radiative emission rate is required. Additionally, low generation of heating is important to avoid thermally induced distortion of a laser beam during its propagation through a medium [12].

The heat generation in rare earth-doped host glasses has been studied by thermal lens (TL) technique [13–18] which gives information about the heat flow by means of a direct

✉ M. Seshadri
   seshumeruva@gmail.com

✉ V. Anjos
   virgilio.anjos@ufjf.edu.br

1 Grupo de Engenharia e Espectroscopia de Materiais, Departamento de Fisica—ICE, Universidade Federal de Juiz de Fora, Juiz De Fora, MG 36036-900, Brazil

2 IFGW, Universidade Estadual de Campinas, Campinas, SP, Brazil

measurement of thermal diffusivity (D). The thermal diffusivity (D) together with thermal conductivity (K) plays an important role on the performance of optical devices. They are interconnected through the relation $K = \rho c D$, where c is the specific heat and ρ is the density of the sample, respectively. Moreover, there is a lack of thermal data (ds/dT, D and K) for optical glasses. In this work, Tm^{3+}-doped tellurite (TBZLN) glasses were characterized through thermal lens, thermal relaxation and z-scan techniques. The thermal diffusivity (D), specific heat (c), thermal conductivity (K), temperature variation in optical path (ds/dT) and nonlinear refractive indices (n_2) were determined. These results suggest that the studied glasses may be useful for opto-electronic devices.

Material preparation and characterization techniques

Glass preparation

Tellurium-based glasses were prepared using the melt quenching technique with the molar compositions: $(78 - x)TeO_2 + 4.5Bi_2O_3 + 5.5ZnO + 10.5Li_2O + 1.5Nb_2O_5 + xTm_2O_3$ ($x = 0.05, 0.1, 0.5, 1.0$ and 1.5 mol%). The detailed sample preparation procedure is given in Ref. [9]. The samples have surface of 15×10 mm^2 and thickness of 0.134, 0.124, 0.140, 0.121 and 0.111 cm, respectively.

Experimental

The TL technique used in this work is the dual-beam mismatched configuration reported in the literature [13–19]. A He–Ne laser at 632.8 nm was used as probe beam, and an Ar$^+$ laser at 488 nm was used as pump beam (25–100 mW). Using a profilometer (UV laser beam profiler 190–1100 nm, LBP-1, Newport), the measured excitation and probe beam waist at the sample are $\omega_e = 40.78$ μm and $\omega_p = 208.87$ μm, respectively. The pump and probe beams are detected by two silicon photodiodes connected to a Tektronix TDS2020 digital oscilloscope.

Heat capacity measurements were performed according to thermal relaxation method (TRM) [20]. A thin carbon film is deposited on the samples and is thermally isolated in a vacuum-sealed Dewar flask. One of its faces is heated with an Ar$^+$ laser at 488 nm (40 mW) through a transparent window. The temperature of the sample was recorded as a function of time via an infrared sensor placed near (~ 1 mm) the rear surface of the sample. Afterwards, the laser was blocked and a cooling curve was measured.

The third-order nonlinear optical measurements were recorded by means of a single-beam Z-scan technique [21]. A pulsed laser beam of 100 fs was generated from a mode-locked Ti–Sapphire laser (Mai Tai) at 800 nm with a repetition rate of 80 MHz. The closed-aperture Z-scan was used to measure the magnitude and sign of the nonlinear refractive index, n_2. All these measurements were performed at room temperature.

Results and discussion

Optical spectroscopy and band gap energy (E_{opt})

IR absorption spectra of the TBZLN glasses are shown in Fig. 1. It can be seen that the main absorption frequencies in the 850–450 cm^{-1} range are attributed to the stretching vibrations of the Te–O bonds. The observed bands are typically broadened and are similar to the spectra of the crystalline phases [22]. Therefore, the IR spectra provide direct proof of structural units (i.e. TeO_4, TeO_3 and TeO_{3+1}) similar to the crystal ones in the short-range order. According to Ref. [22], the addition of other oxides in tellurite glasses favours a stronger polarizability of electron doublets (ns^2) in certain directions due to the transformation of TeO_4–TeO_3 groups. In the present work, the absorption band at 740–750 cm^{-1} is attributed to the stretching mode of [TeO_3] trigonal pyramidal with non-bridging oxygen; the bands at 652 and 681 cm^{-1} are attributed to the stretching mode [TeO_4] trigonal pyramidal with bridging oxygen. The band around 550 cm^{-1} is due to the TeO_{3+1} polyhedra which consist of an intermediate coordination of TeO_3 and TeO_4 entities [23].
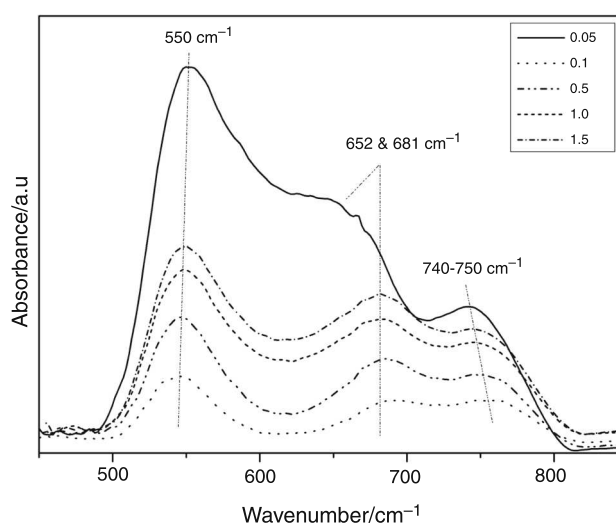
Fig. 1 IR absorption spectra of Tm^{3+}-doped TBZLN glasses
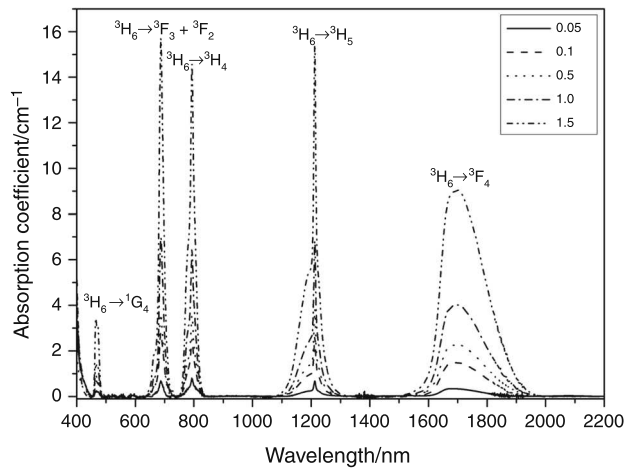
Fig. 2 Optical absorption spectra of Tm^{3+}-doped TBZLN glasses

Figure 2 shows the optical absorption spectra of Tm^{3+}-doped TBZLN glasses. The observed inhomogeneous broadened 4f–4f transitions in the wavelength range 400–2200 nm are due to Tm^{3+} ions [9, 17]. There are no bands higher than $^1G_4$ level due to the strong intrinsic bandgap absorption of the host glass. The absorption coefficients varied proportionally to the Tm^{3+} ion concentration with a maximum around 808 nm. In amorphous materials, the higher values of absorption coefficients, $\alpha(\hbar\omega) \geq 10^4$ cm^{-1}, correspond to transitions between extended states in valence and conduction bands [24]. According to Davis and Mott theory [25], the absorption coefficient in terms of optical band gap for amorphous materials can be given as:

$$\alpha(\omega) = A\frac{(\hbar\omega - E_{\mathrm{opt}})^2}{\hbar\omega}, \qquad (1)$$

where $\alpha(\omega)$ is the absorption coefficient, A is a constant, E_{opt} is the optical band gap and $\hbar\omega$ is the photon energy of the incident radiation. Figure 3 shows the plots of $(\alpha\hbar\omega)^{1/2}$
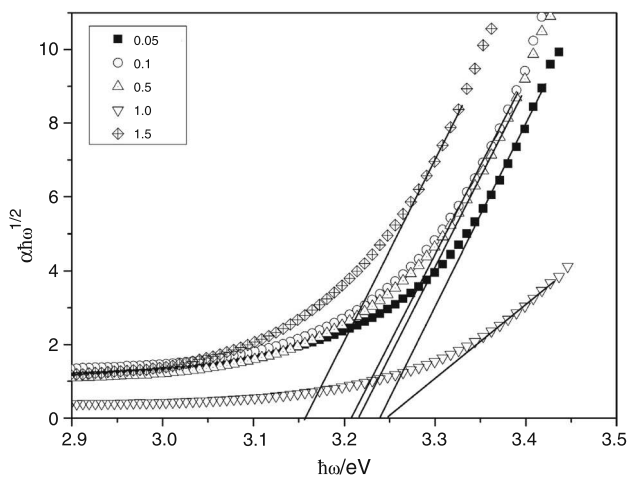
Fig. 3 Plots of $(\alpha\hbar\omega)^{1/2}$ versus $\hbar\omega$ spectra

against $\hbar\omega$ in terms of eV for the Tm^{3+}-doped TBZLN glasses.

The optical energy gap (E_{opt}) is obtained by extrapolating the linear region of the plot and is 3.23, 3.21, 3.22, 3.25 and 3.16 eV for the 0.05, 0.1, 0.5, 1.0 and 1.5 mol% of Tm^{3+}-doped TBZLN glasses. The E_{opt} values have not changed significantly with increasing concentration of Tm^{3+} up to 1.0 mol%. The drop at 1.5 mol% is attributed to the variation in non-bridging oxygens. In addition, higher concentration of dopant may cause a broadening of impurity band and the formation of band tails on the edges of the conduction and valence bands that would lead to a reduction in E_{opt} as in semiconductors [26]. The obtained gaps are comparable with the ZnO–TeO$_2$ glasses ($\sim$ 3.02–3.52 eV) [27] and higher than those reported to MoO-TeO$_2$ (2.181–2.256 eV) [28] or 50B$_2$O$_3$–xZnO–(50 − x)TeO$_2$ (2.55–2.73 eV) [29] glasses, respectively.

Measurement of thermal diffusivity (D) with TL technique

The TL technique is used to understand the modulation of the refractive index of samples caused by thermal–optical effects. In the dual-beam mismatched configuration, the probe beam propagation results in an induced phase shift of its wave front producing a lens-like effect (convergent or divergent). The intensity of the probe beam centre can be expressed with the interpretation of Fresnel diffraction theory and is written as [13, 14]:

$$I(t) = I(0)\left\{1 - \frac{\theta}{2}\tan^{-1}\left(\frac{2mV}{\left[(1+2m)^2+V^2\right]\frac{t_c}{2t}+1+2m+V^2}\right)\right\}^2. \qquad (2)$$

In Eq. (2),

$$\theta = -\frac{P_{\mathrm{abs}}}{K\lambda_p}\varphi\frac{\mathrm{d}s}{\mathrm{d}T}, \qquad (3)$$

and

$$t_c = \frac{\omega_e^2}{4D}. \qquad (4)$$

$I(0)$ or $I(t)$ is the intensity at time, $t = 0$ or t, m is the ratio of probe–pump beam area at the sample, and V is the ratio between the focal and confocal probe beam distances. In the present work, $m = 26.24$ and $V = 1.6$, respectively. The parameter θ is proportional to the probe beam phase shift induced by the thermal lens, λ_p is the probe beam wavelength, and P_{abs} is the absorbed pump power. The $P_{\mathrm{abs}} = P_{\mathrm{ex}}A_eL$, where P_{ex} is the excitation beam power, L is the sample thickness and A_e is the optical absorption coefficient of the sample. The transmittance (P) and incident (P_0) laser powers in terms of absorption coefficient

can be expressed as [30], $P = P_0(1 - R)^2 \exp(-A_e L)$, where $R = \left[\frac{(n-1)}{(n+1)}\right]^2$ is the reflectance. The estimated A_e values for the studied samples are listed in Table 1. φ is the fraction of absorbed energy converted into heat, and ds/dT is the rate of variation in the optical path with temperature. ω_e is the waist of the excitation beam at the sample, t_c is the characteristic TL response time, while D is the thermal diffusivity of the sample.

Figure 4 shows converging thermal lens signal for the 0.05 mol% of Tm^{3+}-doped TBZLN glass under the excitation of 488 nm with operating laser power of 95 mW. The solid line shows the fit of Eq. (2) resulting in a $t_c = 1.64 \pm 0.28$ ms and $\theta = -0.075 \pm 0.004$ rad. Table 1 shows thermo-optical properties of Tm^{3+}-doped TBZLN glasses. The listed thermal diffusivities were obtained from the average of several transients. There is no significant change in the thermal diffusivity (D) with increasing Tm^{3+} ions in TBZLN glasses.

Measurement of specific heat (ρc) and thermal conductivity (K)

The heat capacity of TBZLN sample (0.05 mol% of Tm^{3+}) was measured by the thermal relaxation method. This methodology records the thermal heating (thermal relaxation) of a sample over time in the presence (absence) of illumination. In the thermal equilibrium, the illuminated (front) and non-illuminated (back) faces of the samples reach saturation temperatures. Therefore, heat capacity depends on how long the sample takes to heat or cool, and is expressed by the relation [31, 32]:

$$\Delta T = T_0 - T_m = \frac{(T_m^4 - T_0^4)}{(4T_0^4)} \exp\left[1 - \exp\left(t/\tau_d\right)\right], \qquad (5)$$

where two considerations are used: i) Only radiation losses are taken into account and (ii) the temperature changes induced by the illumination are small compared to the surrounding environment temperature. In Eq. (5), T_m is the equilibrium temperature of the sample, T_0 is the initial
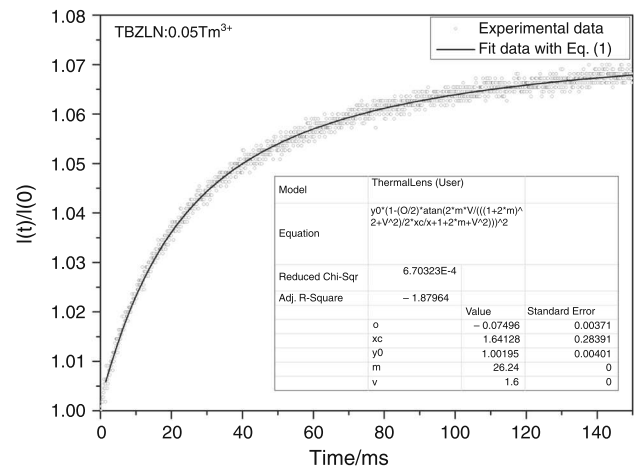
Fig. 4 Typical normalized TL signal for 0.05 mol% Tm^{3+}-doped TBZLN glass ($P_e = 95$ mW)

temperature of the sample, and the mean relaxation time is given by:

$$\tau_d = \frac{\rho c l_s}{8\sigma T_0^3}, \qquad (6)$$

where ρc is the specific heat capacity, l_s is the thickness of the sample and σ is the Stefan–Boltzmann constant. In this work, the system was calibrated measuring the heat capacity of an aluminium sample ($l_s = 400$ μm), as shown in Fig. 5a. The estimated value of the aluminium specific heat capacity is 2.40 J cm^{-3} K^{-1} that agrees with the reported literature value, 2.45 J cm^{-3} K^{-1} [33]. Similarly, the calibration measurement for the TBZLN glass (0.05 mol% Tm^{3+}) was performed with data plotted in Fig. 5b. The mean relaxation time obtained via fit of the experimental data in Eq. (4) is 170 s. Through Eq. (6), specific heat capacity (ρc) was determined as 0.83 J cm^{-3} K^{-1}, which is in good agreement with the reported tellurite glass (0.852 J cm^{-3} K^{-1}) and higher than germanate (0.445 J cm^{-3} K^{-1}), phosphate (0.549 J cm^{-3} K^{-1}) and fluoride (0.152 J cm^{-3} K^{-1}) glasses [34]. The ρc (0.83 J cm^{-3} K^{-1}) of the studied system is lower than the tellurite glasses: TeO_2–PbO–GeO_2

Table 1 Thermo-optical properties of TBZLN glasses

Tm^{3+} x/mol%	Density d/g cm^{-3}	Abs. Coeff. A_e/cm^{-1}	Optical Bandgap E_{opt}/eV	Thermal diffusivity D/cm^2 s^{-1}	Specific heat capacity ρc/J cm^{-3} K^{-1}	Thermal conductivity K/W cm^{-1} K^{-1}	ds/dT/K^{-1}
0.05	4.26	0.65	3.23	2.62×10^{-3}	0.83	2.17×10^{-3}	0.13×10^{-5}
0.1	4.21	0.72	3.21	2.64×10^{-3}	0.83	2.19×10^{-3}	0.11×10^{-5}
0.5	4.15	0.48	3.22	3.01×10^{-3}	0.83	2.50×10^{-3}	0.15×10^{-5}
1.0	3.99	0.49	3.25	2.83×10^{-3}	0.83	2.35×10^{-3}	0.22×10^{-5}
1.5	4.03	0.59	3.16	2.74×10^{-3}	0.83	2.27×10^{-3}	0.20×10^{-5}

(a)

(b)
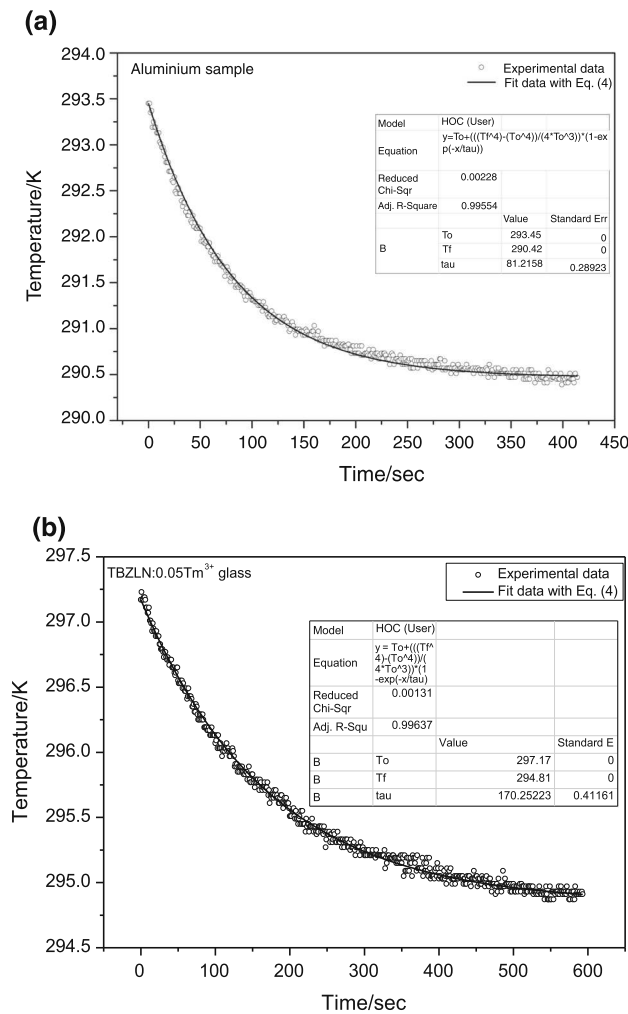
Fig. 5 Cooling curve of the specific heat capacity measurements for aluminium (reference) (**a**) and TBZLN glass (**b**) samples

(1.30 J cm^{-3} K^{-1}) (photothermal relaxation method) [19], 80TeO$_2$–15Li$_2$O–5Nb$_2$O$_5$ (1.95 J cm^{-3} K^{-1}: thermal relaxation calorimetry) [2], 87.5TeO$_2$–7.4ZnO–2.6Na$_2$O–1.5 GeO$_2$–1.0Yb$_2$O$_3$ (1.97 J cm^{-3} K^{-1}) (differential scanning calorimetry) [14], 80TeO$_2$–20 Li$_2$O (2.36 J cm^{-3} K^{-1}: thermal relaxation calorimetry) [30].

In non-crystalline solids, the thermal conductivity is independent of the composition and is several orders of magnitude smaller than in crystals. In addition, it decreases monotonically with decrease in the temperature. Heat may be transmitted in material by several independent factors. In disordered materials or glasses, the heat is transmitted entirely by phonons and it was well understood through the Debye model [35]. In the present work, using the relation, $K = \rho c D$ and known thermal diffusivity (D) of studied samples, the thermal conductivity was obtained and is listed in Table 1 for the Tm^{3+}-doped TBZLN glasses at 300 K. When comparing the TBZLN glasses with other

glasses, the former show smaller K than TeO$_2$–PbO–GeO$_2$ (2.34 × 10^{-3} W cm^{-1} K^{-1}) [19], 87.5TeO$_2$–7.4ZnO–2.6Na$_2$O–1.5GeO$_2$–1.0Yb$_2$O$_3$ (3.19 × 10^{-3} W cm^{-1} K^{-1}) [14], 80TeO$_2$–20 Li$_2$O (6.40 × 10^{-3} W cm^{-1} K^{-1}) [30], 80TeO$_2$–15Li$_2$O–5Nb$_2$O$_5$ (6.60 × 10^{-3} W cm^{-1} K^{-1}) [2], 85.0TeO$_2$–14.0ZnO–1.0Yb$_2$O$_3$ (4.69 × 10^{-3} W cm^{-1} K^{-1}) [14], 85.6TeO$_2$–6.97ZnO–4.3Na$_2$O–3.2PbO–1.0Yb$_2$O$_3$ (4.39 × 10^{-3} W cm^{-1} K^{-1}) [14].

The ds/dT was calculated through Eq. (3) and is presented also in Table 1. In Eq. (3), the fraction of absorbed energy converted into heat was taken as $\varphi = 1$. From Table 1, it can be seen that the ds/dT in TBZLN glass is positive, comparable to other host glasses [12], indicating that the created thermal lenses focalize the probe beam in far field (see Fig. 4). Its range is between 0.11–0.22 × 10^{-5} K^{-1} for the Tm^{3+}-doped TBZLN glasses. For comparison purpose, the ds/dT values of reported host glasses are presented: 85TeO$_2$ + 14ZnO + 1.0 Yb$_2$O$_3$ (0.21 × 10^{-5} K^{-1}) [14], 82.6TeO$_2$ + 16.4 BaO + 1.0 Yb$_2$O$_3$ (0.35 × 10^{-5} K^{-1}) [14], 41.5TeO$_2$ + 20.4 GeO$_2$ + 17.2 Nb$_2$O$_3$ + 19.9BaO + 1.0 Yb$_2$O$_3$ (0.59 × 10^{-5} K^{-1}) [14], soda–lime glass (0.210 × 10^{-5} K^{-1}) [36], Q-98 glass (0.131 × 10^{-5} K^{-1}) [12] and LG750 glass (0.080 × 10^{-5} K^{-1}) [37].

Measurement of nonlinear refractive index (n_2) with Z-scan technique

In Z-scan experimental setup, the sample is moved along the z-axis during the measurement of transmittance (T) of light through the sample. The transmittance is performed in two ways: (i) open-aperture Z- scan and (ii) closed-aperture Z-scan. In the case of open-aperture Z-scan, the transmitted light is collected by just passing through the sample (i.e. without aperture), whereas in the case of closed aperture, the transmitted light is collected after passing through a finite aperture ($S = 0.50$) in the far field. The third-order nonlinear properties of the samples are obtained by fitting the experimental data with the following equations [21]:

$$T = 1 - \frac{1}{\sqrt{2(x^2 + 1)}}\Delta\Psi_0, \tag{7}$$

$$T = 1 + \frac{4x}{(x^2 + 9)(x^2 + 1)}\Delta\Psi_0, \tag{8}$$

where x is the relative distance, $x = \frac{Z}{Z_0} = \frac{2Z}{k\omega_0^2}$. In the latter equation, z, z_0, k and ω_0 are the distance from the focus point, the diffraction length of the beam, the wavenumber of the light and the beam waist at the focal plane, respectively. The transmittance changes ΔT_v and ΔT_{p-v} can be obtained from the fitting curves by using the relationships: $\Delta T_v = \Delta\Psi_0$ and $\Delta T_{p-v} = 0.406(1 - S)^{0.25}|\Delta\Psi_0|$, where S

is the closed-aperture parameter and $\Delta\Psi_0$ is the nonlinear phase deformation. Then, nonlinear refractive index (n_2) and nonlinear absorption coefficient (β) are determined from the following formulas [21]

$$n_2 = \frac{\lambda\Delta_{p-v}}{0.812\pi(1-S)^{0.25}I_0L_{eff}}, \qquad (9)$$

$$\beta = \frac{2\Delta T_v}{I_0L_{eff}}, \qquad (10)$$

where λ is the wavelength and I_0 is the power density of the pump laser. L_{eff} is the effective length of the sample defined as $L_{eff} = (1 - \exp(\alpha L))/\alpha$, α is the linear absorption coefficient at a given wavelength and L is the thickness of the sample, respectively.

(a)

(b)
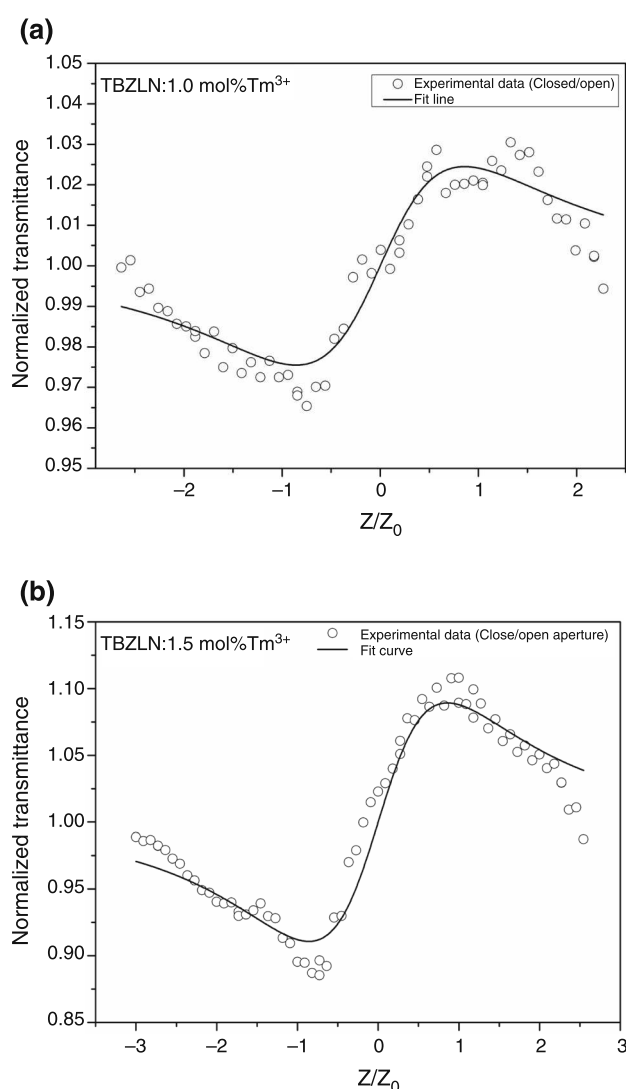
Fig. 6 Closed/open-aperture Z-scan experiment data and fitting curve for 1.0 mol% (**a**) and 1.5 mol% (**b**) of Tm^{3+}-doped TBZLN glasses. (λ = 800 nm and S = 0.50)

In the present work, both open-aperture and close aperture Z-scans were studied for the 1.0 mol% and 1.5 mol% of Tm^{3+}-doped TBZLN glasses. It is worth to notice that the transmittance at the focal plane was not observed for the open-aperture Z-scan when performed at high laser intensity (1.4 GW cm^{-2}). In the case of closed-aperture Z-scan, the observed transmittance changes between minimum (pre-focal, $Z < 0$) and maximum (post-focal, $Z > 0$) are due to the positive nonlinear refractive indexes (i.e. a self-focusing effect) [19] of the 1.0 mol% and 1.5 mol% of Tm^{3+}-doped glasses as shown in Fig. 6. The difference $\Delta Z = 1.7Z_0$ (distance between valley and peak) indicates that the samples experience electronic nonlinearities with negligible contribution from thermal effects [38]. Using Eq. (9), the nonlinear fit was performed giving $n_2 = 1.16 \times 10^{-13}$ cm^2 W^{-1} for 1.0 mol% sample and $n_2 = 3.89 \times 10^{-13}$ cm^2 W^{-1} for 1.5 mol% one. Normally, multi-component tellurite glass can exhibit increasing number of non-bridging oxygens (NBOs) which contribute to TeO$_4$ to TeO$_3$ conversion leading to higher third-order nonlinearities. Thus, the observed increase in n_2 for the 1.0 mol% to 1.5 mol% samples is a consequence of the decrease in the band gap (E_{opt}, 3.25–3.16 eV). These results suggest that 1.5 mol% of Tm^{3+}-doped TBZLN glass may exhibit significant oxide ion polarizability that leads to an increased value of $n_2 = 3.89 \times 10^{-13}$ cm^2 W^{-1}, which is higher than that of 85TeO$_2$ + 15ZnO + 1.0Nd$_2$O$_3$ (3.0 × 10^{-13} cm^2 W^{-1}) [39], Bi$_2$O$_3$ + WO$_3$ + TeO$_2$ (0.096–0.152 × 10^{-13} cm^2 W^{-1}) [24], 90TeO$_2$ + 10TiO$_2$ (0.183 × 10^{-13} cm^2 W^{-1}) [40], 70TeO$_2$ + 10Bi$_2$O$_3$ + 20ZnO (0.059 × 10^{-13} cm^2 W^{-1}) [41] glasses.

Conclusions

In conclusion, the thermal lens (TL), thermal relaxation and Z-scan techniques were applied to determine the thermal diffusivity (D), specific heat (ρc) and nonlinear refractive index in Tm^{3+}-doped TBZLN tellurite glasses. The stretching vibrations of the Te–O bonds were identified by FTIR-ATR analysis. The optical energy band gaps (E_{opt}) do not change significantly with increasing concentration of Tm^{3+} ions. From the TL measurements, ds/dT is positive. From the thermal relaxation mechanism, the medium value of the specific heat capacity (ρc) is 0.83 (J cm^{-3} K^{-1}) which is comparable with tellurite glasses reported in the literature which shows that ρc is almost independent of glass composition. The thermal diffusivity (D) and thermal conductivity (K) parameters varied between 2.62–3.01 × 10^{-3} (cm^2 s^{-1}) and 2.17–2.50 × 10^{-3} (W cm^{-1} K^{-1}) with increasing concentration of Tm^{3+} ions. Among them, the 0.5 mol% of Tm^{3+}-doped glass shows higher D (3.01 × 10^{-3} cm^2 s^{-1})

and K (2.50×10^{-3} W cm^{-1} K^{-1}), respectively. The third-order optical nonlinearity was observed in 1.0 mol% and 1.5 mol% samples by means of Z-scan technique. It is found that higher nonlinear refractive index (n_2) is consistent with the decrease in optical band gap (E_{opt}). Finally, as our samples presented low thermal conductivity, low rate of variation in optical path with temperature and high nonlinear refractive index compared with reported tellurite samples, they may be relevant for future opto-electronic applications.

References

1. Gomes L, Milanese D, Lousteau J, Boetti N, Jackson SD. Energy level decay processes in Ho3 + -doped tellurite glass relevant to the 3 μm transition. J Appl Phys. 2011;109:103110–6.
2. Moraes JCS, Nardi JA, Sidel SM, Mantovani BG, Yukimitu K, Reynoso VCS, Malmonge LF, Ghofraniha N, Ruocco G, Andrade LHC, Lima SM. Relation among optical, thermal and thermo-optical properties and niobium concentration in tellurite glasses. J Non-Cryst Solids. 2010;356:2146–50.
3. Reben M, Yousef ES, Grelowska I, Kosmal M, Szumera M. Influence of modifiers on the thermal characteristic of glasses of the TeO$_2$–P$_2$O$_5$–ZnO–PbF$_2$ system. J Therm Anal Calorim. 2016;125:1279–86.
4. Moreira LM, Anjos V, Bell MJV, Ramos CAR, Kassab LRP, Doualan DJL, Camy P, Moncorgé R. The effects of Nd$_2$O$_3$ concentration in the laser emission of TeO2–ZnO glasses. Opt Mater. 2016;58:84–8.
5. Bell MJV, Anjos V, Moreira LM, Falci RF, Kassab LRP, da Silva DS, Doualan JL, Camy P, Moncorgé R. Laser emission of a Nd-doped mixed tellurite and zinc oxide glass. J Opt Soc Am B. 2014;31(7):1590–4.
6. Mosner P, Vosejpková K, Koudelka L, Benes L. Thermal studies of ZnO–B$_2$O$_3$–P$_2$O$_5$–TeO$_2$ glasses. J Therm Anal Calorim. 2012;107:1129–35.
7. Cankaya H, Gorgulu AT, Kurt A, Speghini A, Bettinelli M, Sennaroglu A. Comparative spectroscopic investigation of Tm^{3+}: tellurite glasses for 2-μm lasing applications. Appl Sci. 2018;8:310–33.
8. Seshadri M, Barbosa LC, Radha M. Study on structural, optical and gain properties of 1.2 and 2.0 μm emission transitions in Ho^{3+} doped tellurite glasses. J Non-Cryst Solids. 2014;406:62–72.
9. Seshadri M, Anjos V, Bell MJV, Barbosa LC, Bosco GBF, Tessler LR, Suresh Kumar J, Graça MPF, Soares M, Radha M, Ratnakaram YC. Doped tellurite glasses: extending near-infrared emission for near 2.0-μm amplifiers. Inter J Appl Glass Sci. 2017;8(2):216–25.
10. Fan H, Gao G, Wang G, Hu J, Hu L. Tm3 + doped Bi2O3–GeO2–Na2O glasses for 1.8 μm fluorescence. Opt Mater. 2010;32:627–31.
11. Fan TY. Heat generation in Nd:YAG and Yb:YAG. IEEE J Quantum Electron. 1993;29:1457–9.
12. Jacinto C, Oliveira SL, Nunes LAO, Myers JD, Myers MJ, Catunda T. Normalized-lifetime thermal-lens method for the

determination of luminescence quantum efficiency and thermo-optical coefficients: application to Nd3 + -doped glasses. Phys Rev B. 2006;73:125107–9.
13. Carmo AP, Bell MJV, Anjos V, de Almeida RM, da Silva D, Kassab LRP. Thermo-optical properties of tellurite glasses doped with Eu^{3+} and Au nanoparticles. J Phys D Appl Phys. 2009;42:155404–5.
14. Kassab LRP, Kobayashi RA, Bell MJV, Carmo AP, Catunda T. Thermo-optical parameters of tellurite glasses doped with Yb^{3+}. J Phys D Appl Phys. 2007;40:4073–7.
15. Serqueira EO, Dantas NO, Silva GH, Anjos V, Bell MJV, Pereira da Silva MA. Thermal diffusivity of a SNAB glass system doped with CdS nanocrystals and Nd^{3+}. Chem Phys Lett. 2011;504:67–70.
16. Lima SM, Catunda T, Lebullenger R, Hernandes AC, Baesso ML, Bento AC, Miranda LCM. Temperature dependence of thermo-optical properties of fluoride glasses determined by thermal lens spectrometry. Phys Rev B. 1991;60(22):15173–8.
17. Moreira LM, Carvalho EA, Bell MJV, Anjos V, Sant Ana AC, Alves APP, Fragneaud B, Sena LA, Archanjo BS, Achete CA. Thermo-optical properties of silver and gold nanofluids. J Therm Anal Calorim. 2013;114:557–64.
18. Kesavulua CR, Suresh K, dos Santos JFM, Catunda T, Kim HJ, Jayasankar CK. Spectroscopic investigations of 1.06 μm emission and time resolved Z-scan studies in Nd^{3+}-doped zinc tellurite based glasses. J Lumin. 2017;192:1047–55.
19. Silva AP, Carmo AP, Anjos V, Bell MJV, Kassab LRP, de Almeida Pinto R. Temperature coefficient of optical path of tellurite glasses doped with gold nanoparticles. Opt Mater. 2011;34:239–43.
20. Anjos V, Bell MJV, de Vasconcelos EA, da Silva EF Jr, Andrade AA, Franco RWA, Castro MPP, Esquef IA, Faria RT Jr. Thermal-lens and photo-acoustic methods for the determination of SiC thermal properties. J Microelectron. 2005;36:977–80.
21. Sheik-Bahae M, Said AA, Wei TH, Hagan DJ, Van Stryland EW. Sensitive measurement of optical nonlinearities using a single beam. IEEE J Quantum Electron. 1990;26:760–9.
22. Sharaf El-Deen LM, Al Salhi MS, Elkholy MM. IR and UV spectral studies for rare earths-doped tellurite glasses. J Alloy Compd. 2008;465:333–9.
23. Ming Oo H, Mohamed-Kamari H, Mohd Daud W, Yusoff W. Optical properties of bismuth tellurite based glass. Int J Mol Sci. 2012;13:4623–31.
24. Chen Y, Nie Q, Xu T, Dai S, Wang X, Shen X. A study of nonlinear optical properties in Bi$_2$O$_3$–WO$_3$–TeO$_2$ glasses. J Non-Cryst Solids. 2008;354:3468–72.
25. Davis EA, Mott NF. Conduction in non-crystalline systems V. Conductivity, optical absorption and photoconductivity in amorphous semiconductors. Philos Mag. 1970;22:0903–22.
26. Aw SE, Tan HS, Ong CK. Optical absorption measurements of band-gap shrinkage in moderately and heavily doped silicon. J Phys Condens Matter. 1991;3:8213–23.
27. Zamyatin OA, Churbanov MF, Medvedeva JA, Gavrin SA, Zamyatina EV, Plekhovich AD. Glass-forming region and optical properties of the TeO$_2$–ZnO–NiO system. J Non-Cryst Solids. 2018;479:29–41.
28. Zamyatin OA, Churbanov MF, Plotnichenko VG, Zamyatina EV. Optical properties of the MoO$_3$–TeO$_2$ glasses doped with Ni^{2+}-ions. J Non-Cryst Solids. 2018;480:74–80.
29. Gayathri Pavani P, Sadhana K, Chandra Mouli V. Optical, physical and structural studies of boro-zinc tellurite glasses. Phys B. 2011;406:1242–7.
30. Lima SM, Falco WF, Bannwart ES, Andrade LHC, de Oliveira RC, Moraes JCS, Yukimitu K, Araujo EB, Falcao EA, Steimacher A, Astrath NGC, Bento AC, Medina AN, Baesso ML. Thermo-optical characterization of tellurite glasses by thermal

lens, thermal relaxation calorimetry and interferometric methods. J Non-Cryst Solids. 2006;352:3603–7.

31. Pinheiro AS, da Costa ZM, Bell MJV, Anjos V, Reis ST, Ray CS. Thermal characterization of glasses prepared from simulated compositions of lunar soil JSC-1A. J Non-Cryst Solids. 2013;359:56–9.

32. Pinheiro AS, da Costa ZM, Bell MJV, Anjos V, Dantas NO, Reis ST. Thermal characterization of iron phosphate glasses for nuclear waste disposal. Opt Mater. 2011;33:1975–9.

33. Valiente H, Delgado-Vasallo O, Abdelarrague R, Calderon A, Marin E. Specific heat measurements by a thermal relaxation method: influence of convection and conduction. Inter J Ther Phys. 2006;27(6):1859–72.

34. Pelle F, Gardant N, Auzel F. Effect of excited-state population density on nonradiative multiphonon relaxation rates of rare-earth ions. J Opt Soc Am B. 1998;15(2):667–79.

35. Zeller RC, Pohl RO. Thermal conductivity and specific heat of noncrystalline solids. Phys Rev B. 1977;4(6):2029–41.

36. Mansanares M, Baesso ML, Silva EC, Gandra FCG, Vargas H, Miranda LCM. Photoacoustic and ESR studies of iron-doped soda-lime glasses: thermal diffusivity. Phys Rev B. 1989;40:7912–5.

37. Campbell JH, Suratwala TI, Thorsness CB, Hayden JS, Thorne AJ, Cimino JM, Marker AJ, Takeuchi K, Smolley M, Ficini-Dorn GF. Nd-doped phosphate glasses for high-energy/high-peak-power lasers. J Non-Cryst Solids. 2000;263&264:318–41.

38. Clementi A, Chiodini N, Paleari A. Cubic optical nonlinearity in nanostructured SnO_2:SiO_2. Appl Phys Lett. 2004;84:960–2.

39. Moreira L, Falci RF, Darabian H, Anjos V, Bell MJV, Kassab LRP, Bordon CDS, Doualan JL, Camy P, Moncorge R. The effect of excitation intensity variation and silver nanoparticle co-doping on nonlinear optical properties of mixed tellurite and zinc oxide glass doped with Nd_2O_3 studied through ultrafast Z-scan spectroscopy. Opt Mater. 2018;79:397–402.

40. Chen F, Xu T, Dai S, Nie Q, Shen X, Zhang J, Wang X. Linear and non-linear characteristics of tellurite glasses within TeO_2–Bi_2O_3–TiO_2 ternary system. Opt Mater. 2010;32:868–72.

41. Yousef E, Hotzel M, Russel C. Effect of ZnO and Bi2O3 addition on linear and non-linear optical properties of tellurite glasses. J Non-Cryst Solids. 2007;353:333–8.

Study of ultrafast carrier dynamics in different doped GaAs by pump-probe differential reflectivity

H. Darabian[1], V. Anjos[1], M. J. V. Bell[1], M. Seshadri[1], Ailton J. Garcia Jr. [2,3], Leonarde N. Rodrigues[4], Christoph Deneke[2,3]

1- Grupo de Engenharia e Espectroscopia de Materiais, Departamento de Física, Universidade Federal de Juiz de Fora – UFJF. Juiz de Fora-MG, Brasil
2- Instituto de Física "Gleb Wataghin", Universidade Estadual de Campinas (Unicamp), Campinas, SP, Brasil
3- Laboratório de Ciências de Superfícies, Laboratório Nacional de Nanotecnologia (LNNano), Centro Nacional de Pesquisa em Energia e Materiais (CNPEM), Campinas-SP, Brasil
4- Departamento de Física, Universidade Federal de Viçosa (UFV), Viçosa, MG, Brasil

Abstract

We report on a study of dynamics of excited carriers in different doped GaAs bulks through a degenerate pump-probe differential reflectivity. Measurements are performed for various excitation energies and intensities. The results show that excited electrons release their energy rapidly when excited with high energy. It turns out that different electron-phonon interactions like Frohlich interaction and intervalley scattering are responsible for such a reduction. The doping level of GaAs does not change the relaxation time of electrons unless in the highly doped GaAs in which the electron relaxation times decrease. High pump intensity excites a large number of electrons in the conduction band that it decreases remarkably the electron relaxation time due to Bandgap renormalization. Furthermore, an ambipolar diffusion model is used to explore its effects on the dynamics of carriers, introducing an effective time scale around 10ps in which the diffusion effects are considerable.

Introduction

The fundamental knowledge of the nanostructured semiconductor materials has a substantial contribution to miniaturization and high performance of electronic and optoelectronic devices. Therefore, understanding light-matter interaction in the micron dimensions demands the methods that are able to study events occurring in picosecond regimes. Developing models describing the phenomena and the physics therein, in this temporal regime provides the possibility to design new nanostructured materials and control their physical properties. For example, improving the performance of THz antennas and energy harvesting devices such as solar cells in nanostructure scale are recently possible by a better understanding of dynamics the system in the temporal regime[1, 2, 3]. On the other hand, carrier doping in semiconductors that are performed in order to change electronic properties needs expensive equipment that can be replaced by carrier generation by light absorption. However, those carriers made by light absorption do not have an unlimited lifetime, in contrast to the carriers made by doping. Therefore, carrier lifetime measurement which is governed by the interactions becomes more essential. The advent of femtosecond lasers made the opportunity to investigate sub-nanosecond events in materials by using them in a pump-probe setup [4]. In this technique, the first short pulsed beam, called the pump, excites electrons from the valence band to the conduction band and the induced optical change will be measured with a delayed pulse called the probe. Pump-probe setups have been used to investigate a wide range of physical phenomena such as degenerate and non-degenerate optical pump-probe [5], optical pump- THz probe [6], heterodyne pump-probe [7] and four-wave mixing [8] and so on[9, 10]. Dynamics of generated carriers undergoing different mechanisms in short times after excitation is the main subject of this study [5]. The samples that are studied are bulks

of GaAs in order to investigate the dynamics of 3D electron gas generated by light absorption. Because the formation of confined electron systems like 2D electron gas and their emergent collective behaviors make the signal interpretations difficult [11, 12]. Particularly, in this work, we address three main questions about the dynamics of carriers in a specific case of GaAs as following: 1- What is the effect of the excitation energy on the dynamics of the carriers? 2- How the doping level can change the dynamics of the carriers? 3- If the excitation energy or in another word, the density of excited carriers is important in the dynamics of them? To this aim, a pump-probe setup in differential reflectivity mode with different conditions is implemented to answer the above questions. Moreover, the results of simulations for the carrier diffusion will be presented to understand its effects on the dynamics of carriers.

In an extended temporal and energy window, there are several processes that can evolve the distribution of electrons and holes after excitation in a semiconductor [13, 14]. To determine what mechanisms are important, we need to consider time and energy regimes of interest. In this work, we investigated the carrier dynamics behavior of GaAs bulk samples. The maximum excitation energies are 0.35eV above the bandgap at room temperature (1.42eV) and the maximum temporal window is around 50 ps by 100fs time resolution after excitation. In the mentioned energy and time regime, the main mechanisms evolving photo-excited carrier distribution are diffusion, interband transition, intervalley and intravalley interactions [15, 16, 17]. The carriers after excitation begin to thermalize between themselves and then decrease their excess energy to reach the same temperature with the lattice. The excited holes thermalize faster than electrons and reach a new equilibrium due to their heavy mass generating a hole distribution [18]. Although, the higher density of states of the conduction band compared to the valence band, due to the different curvatures of the bands, cause the dominant role of the electrons in the optical parameter changes [19]. Therefore, the effects of the holes compared to the electrons on the evolution of the system are negligible. Characteristic curvature of the conduction and valence bands provides a condition in which most of the residual energy after excitation would belong to the electrons [20]. Hereafter, we just consider the electrons as main carriers contributing to the differential reflectivity signal. Then we are able to investigate the dynamics of the electrons in a framework in which the electron-electron and electron-phonon have the principal roles in the electron dynamics. Basically, electron-phonon scatterings are attributed to interactions between the electrons and lattice. For better describing these scatterings, one needs to consider the occupied electron states, the energy and momentum of the phonons and the polarity of the lattice. Electron-phonon interactions occur with two different channels called Frohlich interaction and deformation potential. For instance, the interaction between the LO phonon in a polar semiconductor and the low energy electrons is formulated by Frohlich, demonstrating the electrons release their residual energy via zone-center LO phonon emission in the principal valley[13, 21]. In addition, deformation potential is another model that describes a mechanism in which the high energy acoustic phonons(zone-edge phonons) induce a macroscopic lattice distortion, which is formulated by a deformation potential, can interact with the electrons [22]. Piezoelectric is a well-known consequence of deformation potential in a non-centrosymmetric crystal whereby an applied electric field induces mechanical vibrations and vice versa. Moreover, the high energy electrons in the conduction bands that possess some valleys can be scattered to other valleys. This scattering called Intervalley Scattering (IVS) is an electronic transition between different valleys for electrons that provides a way to change their energy and momentum in the conduction band [11, 17]. These different valleys in conduction band often with different effective mass and density of state have an important role in transport and optical properties of semiconductors such that those electrons remain in L or X valleys have no contribution in the optical and transport properties of the samples. Redistribution of electrons in GaAs between Γ, L and X valleys occurs less than 100fs. The IVS scattering processes are possible by zone-edge optical phonons to provide those high momentum changes during the scattering [23].

The photo-generated carriers change refractive index and consequently reflectivity of materials [8] and time evolution of these changes can be seen by time-resolved photoreflectance implemented by pump-probe. Relative changes of reflectivity induced by pulsed pump and detected via probe beam given by

1)

$$\frac{\Delta R}{R}\left(\omega_{probe}, t\right) \cong \frac{4\Delta\tilde{n}\left(\omega_{probe}, t\right)}{\tilde{n}^2\left(\omega_{probe}\right) - 1}$$

Where $\tilde{n}$ is refractive index, $\Delta\tilde{n}$ is induced changes by a pump, ΔR variation of reflection coefficient, R reflection coefficient without the presence of pump, ω_{probe} frequency of probe beam and t time [4, 16].

The signal begins with an abrupt rise in reflectivity at zero delay time due to band filling. Then the peak followed by a decay showing relaxation of excited electrons. The rate of this decay basically depends on residual energy, charge density, phononic structure and form of the conduction band. In the present study, we have measured time resolved differential reflectivity at different excitation wavelengths (800nm, 750nm, 720nm and 700nm) for three GaAs bulk samples with different doping levels. The excitation wavelengths are used to determine dependency of energy excited electrons on reflectivity of GaAs. We find that the doping level from 5×10^{17} cm^{-3} to 8×10^{18} cm^{-3} has very small effect on relaxation time (RT) of excited electrons. Results show that the reduction of excitation wavelength decreases RT remarkably. Increasing the intensity of the pump, electron density leads to very fast decay and recovery of signal to a new equilibrium value. Similar works have been done to explore ultrafast dynamics of GaAs in different excited carrier densities and temperatures by other groups [19, 24]. Besides, diffusion of carriers is simulated based on ambipolar diffusion to find the role of it in ultrafast optical properties.

Experimental

Molecular beam epitaxy (MBE) was used to grow two 500 nm and one 1000 nm thick GaAs layer with n-doping (Si) of n= 5×10^{17} cm^{-3} n= 1×10^{18} cm^{-3} and n= 8×10^{18} cm^{-3}, respectively. These structures were grown on GaAs (001) substrate in the MBE of the LNNano/CNPEM (Karl Eberl MBE Komponenten) and named sample A, B and C, respectively. We have used an 80 MHz pulsed laser (Mai Tai Laser) producing 100 femtosecond pulse duration with a tunable wavelength from 690 nm to 1060nm to set up a degenerate pump-probe experiment. As shown in fig.1, the laser beam is split into a pump and probe beams. The probe intensity is around 10 times weaker than the pump and both were focused on the sample with spot size 0.03 mm^2 and 0.05 mm^2, respectively. The probe beam passes through a motorized translation stage which is controlled by computer to make delay time between the pump and probe beams. Relative polarizations between the pump and probe are orthogonal by using a half wave plate to eliminate artifact coherent effect at overlap region [25]. Time resolution is determined by pulse duration and minimum movement of the delay stage. A mechanical chopper has been used to modulate the pump and probe with different frequencies to reduce noise efficiently. Modulation of both pump and probe prevents signal interruption of the pump beam may enter to photodetector [26]. The reflected probe converted to a signal by a Si- photodetector and fed to the Lock-in and locked to sum frequencies of the pump and probe to amplify the signal. Measurements are performed at room temperature. In this configuration, we can measure the reflection variation of sample induced by the pump beam versus time. The excitation energies are selected based on the penetration depth of the beam at each wavelength and thickness of samples to avoid the beams penetrate inside the substrate. Therefore for samples A and B, 720nm and 700 nm wavelengths were used. For sample C, the used wavelengths were 700nm, 720nm, 750nm and 800nm. The photo-excited density is calculated by $\frac{(1-R)Q\alpha}{\pi d^2}$, where R is the sample reflectivity, Q is numbers of absorbed photons, α is absorption coefficient and d is the spot radii of the pump [27]. One can find α values for GaAs at each wavelength

in the literature [28]. In this work, we control the photo-excited electron density to be constant around 1×10^{18} cm^{-3} for the samples.

Carrier Ambipolar diffusion

Diffusion is a key factor in the dynamics of photo-excited carriers in semiconductors. As the effective mass of electrons and holes are different in semiconductors, we need to utilize an approach that takes into account these features and describes the diffusion behavior of the electrons and holes. A well-known model called the ambipolar diffusion model is considered that possessing the mentioned points [29]. An exact solution of the diffusion equation can be written as the following:

2)

$$N(z,t) = \frac{N_0}{2} e^{\alpha^2 Dt} \left[e^{-\alpha z} erfc \left(\frac{2\alpha Dt + z}{\sqrt{4Dt}} \right) + e^{\alpha z} erfc \left(\frac{2\alpha Dt - z}{\sqrt{4Dt}} \right) \right]$$

Where erfc is the complementary error function, N the carrier concentration, N_0 initial carrier concentration, α absorption coefficient, D the diffusion coefficient, t and z time and position in the sample along the growth direction, respectively. Since the mobility of the electrons and holes are different, we have to define an alternative value called ambipolar diffusion constant and given by

3)

$$D_{am} = \frac{D_e \mu_h + D_h \mu_e}{\mu_e + \mu_h}$$

Where D and μ are diffusivity constant and mobility of electron and hole that are represented by e and h indices, respectively. [28]. The carrier concentrations based on Equation of (2) versus penetration depth of the GaAs for 1ps and 10ps after excitation are shown in Figure 2. Four ambipolar diffusion constants are taken from 25cm^2/s to 100 cm^2/s [15, 27]. According to equation (2), one expects that carrier concentration reduces with time as seen in Figure 2, particularly at less than 200nm thickness. The simulation results show the carriers spread more inside the sample when we excite it by shorter wavelengths such that the concentration variations are more considerable for 700nm from 1ps to 10ps compared to 800nm.

The diffusion effect is more evident when we use a degenerate pump-probe setup. On one hand, the above results show that the spatial carrier concentration is highly dependent on the pump wavelength. On the other hand, the maximum thickness that could be covered by the probe is wavelength dependent due to the dependence of the absorption coefficient of GaAs on wavelength. Furthermore, we use a pump-probe setup in reflection mode the care should be taken that the penetration depth of the probe becomes half of the pump. For instance, the pump penetration depths for 700nm and 800nm are around 500nm and 800nm, respectively. Thus, in a similar initial carrier concentration for both wavelengths, the carriers that are created by 700 nm are more localized near the surface in the GaAs. Moreover, the 700nm probe can just detect $\frac{500nm}{2} = 250nm$ beneath the surface where the concentration variations are more intense. Whereas the maximum penetration for 800nm probe is around 400 nm, where the changes are smooth. Therefore, in a pump-probe setup, changes in a probe intensity should be more pronounced in shorter wavelengths due to the dynamics that is induced by the diffusion. The carrier distribution with higher Diffusion constant and long times after excitation have slower slopes and consequently are more stable. Also, as shown in Figure 2, the carrier distribution with higher diffusion constant and long times after excitation have slower slopes and consequently are more uniform. It implies that the diffusion effects are less considerable after 10 ps in the ultrafast dynamics of the carriers, at least in the mentioned wavelengths.

Result and discussion

All measurements show a transient peak in the signals after excitation in zero time delay. This abrupt change is due to band filling leading to saturation in absorption. These peaks are followed by a decay that is varied by experimental conditions. The decay behavior can be formulated by a bi-exponential function, in a general form such that $\frac{\Delta R}{R} = a_1 + a_2 \exp\left(-\frac{t}{\tau_1}\right) + a_3 \exp\left(-\frac{t}{\tau_2}\right)$, where τ_1 and τ_2 are time parameters that are assigned to the momentum and energy relaxation process of electrons, a_1, a_2 and a_3 are constants coefficients, respectively[18]. Momentum RT usually is smaller than energy relaxation and normally less than 100fs. Therefore, it is not available to resolve such a fast process because the temporal resolution of our setup is more than 100fs. As a result, fitting always give the same values for τ_1 and τ_2 showing that only energy relaxation is observable in our setup. It is worth mentioning that relaxation momentum time refers to a difference between absorption and emission of phonons by electrons, whereas the energy RT is the sum of absorption and emission of phonons. Since momentum and energy relaxation times are different.

Figure 3 shows differential reflectivity and calculated RT for sample C, at four different wavelengths. The RTs at 800 nm and 750nm probe are around 12ps - 11ps, respectively, where these values for 720 nm and 700 nm probe decreases substantially and reach around 4ps. Results for samples A and B show similar the RT values at 720nm and 700nm. This tendency indicates that the electron RTs highly depend on the excitation energy, especially for the high doped GaAs sample. This behavior can be understood from the point of view of the carrier-phonon interactions. Frohlich interaction (electron-phonon interactions) is responsible for the reduction of electron RT in GaAs. As explained earlier, the excited electrons with residual energy in the conduction band can release their energy by LO phonon emission. As the energy of the excited electron rise up in the conduction band the probability of the interaction increase and consequently the electron relax rapidly [30]. The interaction may happen through the absorption and emission of phonons by electrons. Frohlich theory proves that LO phonon emission dominates LO phonon absorption in the energy regimes higher than bandgap energy [13]. In addition, the small bandgap between the acoustic and optical phonon bands in GaAs causes rapid decay of LO phonon to either a TO phonon and an acoustic phonon or two acoustic phonons with different momentums. The mentioned decay mechanisms reduce the LO phonon occupancy number and therefore decrease the contribution of LO phonon absorption in electron-phonon interaction. In materials with the large bandgap phonon bands, the presence of LO phonon in more time leads to a considerable LO phonon absorption and an increase of energy of electrons. This phenomenon is called the bottleneck effect [31]. Nevertheless, the reduction RTs for 720nm and 700nm are more remarkable. Since the Frohlich interaction approaches to a saturation value by increasing more the electron energy, one needs another mechanism to explain such reduction. We suggest an intervalley scattering in which an electron with sufficient energy is transferred from Γ valley to L or X valley and vice versa. In fact, during a backscattering from a side-valley (L or X) into the Γ valley, which is possible by phonon emission due to the momentum conservation, it reduces the energy of an electron. The transition probability of IVS is calculated based on Fermi's golden and given by:

4)

$$P_{X,L\to\Gamma} = \frac{2\pi}{\hbar}\sum_{i,f}|\langle f|H_{Fro}|i\rangle|^2$$

Where initial state (i) is the electron states in the L or X valley, (f) is the final electron state in the Γ valley and H_{Fro} is the Hamiltonian of IVS that is proportional to the Frohlich interaction value discussed earlier [20, 32]. Of course, it should be noted that deformation potential interaction could be involved in IVS although its contribution is weak, particularly in polar semiconductors compared to Frohlich interaction

[31]. A schematic of possible mechanisms after excitation is presented in Figure 4. The IVS is forbidden energetically for excitations with 800nm and 750nm. It is turned out that after a threshold energy IVS is allowed and consequently leads to a fast decay for the excited electrons. The tendency of the RTs by the energy show a good agreement with Monte-Carlo simulation results and experimental data from time-resolved photoluminescence setup, Raman spectroscopy and photoemission microscopy [31, 33-35]. IVS is important not only for the decay process but also for the time initial peak in the signal. An increase in the time that the peak occurs are observed in 720nm excitation. We purpose that in 720nm excitation where the energy is enough to scatter electrons to L valley, the band filling time can be elongated because the side-valley electrons can stay more time in their states and repopulate the initial states were populated just after the excitation. Although it is not observed in 700nm excitation due to the interband transition from the split-off band. When the energy is enough to excite electrons from all possible valence bands, the contribution of excited electrons from the light hole, heavy hole and split-off are around 0.4, 0.4 and 0.2, respectively. Therefore, the electrons that are excited from the split-off band do not contribute to IVS because they are placed at the bottom of the conduction band and decrease the effect of IVS on the time of the signal peak [19]. Also, in the simulation section, we found that for shorter wavelengths, the carriers need more time to approach a stable distribution and a time regime around 10ps is introduced from the results, showing good agreement with the signals of 720nm. Nevertheless, the kinetic energy of diffusion is so less than the energy regime of the excited electrons that suppresses the effect of the split-off electrons in the case of 700nm.

Results are presented in Figure 5 demonstrate the very low dependency of the RT on the doping level for electrons excited by 720nm and 700nm probe. This may be indicative of the large energy difference between the Fermi level and the excited electrons despite the increase of Fermi level by doping. However, small reductions in RTs are observed by rising doping levels. It may be due to the bandgap renormalization of the high doped GaAs. The Bandgap renormalization lowers the Bandgap energy even though small, however, it causes the excited electron with more energy in the conduction band and as we explained previously, more energy of the electron, faster decay of them[16].

Figure.6 represents the effects of the intensity on the differential reflectivity of sample B, excited by 720nm and 700 nm. More intensity increasing was not possible because of the limits of the laser at 700nm. Two main effects are observed in this experiment. First, results show a substantial reduction in the RT with increasing the excitation intensity and consequently the excited electron density. Second, the recovery of the signals to the initial value at zero delay time is more pronounced as the intensities increase. We conclude that electron RT is dependent on the density of excited electrons. In fact, the higher excited electron number provides more phonon occupation number due to the LO phonon emission and therefore it increases the interaction electron-phonon and reduces the electron RT more effectively. Those electrons have released their energy and reach a Fermi level cause a bandgap renormalization happens and becomes amplified by a higher number of electrons. As explained earlier, the bandgap renormalization decreases the bandgap and eventually electron RT. This avalanche-like process recovers the signal rapidly to the probe intensity value without the pump.

Conclusion:

In summary, the ultrafast dynamics of carriers in the doped bulks of GaAs have been studied by a degenerate pump-probe at different wavelengths. We find that the residual energy of the excited electrons in the conduction band is a crucial role in the evolution of them such that the energetic electrons relax rapidly.

This behavior is explained by electron-phonon interactions such as Frohlich interaction and IVS. Also, a threshold wavelength around 720nm is observed in the measurements allowing IVS to occur in the samples. Our data are in good agreement with experimental results and simulations in literature. Also, the results show that the doping levels of GaAs have a very small effect on the RT of electrons such that high doping level decreases the RT of excited electrons. We attribute this effect to a bandgap renormalization in the high doped GaAs. Moreover, the ambipolar diffusion simulation reveals a time scale around 10ps in which the spatial distribution of carriers becomes stable. Furthermore, a fast signal recovery is observed for the sample pumped with high intensity. This is as a result of an effective bandgap renormalization with higher electron density. On the other hand, the high number of emitted phonons from the decay of the large density of the excited electrons provides a faster decay for the electrons.

References:

1- McIntosh, K. A., et al. "Investigation of ultrashort photocarrier relaxation times in low-temperature-grown GaAs." Applied physics letters 70.3 (1997): 354-356.
2- Busch, Stefan, et al. "Terahertz transceiver concept." Optics express 22.14 (2014): 16841-16846.
3- Yano, R., Hirayama, Y., Miyashita, S., Sasabu, H., Uesugi, N., & Uehara, S. (2001). Pump–probe spectroscopy of low-temperature grown GaAs for carrier lifetime estimation: arsenic pressure dependence of carrier lifetime during MBE crystal growth. Physics Letters A, 289(1-2), 93-98.
4- Prasankumar, Rohit P., and Antoinette J. Taylor, eds. Optical techniques for solid-state materials characterization. CRC Press, 2016.
5- Yahng, J. S., et al. "Femtosecond degenerate and nondegenerate pump-probe experiments in bulk GaAs below the band gap." Journal of the Optical Society of Korea 1.2 (1997): 100-103.
6- George, Paul A., et al. "Ultrafast optical-pump terahertz-probe spectroscopy of the carrier relaxation and recombination dynamics in epitaxial graphene." Nano letters 8.12 (2008): 4248-4251.
7- K. L. Hall, G. Lenz, E. P. Ippen, and G. Raybon, "Heterodyne pump–probe technique for time-domain studies of optical nonlinearities in waveguides," Opt. Lett. 17, 874-876 (1992)
8- P. Borri, W. Langbein, J. Mørk, J.M. Hvam, Heterodyne pump-probe and four-wave mixing in semiconductor optical amplifiers using balanced lock-in detection, Optics Communications, Vol. 169, 1–6,1999,317-324.
9- Bartels, Albrecht, et al. "Femtosecond time-resolved optical pump-probe spectroscopy at kilohertz-scan-rates over nanosecond-time-delays without mechanical delay line." Applied physics letters 88.4 (2006): 041117.
10- Man, Michael KL, et al. "Imaging the motion of electrons across semiconductor heterojunctions." Nature nanotechnology 12.1 (2017): 36.
11- Rodrigues, Leonarde N., et al. "Resonant electronic Raman scattering: A BCS-like system." Physical Review B 93.20 (2016): 205409.
12- Anjos, V., and L. Ioriatti. "Collective and single-particle excitations in Raman scattering of multilayer δ-doped systems." Physical Review B 63.3 (2000): 035404.
13- Shah, Jagdeep. Ultrafast spectroscopy of semiconductors and semiconductor nanostructures. Vol. 115. Springer Science & Business Media, 2013.
14- Ziaja, Beata, et al. "Time-resolved observation of band-gap shrinking and electron-lattice thermalization within X-ray excited gallium arsenide." Scientific reports 5 (2015): 18068.
15- Williams, G. Jackson, et al. "Direct measurements of multi-photon induced nonlinear lattice dynamics in semiconductors via time-resolved x-ray scattering." Scientific reports 6 (2016): 39506.

16- Prabhu, S. S., & Vengurlekar, A. S. (2004). Dynamics of the pump-probe reflectivity spectra in GaAs and GaN. Journal of applied physics, 95(12), 7803-7812.

17- Wells, Nathan P., et al. "Transient reflectivity as a probe of ultrafast carrier dynamics in semiconductors: A revised model for low-temperature grown GaAs." Journal of Applied Physics116.7 (2014): 073506.

18- Tommasi, R., P. Langot, and F. Vallée. "Femtosecond hole thermalization in bulk GaAs." Applied physics letters 66.11 (1995): 1361-1363.

19- Lin, W-Z., et al. "Femtosecond absorption saturation studies of hot carriers in GaAs and AlGaAs." IEEE journal of quantum electronics 24.2 (1988): 267-275.

20- Knox, W. H., et al. "Femtosecond excitation of nonthermal carrier populations in GaAs quantum wells." Physical review letters 56.11 (1986): 1191.

21- Sjakste, J., et al. "Hot electron relaxation dynamics in semiconductors: assessing the strength of the electron–phonon coupling from the theoretical and experimental viewpoints." Journal of Physics: Condensed Matter 30.35 (2018): 353001.

22- Zollner, Stefan, Sudha Gopalan, and Manuel Cardona. "Microscopic theory of intervalley scattering in GaAs: k dependence of deformation potentials and scattering rates." Journal of Applied Physics 68.4 (1990): 1682-1693.[canceled]

23- Kanasaki, Jun'ichi, Hiroshi Tanimura, and Katsumi Tanimura. "Imaging energy-, momentum-, and time-resolved distributions of photoinjected hot electrons in GaAs." Physical review letters 113.23 (2014): 237401.

24- Nie, X. C., et al. "Transient transition from free carrier metallic state to exciton insulating state in GaAs by ultrafast photoexcitation." New Journal of Physics 20.3 (2018): 033015.

25- Lebedev, M. V., et al. "On the nature of "coherent artifact"." Journal of Experimental and Theoretical Physics 100.2 (2005): 272-282.

26- Mondal, Richarj, et al. "How pump–probe differential reflectivity at negative delay yields the perturbed-free-induction-decay: theory of the experiment and its verification." Journal of Physics: Condensed Matter 30.50 (2018): 505902.

27- Basak, Amlan Kumar, et al. "Ultrafast coupling of coherent phonons with a nonequilibrium electron-hole plasma in GaAs." Physical Review B 91.12 (2015): 125201.

28- Jellison Jr, G. E. "Optical functions of GaAs, GaP, and Ge determined by two-channel polarization modulation ellipsometry." Optical Materials 1.3 (1992): 151-160.

29- Mics, Zoltán, et al. "Density-dependent electron scattering in photoexcited GaAs in strongly diffusive regime." Applied Physics Letters 102.23 (2013): 231120.

30- Sjakste, Jelena, et al. "Energy relaxation mechanism of hot-electron ensembles in GaAs: Theoretical and experimental study of its temperature dependence." Physical Review B 97.6 (2018): 064302.

31- Clady, Raphael, et al. "Interplay between the hot phonon effect and intervalley scattering on the cooling rate of hot carriers in GaAs and InP." Progress in Photovoltaics: Research and Applications 20.1 (2012): 82-92.

32- Stanton, C. J., and D. W. Bailey. "Rate equations for the study of femtosecond intervalley scattering in compound semiconductors." Physical Review B 45.15 (1992): 8369.

33- Bernardi, Marco, et al. "Ab initio study of hot electrons in GaAs." Proceedings of the National Academy of Sciences 112.17 (2015): 5291-5296.

34- Kim, Dai-sik, and Y. Yu Peter. "Hot-electron relaxations and hot phonons in GaAs studied by subpicosecond Raman scattering." Physical Review B 43.5 (1991): 4158.

35- Tanimura, Hiroshi, et al. "Formation of hot-electron ensembles quasiequilibrated in momentum space by ultrafast momentum scattering of highly excited hot electrons photoinjected into the Γ valley of GaAs." Physical Review B 93.16 (2016): 161203.

Table 1:RT for samples at two different wavelengths.

	A	B	C
720nm	4.7 ps	4.5 ps	4ps
700nm	4.7 ps	4.5 ps	3.5ps
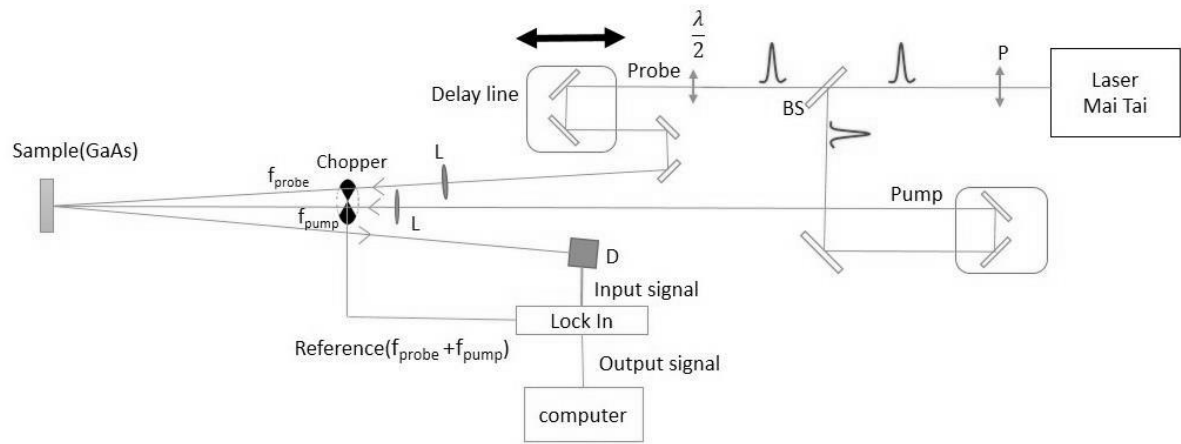
Figure 1: Schematic of pump-probe differential photoreflectance. BS: beam splitter, M: mirror, D: detector, L: lens and λ/2 is a half wave plate.
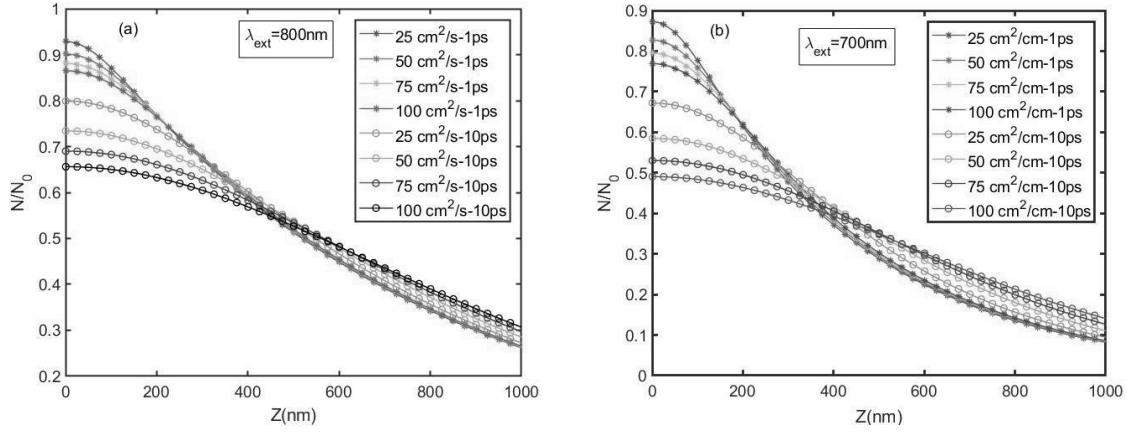
Figure 2: Carrier concentration profile in GaAs for excitation wavelength a) 800nm and b) 700nm. Circle and star points show data for 1ps and 10 ps after excitation, respectively. The simulations were performed for different values of ambipolar diffusion coefficient and Z is the distance between the surface and a point inside the sample along the growth direction.
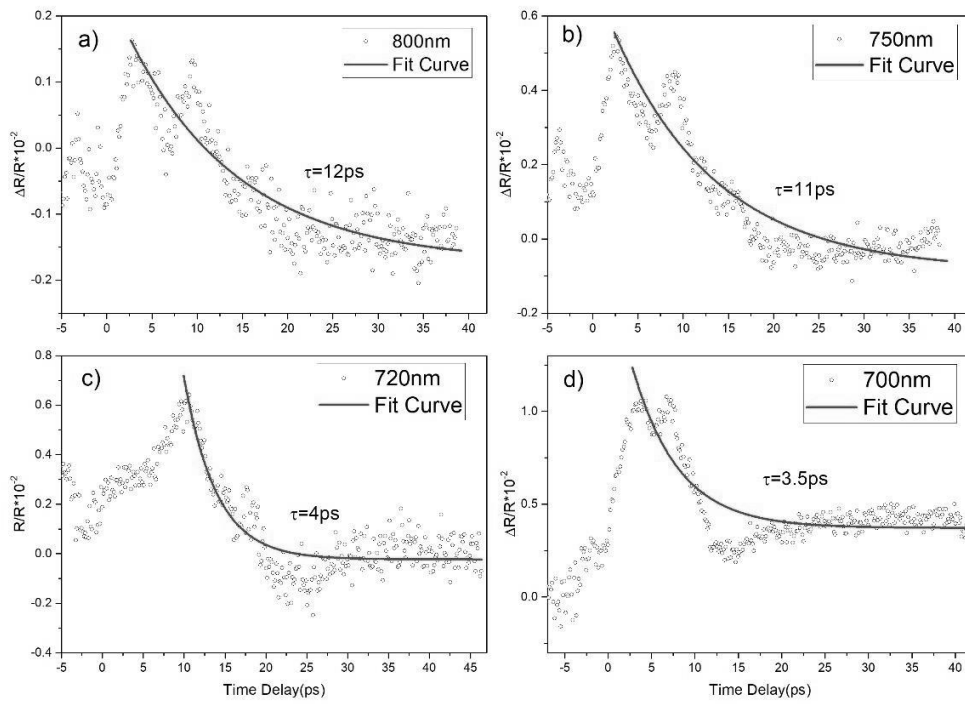
Figure 3: Time-resolved differential reflectivity of sample C at a) 800nm, b) 750nm, c) 720nm and d) 700nm and red lines are fit curves. The RTs are represented in each graph.
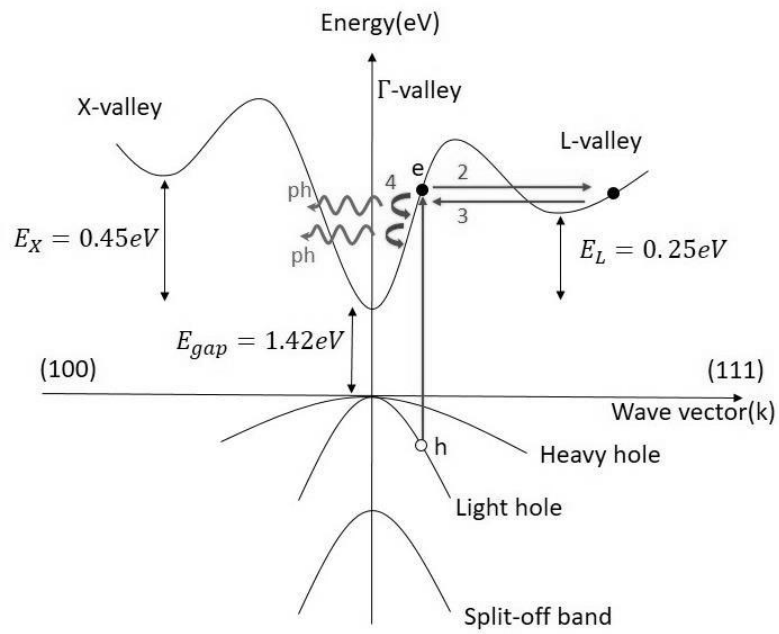
Figure 4: Schematic of energy band of GaAs and ultrafast processes after excitation indicated by arrows. 1-excitation of electrons by photon absorption .2- scatter out to satellite valleys. 3- scatter back to Γ valley again. 4- Cool down to the lower energy states by emitting phonons.
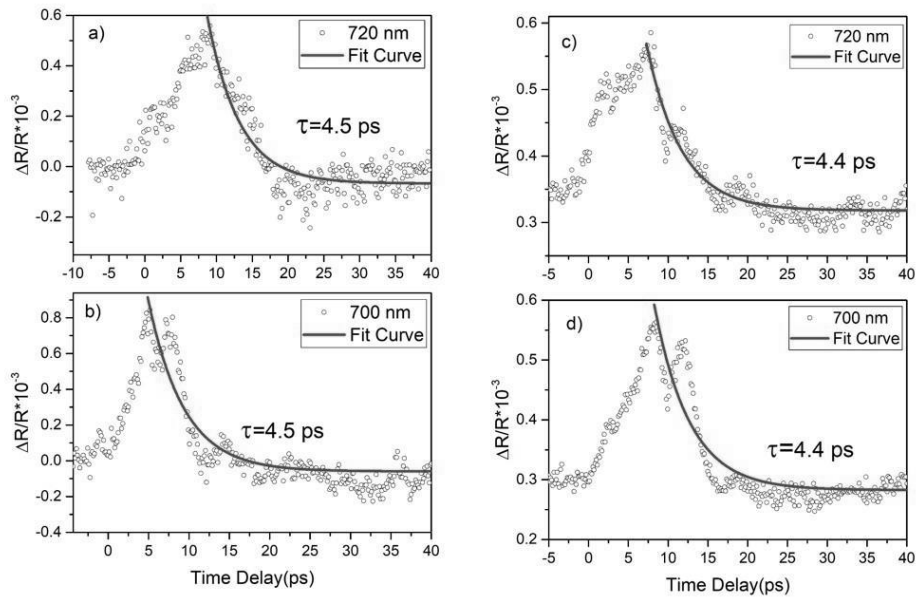
Figure 5: Differential reflectivity for (a) and (b) sample A and (c) and (d) for sample B at two excitation energy versus delay time.
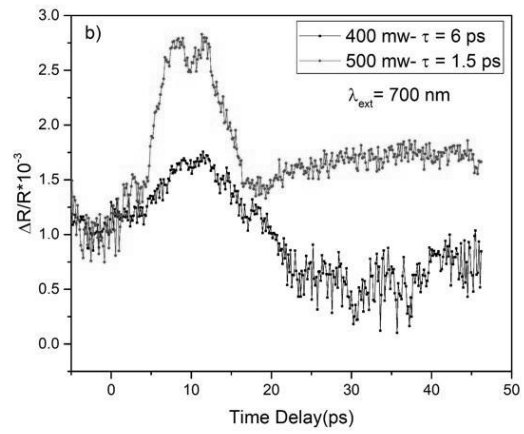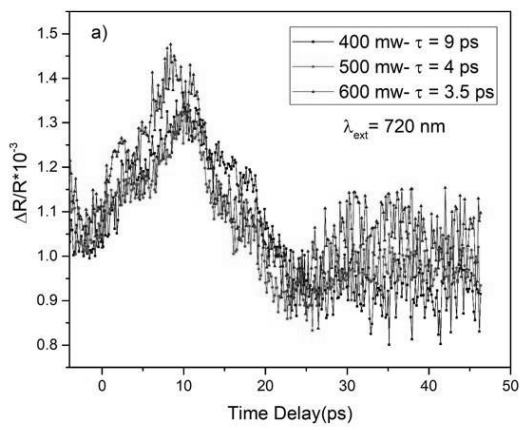
Figure 6: The differential reflectivity for the sample B excited by a) 720nm and b) 700nm in three and two different intensities ,respectively. The arrows indicate the growth direction in the signal.

Structural and thermal study of ZnTe Nanocrystals doped with Cr and Mn in phosphate glasses

H. Darabian[1], M. Radha[1], V. Anjos[1], M. J. V. Bell[1], C. Batesttin[1], A. S. Silva[2], N. O. Dantas[2]

[1]Grupo de Engenharia e Espectroscopia de Materiais, Departamento de Física, Universidade Federal de Juiz de Fora - MG 36036-900, Brazil

[2]Laboratório de Novos Materiais Nanoestruturados e Funcionais, Instituto de Física, Universidade Federal de Alagoas, Brazil

Abstract:

In this study, structural and thermal features of phosphate glasses doped with diluted magnetic semiconductors are investigated. The samples were ZnTe nanocrystals doped with different concentrations of Cr and Mn. UV-visible absorption spectra showed the presence of Cr^{2+} and Cr^{3+} ions into the matrix. Depolymerization of the phosphate network is observed by Raman spectroscopy due to the addition of Cr ions breaking the phosphate chains. The thermal diffusivity (D), thermal conductivity (K), specific heat capacity (ρc) and optical path variation with temperature (dS/dT) of samples are measured by thermal lens and ρc techniques. The thermal conductivity values show that although the formation of crystalline structures of ZnTe inside the matrix glasses leads to a decrease, the incorporation of the Cr and Mn do not show a definite trend. A monotonic reduction in optical path variation with temperature is observed with nanocrystal formation and Cr addition.

Key words: Diluted magnetic semiconductor, Thermal conductivity, Depolymerization, Phosphate glass

Introduction:

The demand for new materials aiming the fabrication of different devices that enable the control of the spin freedom degree has been attracting attention for decades. Diluted magnetic semiconductors (DMS) form one of these groups where materials for spintronic applications demonstrated ferromagnetism in high temperature (T_c>100K) [1]. This feature distinguishes DMS from other magnetic semiconductors which may require low temperatures to show distinct magnetic phenomena [2]. A possible class of DMS comprises wide band gap semiconductors doped with transition metal (TM) ions as Cr, Mn and Ni. The electrons of the TM ions in *d* orbitals interact with the semiconductor carriers in the *sp* orbitals leading to appearance of ferromagnetism even in room temperature [3, 4]. DMS nanostructures can improve optical properties. For example, possible energy transfer between semiconductor nanostructures and TM ions through which luminescence enhancement may occur is an interesting advantage of the materials [5]. In addition, doping with two different TM ions has been presented as a straightforward method to add further properties either by the formation of new electronic transitions, or by modulating intrinsic defect points in the crystalline structure of the semiconductor [6].

Thermo-optical response of such optical materials, where excitation by a laser beam may generates a local increase in temperature that change refractive index, is another parameter that should be considered for emission applications like in high power lasers. In this case, it is important to know how the generated heat dissipates to avoid degradation of the optimal conditions that affect the lasing active medium. This effect is observed and measured by a technique called thermal lens spectroscopy where thermal elastic properties are extracted such as thermal conductivity. In solids, thermal conductivity (K) has two main components are the lattice (κ_L) and electronic (κ_e) parts. The lattice contribution is dominant compared to the electronic counterpart in glasses due to low free carrier density. This can be modified by changing the structure and composition of the material [7, 8].

Furthermore, investigation on thermal properties of magnetic materials is interesting due to the possibility of generating spin current by applying a temperature gradient over length of a magnetic material, an effect

called spin Seebeck effect [9, 10]. Therefore, the knowledge of the thermal properties of magnetic materials like thermal conductivity is essential for design of spintronic devices exploiting spin Seebeck effect.

There are some techniques to make DMSs such as epitaxy methods [11, 12], colloidal [13] and mechanical method [14]. However, an affordable and promising method is proposed based on growing crystalline structures of DMS inside glasses by the fusion and annealing methods [15, 16]. The glassy structure of a host determines electrical, optical and thermal features allowing us to design tailored materials by doping with other components or elements. Phosphate glasses are promising host media to modify the optical properties due to a high transparency from UV to near IR and low phonon energy [17, 18]. The latter reduces the probability of non-radiative emission after excitation and the former enables one to dope the matrix with transition metals or rare earth elements. The enhancement of optical emission by adding DMS was already observed due to new possible energy transitions between the metal ions and nanocrystals (NCs) [19].

In this work, phosphate glass with a nominal composition of $65P_2O_5.14ZnO.1Al_2O_3.10BaO.10PbO$, PZABP, is considered as a host material [20]. The ZnTe (semiconductor) nanocrystals are grown in the PZABP matrix with Cr and Mn co-doping. Effects of the presence of DMS NCs with different concentration of the mentioned magnetic elements on electronic structure, thermal conductivity, thermal diffusivity, specific heat capacity and structural properties of the samples will be studied. The purpose of this article is to investigate the relation between structural and thermal properties in the samples. Moreover, the insertion of the transitions metals in our glass may confer to them magneto-optics features. Concerning the latter aspect, nonlinear optical properties should be addressed. In fact, we tried to measure optical nonlinear properties via Z-scan technique. Nevertheless, the heating of the samples was the technical obstacle which avoids the measurement.

Experimental details

The PZABP glasses were prepared with different concentrations of Mn and Cr in $Zn_{1-x-y}Mn_yCr_xTe$ structures. Four samples were prepared, with y=0.01 and x= 0.005, 0.01, 0.05, 0.1 (or equivalently, x= 0.5, 1, 5, 10% weight). Thereafter the samples will be named only by the weight percentage of Cr content. As a reference, two additional samples were prepared, one PZABP doped with 0.05Cr and the other, embedded only with ZnTe NCs. The detailed process of fabricating is presented elsewhere [16, 21, 22].

UV-Vis-NIR absorption spectrum is measured by a model UV-2550 Shimadzu spectrometer from 200 to 900 nm for the all samples with resolution of 0.1 nm. The micro Raman spectra are measured using a 488 nm wavelength laser for excitation and detected with an integrated triple spectrometer T64000 at room temperature. The spectrometer covers Raman shifts from 200 to 1400 cm^{-1} with resolution of 0.7 cm^{-1}. Raman spectra are recorded in two different polarizations situations: a) HH in which polarization of the incident and scattered light have parallel polarization; b) nonpolarized. A thermal lens setup is used with a 488 nm wavelength laser for excitation and a 632.8 nm wavelength laser as a probe beam in a mismatched configuration to determine thermal diffusivity [23, 24]. The thermal diffusivity (*D*) was measured by the thermal lens technique in order to investigate the effects of Mn and different concentration of Cr ions. A scheme of the thermal lens technique is presented in Fig. 1. The Thermal Lens theory considers two-dimensional radial temperature rise and heat flow in the sample, produced by a pump beam with Gaussian profile [25]. Consequently, a refractive index gradient is produced, which generates the lens effect, monitored by a probe laser.

According to the diffraction integral model, the temporal evolution of the probe intensity, *I(t)*, in the thermal lens technique is given by [26],

$$I(t) = I(0)\left[1 - \frac{\theta}{2}\tan^{-1}\left(\frac{2mV}{\frac{[(1+2m)^2+V^2]t_c}{2t} + 1 + 2m + V^2}\right)\right]^2 \quad (1)$$

where

$$m = \left(\frac{\omega_p}{\omega_e}\right)^2, \quad V = \frac{Z_1}{Z_c} \quad \text{with } Z_c \ll Z_2,$$

t_c is obtained from the equation $D = \frac{\omega_0^2}{4t_c}$ where D is the thermal diffusivity of the sample. ω_0 is the beam waist of the pump beam. Z_c is the confocal distance of the probe beam, Z_1 is the distance between the probe beam and the sample, Z_2 corresponds to the distance between the sample and the detector, ω_p (ω_e) accounts for the probe (pump beam) beam radius at the sample, and $I(0) = I(t)$ when the transient time t is zero. V and m are geometrical parameters of the experiment and have the fixed values 1.6 and 26.24, respectively. The relation between the phase shift of probe beam (θ) and the variation of optical path beam by temperature (dS/dT) is given by,

$$\theta = -\frac{P_e A l_0}{K \lambda_p} \varphi \frac{ds}{dT} \qquad (2)$$

Where P_e is excitation beam power, A is absorption coefficient, l_0 is the sample thickness, λ_p is the probe wavelength and φ is the fraction of the optical energy converted to heat energy [27]. In order to determine thermal conductivity of the samples, the thermal relaxation method was used. The relation between thermal conductivity (K) and thermal diffusivity (D) is $K = \rho c D$, where ρ and c are the density and specific heat, respectively. Combining thermal diffusivity from the thermal lens setup and ρc quantity that is measured by the thermal relaxation technique, thermal conductivity constant is obtained. The thermal relaxation technique is based on heating a sample with a laser up to a certain temperature and recording temperature changes in cooling process after blocking the laser to measure specific heat capacity. In our case, the sample is placed in a vacuum chamber and diode laser with 445 nm wavelength and 32 mw is used for heat generation. More details about the technique can be found in the reference [28]. The temperature of the sample is measured versus time by a thermocouple. Via the temperature dynamic of a sample after the absorption of an optical pulse the ρc may be obtained. This can be obtained based on solving the energy balance equation with heat losses due to radiation and given by [28],

$$\Delta T(t) = T_f - T_0 = \left(\frac{T_f^4 - T_0^4}{4T_0^3}\right)[1 - \exp\left(\frac{t}{\tau_r}\right)], \quad (3)$$

where T_f is the sample temperature after blocking the beam light in a cooling process, T_0 is the initial temperature of the sample after absorption of light, and τ_r is temporal decay parameter which is related to density and heat capacity of sample by the relation, $\tau_r = \frac{\rho c l_0}{8\sigma T_0^3}$ in which σ is Stefan- Boltzmann constant. All experiments were performed at room temperature.

Results

Fig. 2 exhibits the UV-Vis absorption of the samples that is clearly modified by adding ZnTe, Mn and Cr ions. The black curve, for undoped PZABP indicates that the glass has UV absorption and no structures from 300 to 800 nm. The blue curve, PZABP doped with Cr, allows the identification of Cr ions absorption. Previously, it was reported that Cr ions could be found in the Cr^{2+} and Cr^{3+} valences in PZABP glasses doped with $Zn_{1-x-y}Mn_yCr_xTe$ NCs. The spin-forbidden transitions of Cr^{2+} ions with tetrahedral coordination, $^5T_2(^5D) \rightarrow ^1A_2(^1I)$, $^5T_2(^5D) \rightarrow ^3A_2(^3F)$, $^5T_2(^5D) \rightarrow ^3E(^3H)$, and $^5T_2(^5D) \rightarrow ^3T_2(^3H)$ were associated with the absorption bands at 457, 633, 659 and 689 nm, respectively, and were also identified in the present samples [29]. On the other hand, the band around 300 nm is observed only in the PZABP:5Cr sample and it is attributed to the $^4A_2(^4F) \rightarrow ^4T_2(^4P)$ transition of Cr^{3+} ions with octahedral coordination. A detailed analysis of the absorption spectrum based on the transition energies of the ions by using the Tanabe-Sugano diagram can be seen elsewhere [19]. Besides, two bands at 400 nm and 532 nm (red curve, red arrows in the online version) are assigned to the formation of quantum dots (QD) and bulk nanocrystals of ZnTe, respectively. The addition of Cr and Mn ions decreases the formation of QDs which can be seen in the intensity of the related bands. However, although the absorption spectra confirm the formation of ZnTe NCs and the incorporation of the Cr and Mn ions in the NCs, a measurement by the magnetic phase images is necessary in order to check whether the incorporation of the Cr and Mn ions gives rise to the DMS structure [16].

Raman spectra with different polarization states were also performed to survey structural information of the samples and the effects of doping materials. The HH and unpolarized Raman spectra of the samples

are presented in Fig.3 a and b, respectively. The main components of phosphate glasses are different structures of PO_4 tetrahedral depending on the number of bridging oxygens (n), named as Q^n [30- 32]. The bands around 745 cm^{-1} and 690 cm^{-1} are related to the bridging oxygens in Q^2 and Q^1, respectively. The detailed information about the identified Raman bands is listed in Table 1. Even though some bands are relatively similar in Fig. 3a and b, their relative intensities depend on the polarization. In the HH spectrum certain bands e. g. around 700 and 1170 cm^{-1}, which are related to symmetrical and asymmetrical vibrations of the bridging oxygens in P-O-P linkages, are the most pronounced bands. Surprisingly the HH polarization enhanced substantially the band around 700 cm^{-1} and 1180 cm^{-1}, related to the symmetrical vibrations of linkages and bonds, respectively. The vibrational modes of ZnTe NCs are observed at around 215 cm^{-1} (1LO phonon), 430 cm^{-1} (2LO phonon) and 644 cm^{-1} (3LO phonon), as shown in Fig. 3 [33- 35].

The thermal lens signals and cooling curves of the samples are presented in Fig. 4 and 5, respectively. Based on the obtained data, the thermo-optical parameters are calculated and listed in table.2. The uncertainty values are based on the standard errors of fitting process. Since the undoped PZABP glass doesn't show absorption at the pump laser wavelength, it was not possible to obtain a thermal lens signal, while the doped PZABP samples present enough absorption in accordance with the model [25]. The sample PZABP+5Cr furnished a thermal diffusivity $D = 2.5$ cm^2/s that is comparable to the one reported in reference [36] for nonmagnetic PZABP glasses doped with 1% of Yb^{3+}. Comparing the samples PZABP+5Cr and ZnMnCrTe- 5%, it is clear that the formation of the co-doped Cr and Mn NCs decreased the thermal conductivity by about 24%. However, the calculated values of thermal conductivity do not show a regular behavior by the addition of Cr ions. Thermal diffusivity values show different effect by addition of NCs inside the glassy system. Thermal diffusivity increases by introduction of NCs whereas thermal conductivity decreases. This is a direct result of the changes of the specific heat by NCs. Concerning optical path variation with temperature, $\frac{dS}{dT}$, it is observed that its values decrease monotonically with Cr concentration.

Discussion:

From UV-Vis spectrum, it is turned out that the Cr^{2+} ions appear with the assistance of ZnTe NCs due to exchange the ion position with the Zn^{2+} in the ZnTe NCs, while the Cr^{3+} ions are formed in PZABP+ 5Cr.

For a more precise analysis of Raman spectra, multiple bands fit is carried out for the polarized Raman to discriminate the effects of ZnTe, Mn and Cr. The band intensities, full width at half maximum (FWHM) and Raman shifts were analyzed to compare PZABP with PZABP+5Cr and ZnMnCrTe-0.5% with ZnMnCrTe-10.0%, as shown in Fig. 6 and 7, respectively. It can be noted that both bands decrease by the addition of the Cr and Mn ions as well as the ZnTe NCs. Fig. 6 shows that by adding the Cr ions, the ratio of the Raman intensity of the Q^1 to Q^2 increases considerably showing breaks in the phosphate chains. On the other hand, due to the coordination number of Cr^{3+}, these cations can turn the phosphate chains into ring structures by attracting pyrophosphates around the cations. Therefore, the frequencies and even the FWHM of the PO_2 bands are cation dependent [30]. Strong cations can increase the disorder degree and change the phosphate bond distribution and consequently the FWHM of the Raman bands. The observed Raman shift from 1115 to 1130 cm^{-1} as the Cr concentration increases may be attributed to the formation of a bond between Cr cations and a non-bridging oxygen of $(P-O)^-$. Moreover, the band intensities around 1258 and 1176 cm^{-1} decrease as Cr concentration increases. This effect may be related to asymmetry and symmetry stretch vibrations of non-bridging oxygens in Q^2 units presenting additional evidence that the Cr addition depolymerizes the phosphate network. It should be mentioned that, according to the Hoppe model, despite depolymerization processes, all terminal oxygens interact with cations in the system such that a weak re-polymerization is expected [37]. The bending modes characterized by a broad feature between 250 cm^{-1} and 450 cm^{-1} are attenuated by adding Cr^{3+}due to the attraction between the strong cations with the delocalized electrons in P-O bonds [38- 40]. As shown in Fig. 7, a depolymerization process is observed in ZnMnCrTe-10.0% such that the band around 1235 cm^{-1}, which is related to the P-O double bond in Q^3 structure, disappears. It shows that the addition of Cr ions prevents the increase of bridging oxygens in the phosphate network [41]. The sharp Raman bands of ZnTe NCs reveal their crystalline structure. Since the Cr atomic mass is lighter than Zn it leads to an increase in the vibration

amplitude [19]. Fig.7 demonstrates that the NCs Raman bands are intensified by increasing Cr concentration. However, the amplification observed at 1LO frequency is greater than the one for 2LO frequency. The same behavior is observed for the 2LO band compared to 3LO, where almost no change is observed around 644 cm^{-1}. The Cr presence cannot change the Raman shift of NCs because the interlayer distances of the NCs remain unchanged with substitution of Cr with Zn atoms. It is turned out that adding ZnTe NC and Cr and Mn ions break the phosphate chains in the matrix [42, 43].

Concerning the thermal parameters of the samples, it is worth to mention that phosphate glasses usually have high thermal diffusivity making them good candidates for high power laser applications [44]. Thermal diffusivities of glasses are normally in the range from 10^{-3} cm^2/s to 10^{-2} cm^2/s. Another important point is that when *I(t)* increases with time, the samples reveal a convergent lens effect, while in the opposite case, the lens is divergent. Most oxide glasses produce a convergent lens effect (as is the case here) [26]. The relative high value of thermal conductivity of PZABP+5Cr compared to other glasses may be due to the presence of Cr^{3+} and consequently the free carriers, in this case, holes. These free carriers, in turn, can increase the electronic contribution of the thermal conductivity [45].

The reduction of thermal conductivity of ZnMnCrTe-5% compared to PZABP+5Cr shows that still the lattice contribution has major effect. Although the Cr doping increases the free carrier concentration the electronic contribution of thermal conductivity is still negligible compared to the lattice contribution of the glasses. The electronic heat capacity is proportional to the temperature while the phonon contribution is proportional to the cube of temperature [45].

The amorphous materials that are embedded with nanostructures, surfaces and interfaces have lower thermal conductivity versus their undoped counterparts [45, 46]. Moreover, the presence of NCs may result in phonon confinement that may decrease the thermal conductivity [47].

The optical path variation with temperature is expressed by $\frac{dS}{dT} = \frac{dn}{dT} + n\alpha$, in which n and α are the refractive index and thermal expansion coefficient, respectively. Since materials with low $\frac{dn}{dT}$ and low α

are suitable for high power laser applications, low values of $\frac{dS}{dT}$ are appropriate, which occurred by Cr addition in the samples [48].

The nanostructures in a glassy system reduce thermal conductivity which is technologically not desirable in high power laser applications whereas it is a favorable factor for efficiency of spintronic devices exploiting spin Seebeck effect [49]. In summary, the thermo-optical behaviors of the proposed DMS nanocomposite systems evidence that subtle alterations in their structure and doping could change the thermal properties that should be considered in both optical and magnetic applications. For example, in the latter case, possible induced changes in spin Seebeck effect by thermal conductivity can be measured through an inverse spin-Hall technique [9].

Conclusions:

Structural and thermal studies of ZnTe NCs semiconductors doped with Mn and Cr grown in phosphate glasses are performed. The absorption spectra in the UV-Vis region indicate the good incorporation of Cr^{2+} and Mn^{2+} in the ZnTe doped structures and Cr^{3+} ions in PZABP+5Cr. It is found from absorption spectra that the Cr ions addition prevents the formation of ZnTe QDs in the glasses. The Raman measurements show that the Cr and Mn ions break long phosphate chains by reduction of bridging oxygens through the junction between the cations and PO_4 anions. The amplification of the Raman bands related to the Q^1 structure is another evidence of breaking of the phosphate chains in the glasses. Using the polarizer in the Raman setup allows us to identify which vibrations are symmetrical. The results show that NCs structures decrease thermal conductivity of the glasses by introducing new surfaces and interfaces that cause boundary scattering of phonons. The reductions in thermal conductivity are considered as an advantage for materials in which a spin current is generated via spin Seebeck effect. Despite of an irregular behavior that is observed in thermal conductivity by changing Cr concentration, a monotonic reduction occurs in $\frac{dS}{dT}$ values in the samples, which is an advantage for the optical applications. In order to acquire non-linear optical effects, it may be important to maintain the degree of oxidation of Cr in 2+.

Because in the case of Cr^{3+} there may be a greater structural change that may impair the diffusion of heat, increasing the heating of the sample.

Acknowledgments

References:

[1]   A. MacDonald, P. Schiffer, N. Samarth, Ferromagnetic semiconductors: moving beyond (Ga, Mn)As, Nature Materials 4 (2005) 195–202.

[2]   T. Story, R.R. Galazka, R.B. Framkel, P.A. Wolff, Carrier-concentration–induced ferromagnetism in PbSnMnTe, Physical Review Letters 56 (1986) 777.

[3]   M.I. Dyakonov, Spin physics in semiconductors, Vol. 1, Springer, Berlin, 2008.

[4]   H. Saito, V. Zayets, S. Yamagata, K. Ando, Room-Temperature Ferromagnetism in a II-VI Diluted Magnetic Semiconductor $Zn_{1-x}Cr_xTe$, Physical Review Letters 90 (2003) 207202.

[5]   J. Eilers, E. Groeneveld, C.M. Donegá, A. Meijerink, Optical properties of Mn-doped ZnTe magic size nanocrystals, J. Phys. Chem. Lett 3 (2012) 1663–1667

[6]   D.A. Reddy, S. Sambasivam, G. Murali, B. Poornaprakash, R.P. Vijayalakshmi, Y. Aparna, B.K. Reddy, J.L. Rao, Effect of Mn co-doping on the structural, optical and magnetic properties of ZnS: Cr nanoparticles, Journal of Alloys and Compounds 537 (2012) 208-215.

[7]   M.C. Wingert, J. Zheng, S. Kwon, R. Chen, Thermal transport in amorphous materials: a review, Semiconductor Science and Technology 31 (2016) 113003.

[8]   K. Vandaele, S.J. Watzman, B. Flebus, A. Prakash, Y. Zheng, S.R. Boona, J.P. Heremans, Thermal spin transport and energy conversion, Materials Today Physics 1 (2017) 39-49.

[9]   S. Maekawa, S.O. Valenzuela, T. Kimura, E. Saitoh, Spin Current. Oxford University Press, 2017.

[10]   A. Hirohata, K. Yamada, Y. Nakatani, L. Prejbeanu, B. Diény, P. Pirro, B. Hillebrands, Review on spintronics: Principles and device applications, Journal of Magnetism and Magnetic Materials 509 (2020) 166711.

[11]   F.C. Peiris, B.A. Kowalski, X. Liu, U. Bindley, J.K. Furdyna, Optical properties of molecular beam epitaxy-grown $Zn_{1-x}Mn_xTe$ thin films measured by complementary techniques, Journal of Applied Physics 94 (2003) 4717-4719.

[12] Y. Yu, O. Byungsung, Y. Yoon, J.B. Kim, Y.D. Choi, Effect of Mn concentration on photoluminescence characteristics of $Zn_{1-x}Mn_xTe$ epilayers, Thin Solid Films 426 (2003) 265-270.

[13] S.H. Lee, Y.J. Kim, J. Park, Shape evolution of ZnTe nanocrystals: nanoflowers, nanodots, and nanorods, Chemistry of Materials 19 (2007) 4670-4675.

[14] K. Ersching, C.E.M. Campos, J.C. De Lima, T.A. Grandi, S.M. Souza, D.L. Da Silva, P. S. Pizani, X-ray diffraction, Raman, and photoacoustic studies of ZnTe nanocrystals, Journal of Applied Physics 105 (2009) 123532.

[15] N.O. Dantas, A.S. Silva, E.S. Freitas Neto, S..A. Lourenço, Thermal activated energy transfer between luminescent states of Mn^{2+}-doped ZnTe nanoparticles embedded in a glass matrix, Physical Chemistry Chemical Physics 14 (2012) 3520-3529.

[16] A.S. Silva, S.A. Lourenço, N.O. Dantas, Mn concentration-dependent tuning of Mn^{2+} d emission of $Zn_{1-x}Mn_xTe$ nanocrystals grown in a glass system, Physical Chemistry Chemical Physics 18, (2016) 6069-6076.

[17] A.M. Freitas, M.J.V. Bell, V. Anjos, A.S. Pinheiro, and N.O. Dantas, Thermal analyzes of phosphate glasses doped with Yb^{3+} and ZnTe nanocrystals, Journal of Luminescence 169 (2016) 353-358.

[18] G.H. Silva, V. Anjos, M.J.V. Bell, A.P. Carmo, A.S. Pinheiro, N.O. Dantas, Eu^{3+} emission in phosphate glasses with high UV transparency, Journal of luminescence 154 (2014) 294-297.

[19] A.S. Silva, S.A. Lourenço, M.A.T. da Silva, N.O. Dantas, Optical properties of Cr-doped $Zn_{1-x}Mn_xTe$ semimagnetic nanocrystals, Applied Physics Letters 112 (2018) 063102.

[20] A.S. Pinheiro, A.M. Freitas, G.H. Silva, M.J.V. Bell, V. Anjos, A.P. Carmo, and N.O. Dantas, Laser performance parameters of Yb^{3+} doped UV-transparent phosphate glasses, Chemical Physics Letters 592 (2014) 164-169.

[21] N.O. Dantas, A.S. Silva, W.E. Feria Ayta, S.W. da Silva, P.C. de Morais, M.A. Pereira-da-Silva, G.E. Marques, Dilute magnetism in $Zn_{1-x}Mn_xTe$ nanocrystals grown in a glass template, Chemical Physics Letters 541 (2012) 44-48.

[22] A.S. Silva, A. Franco Jr, F. Pelegrini, N.O. Dantas, Paramagnetic behavior at room temperature of $Zn_{1-x}Mn_xTe$ nanocrystals grown in a phosphate glass matrix by the fusion method, Journal of Alloys and Compounds 647 (2015) 637-643.

[23] L.M. Moreira, E. A. Carvalho, M.J.V. Bell, V. Anjos, A.C. Sant'Ana, A.P.P. Alves, B. Fragneaud, L.A. Sena, B.S. Archanjo, C.A. Achete, Thermo-optical properties of silver and gold nanofluids, Journal of Thermal Analysis and Calorimetry 114 (2013) 557-564.

[24] D.N. Messias, C. Jacinto, M.J.V. Bell, T. Catunda, Thermal and Optical Properties of Yb^{3+} and Nd^{3+} Doped Phosphate Glasses Determined by Thermal Lens Technique, IEEE journal of quantum electronics 43 (2007) 751-757.

[25] S.M. Lima, J.A. Sampaio, T. Catunda, A.C. Bento, L.C.M. Miranda, M.L. Baesso, Mode-mismatched thermal lens spectrometry for thermo-optical properties measurement in optical glasses: a review, Journal of Non-Crystalline Solids 273 (2000) 215-227.

[26] M.J.V. Bell, N.O. Dantas, L.R.P. Kassab, V. Anjos, Thermo-optical properties of glasses doped with semiconductor or metallic nanoparticles and rare-earth ions, in: L.P.R. Kassab, S.J.L. Ribeiro, R. Rangel-Rojo (Eds.) In Nanophotonics, Nanocomposites for Photonic and Electronic Applications, Elsevier, 2020, pp. 5-29

[27] E.A. Carvalho, A.M. Freitas, G.H. Silva, M.J.V. Bell, L.R.P. Kassab, V. Anjos, Thermal and structural analysis of germanate glass and thin films co-doped with silver nanoparticles and rare earth ions with insights from visible and Raman spectroscopy, Vibrational Spectroscopy 87 (2016) 143-148.

[28] A.S. Pinheiro, Z.M. da Costa, M.J.V. Bell, V. Anjos, S.T. Reis, C.S. Ray, Thermal characterization of glasses prepared from simulated compositions of lunar soil JSC-1A, Journal of Non-Crystalline Solids 359 (2013) 56-59.

[29] Y.A. Nitsuk, Energy states of a Cr 2+ ion in ZnSe crystals, Semiconductors 47 (2013) 736-739.

[30] A.K. Yadav, P. Singh, A review of the structures of oxide glasses by Raman spectroscopy, RSC advances 5 (2015) 67583-67609.

[31] J. Schwarz, H. Tichá, L. Tichy, R. Mertens, Physical properties of PbO-ZnO-P_2O_5 glasses. I. Infrared and Raman spectra, Journal of Optoelectronics and Advanced Materials 6 (2004) 737-746.

[32] R.K. Brow, Review: the structure of simple phosphate glasses, Journal of Non-Crystalline Solids 263 (2000) 1-28.

[33] N.O. Dantas, A.S. Silva, S.W. Silva, P.C. Morais, M.A. Pereira-da-Silva, G.E. Marques, ZnTe nanocrystal formation and growth control on UV-transparent substrate, Chemical Physics Letters 500 (2010) 46-48.

[34] K. Ersching, C.E.M. Campos, J.C. De Lima, T.A. Grandi, S.M. Souza, D.L. Da Silva, P.S. Pizani, X-ray diffraction, Raman, and photoacoustic studies of ZnTe nanocrystals, Journal of Applied Physics 105 (2009) 123532.

[35] J.C. Irwin, J. LaCombe, Raman scattering in ZnTe, Journal of Applied Physics 41 (1970) 1444-1450.

[36] R.F. Falci, A.M. Freitas, G.H. Silva, A.S. Pinheiro, N.O. Dantas, V. Anjos, M.J.V. Bell, Quantum efficiency of Yb^{3+}–ZnTe co-doped phosphate glass system, Journal of Luminescence 176 (2016) 381-386.

[37] U. Hoppe, A structural model for phosphate glasses, Journal of Non-Crystalline Solids 195, (1996) 138-147.

[38] K. Griebenow, C.B. Bragatto, E.I. Kamitsos, L. Wondraczek, Mixed-modifier effect in alkaline earth metaphosphate glasses, Journal of Non-Crystalline Solids 481 (2018) 447-456.

[39] R.O. Omrani, S. Krimi, J.J. Videau, I. Khattech, A. El Jazouli, M. Jemal, Structural and thermochemical study of Na_2O–ZnO–P_2O_5 glasses, Journal of Non-Crystalline Solids 390 (2014) 5-12.

[40] A. Moguš-Milanković, L. Pavić, S.T. Reis, D.E. Day, M. Ivanda, Structural and electrical properties of $Li_2O–ZnO–P_2O_5$ glasses, Journal of Non-Crystalline Solids 356 (2010) 715-719.

[41] Y. Takamatsu, Y. Daiko, S. Kohara, K. Suzuya, A. Mineshige, T. Yazawa, The state of POnb non-bridging oxygen and proton incorporation in binary MO· P_2O_5 (M= Ca, Mg) phosphate glasses, Solid State Ionics 245 (2013) 19-23.

[42] Y.M. Lai, X. F. Liang, S.Y. Yang, J.X. Wang, B.T. Zhang, Raman spectra study of iron phosphate glasses with sodium sulfate, Journal of Molecular Structure 1013 (2012) 134-137.

[43] K.S. Al Mugren, Y. El Sayed, H. Shoukry, A. El Taher, Raman and Uv-Vis-NIR spectroscopy of phosphate glasses, Digest Journal of Nanomaterials and Biostructures 11 (2016) 607-614.

[44] J.H. Campbell, T.I. Suratwala, Nd-doped phosphate glasses for high-energy/high-peak-power lasers, Journal of Non-Crystalline Solids 263 (2000) 318-341.

[45] T.M. Tritt, Thermal conductivity: theory, properties, and applications. Springer Science & Business Media, 2005.

[46] F.B. Juangsa, Y. Muroya, M. Ryu, J. Morikawa, Tomohiro Nozaki, Comparative study of thermal conductivity in crystalline and amorphous nanocomposite, Applied Physics Letters 110 (2017) 253105.

[47] A. Balandin, K.L. Wang, Significant decrease of the lattice thermal conductivity due to phonon confinement in a free-standing semiconductor quantum well, Physical Review B 58 (1998) 1544.

[48] T.Y. Fan, J.L. Daneu, Thermal coefficients of the optical path length and refractive index in YAG, Applied Optics 37 (1998) 1635-1637.

[49] H. Adachi, K. Uchida, E. Saitoh, S. Maekawa, Theory of the spin Seebeck effect, Reports on Progress in Physics 76 (2013) 036501.

Tables and figures:

Wavenumber (cm^{-1})	Assignment	Ref.
1325	P-O double bond in Q^3 unit	17, 18
1260	Asymmetric stretching of non-bridging oxygen on a Q^2 unit	17
1176	Symmetric stretching of non-bridging oxygen on a Q^2 unit	17
1080	P-O symmetric groups in Q^1 pyrophosphate	17, 18
970	Symmetric stretching orthophosphate [PO4]$^{-3}$ in Q^0 unit	17
745	Symmetric stretching of P-O-P linkage in Q^1	17, 18, 20
697	Symmetric stretching of P-O-P linkage in Q^2	17, 18
585	Bending vibration of P-O bonds or Zn-O and Pb-O vibration	18
350	chain of O-P-O bending motions	17
624	3LO phonons of ZnTe	28-30
426	2LO phonons of ZnTe	28-30
214	1LO phonons of ZnTe	28-30

Table 1.

Sample	A_e (cm^{-1})	t_c (m.sec)	$D \times 10^{-3}$ (cm^2/sec)	ρc (J/cm^3.K)	$K \times 10^{-3}$ (W/cm.K)	$dS/dT \times 10^{-6}$ K^{-1}
PZABP+ **5Cr**	2.8125	1.7 ± 0.3	2.51 ± 0.04	2.41 ± 0.01	6.04 ± 0.09	1.907
ZnMn**Cr**Te- 0.5%	1.858	1.6 ± 0.4	2.64 ± 0.07	2.10 ± 0.01	5.54 ± 0.15	1.674
ZnMn**Cr**Te- 1.0%	1.846	2.0 ± 0.5	2.07 ± 0.05	2.10 ± 0.01	4.35 ± 0.11	0.959
ZnMn**Cr**Te- 5.0%	3.143	2.1 ± 0.4	1.97 ± 0.03	2.32 ± 0.01	4.56 ± 0.07	0.922
ZnMn**Cr**Te- 10%	7.176	---	---	2.26 ± 0.01	--	---

Table 2.

chopper

488 nm – pump beam

643.8 nm – probe beam

PD2

pinhole

M

M

M

M

M

M

PD1

L

L
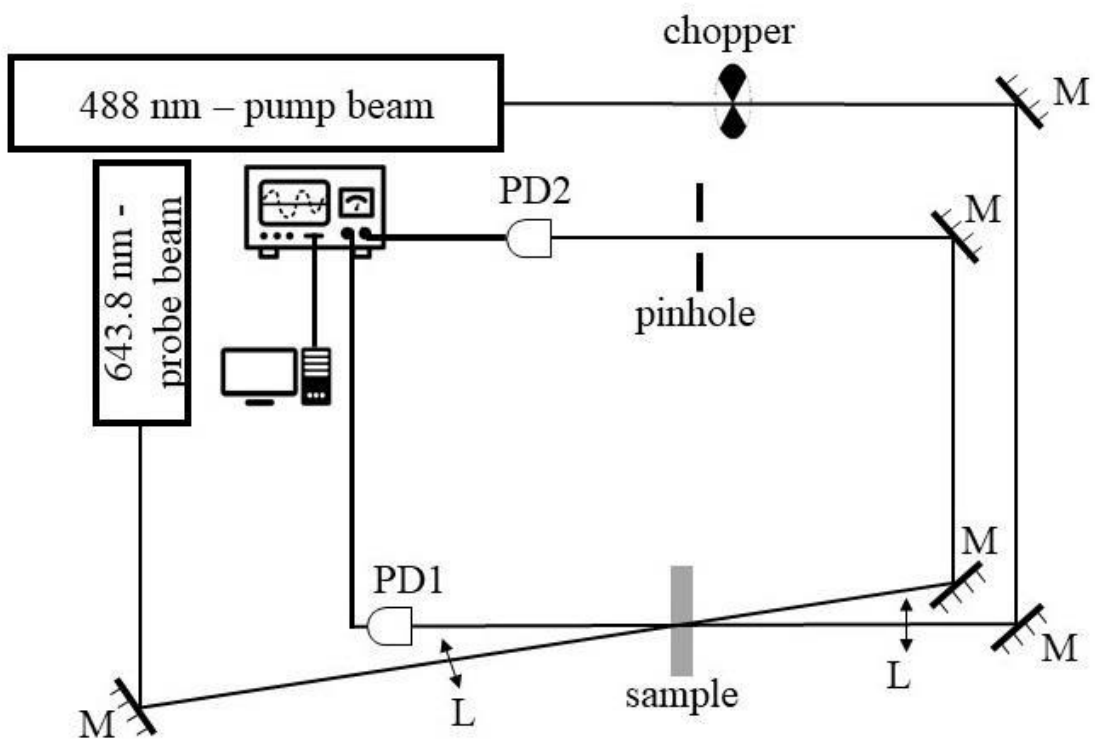
sample

Fig. 1.
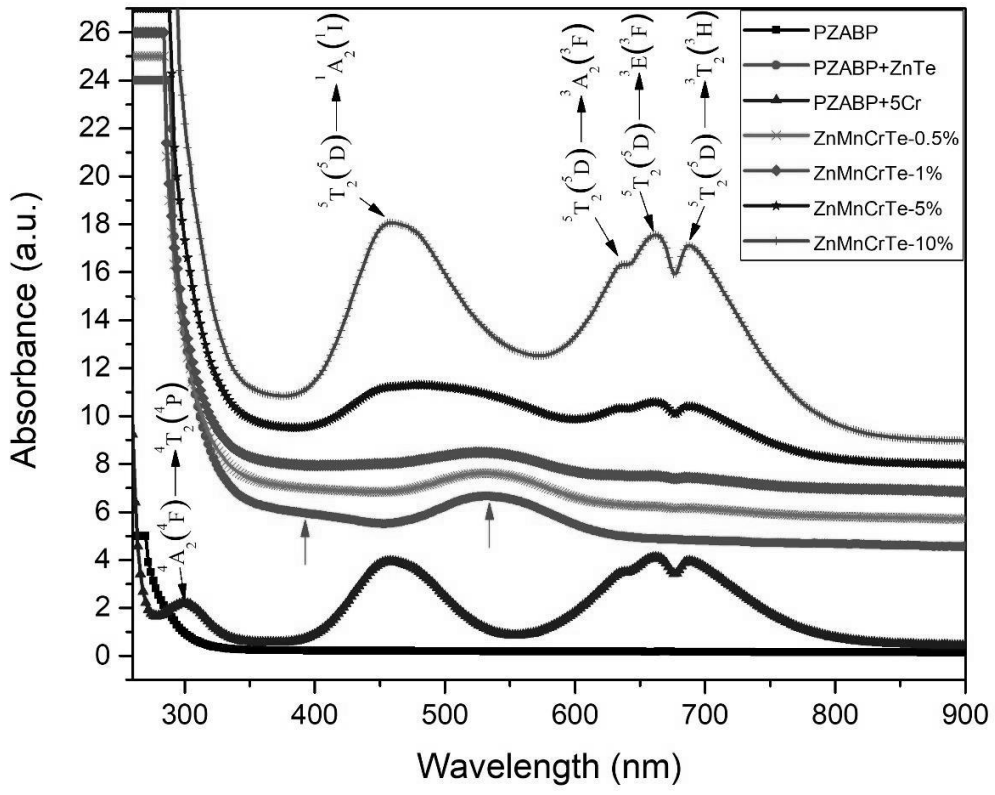
Fig. 2.
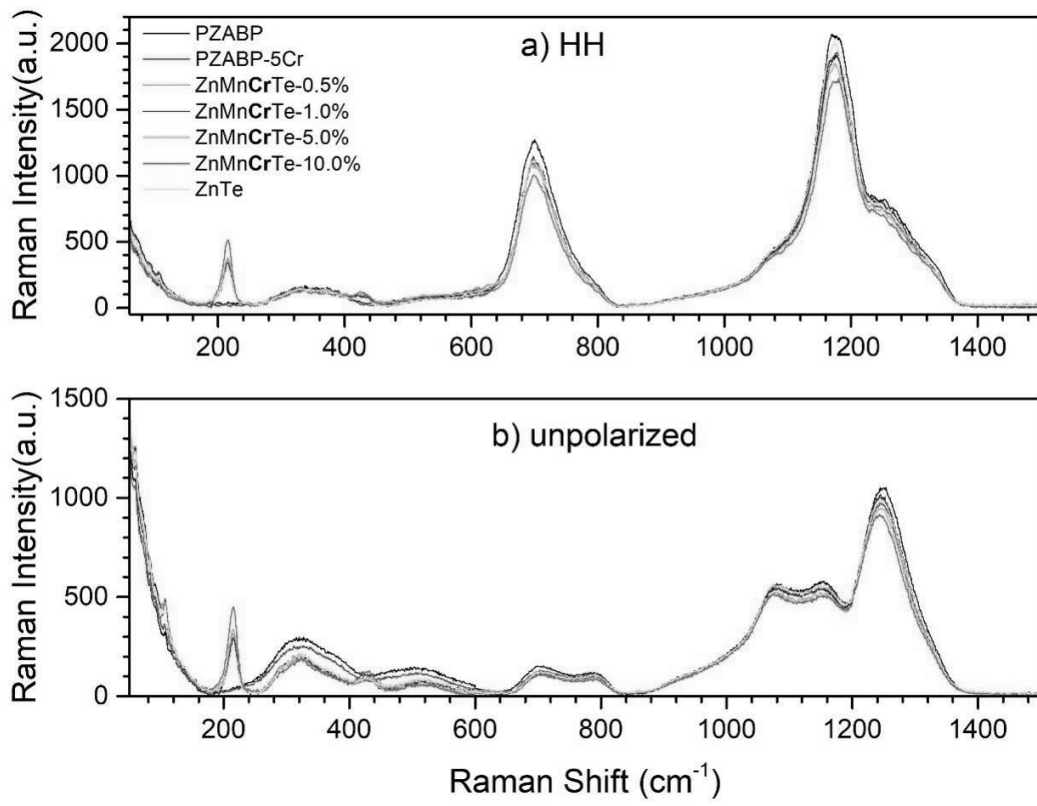
Fig. 3.
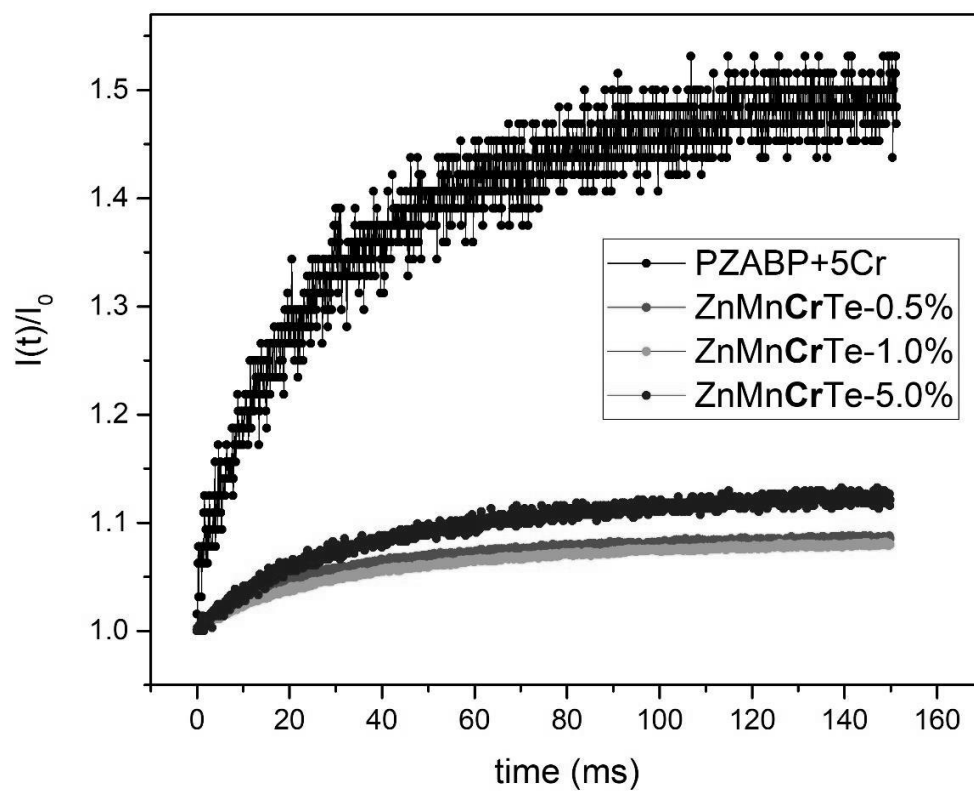
Fig. 4.
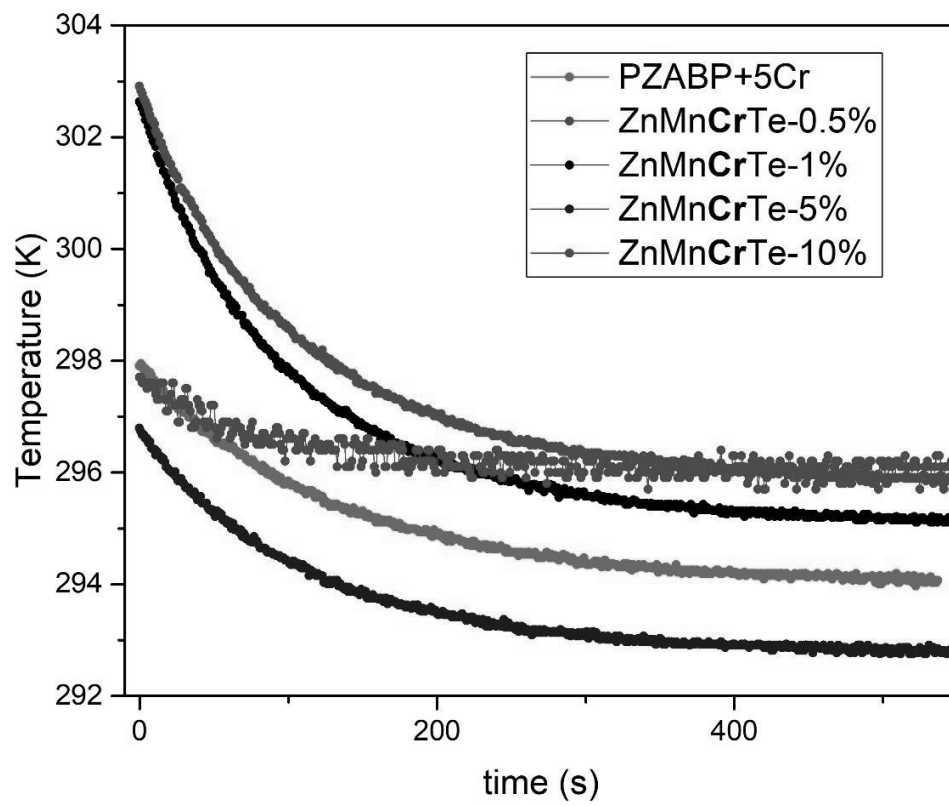
Fig. 5.
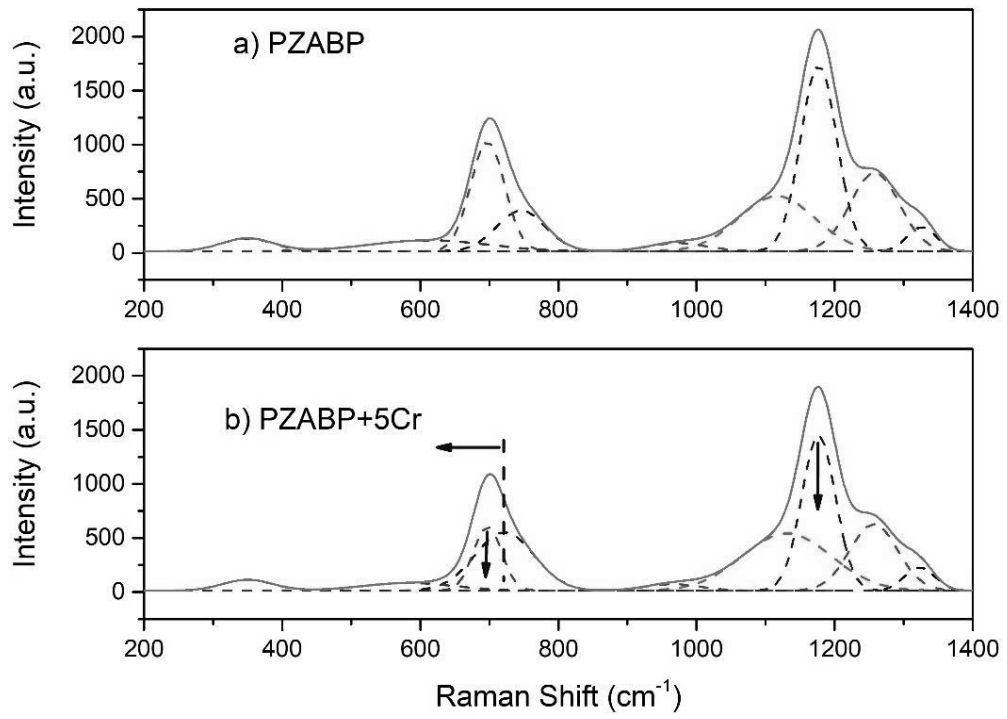
Fig. 6.
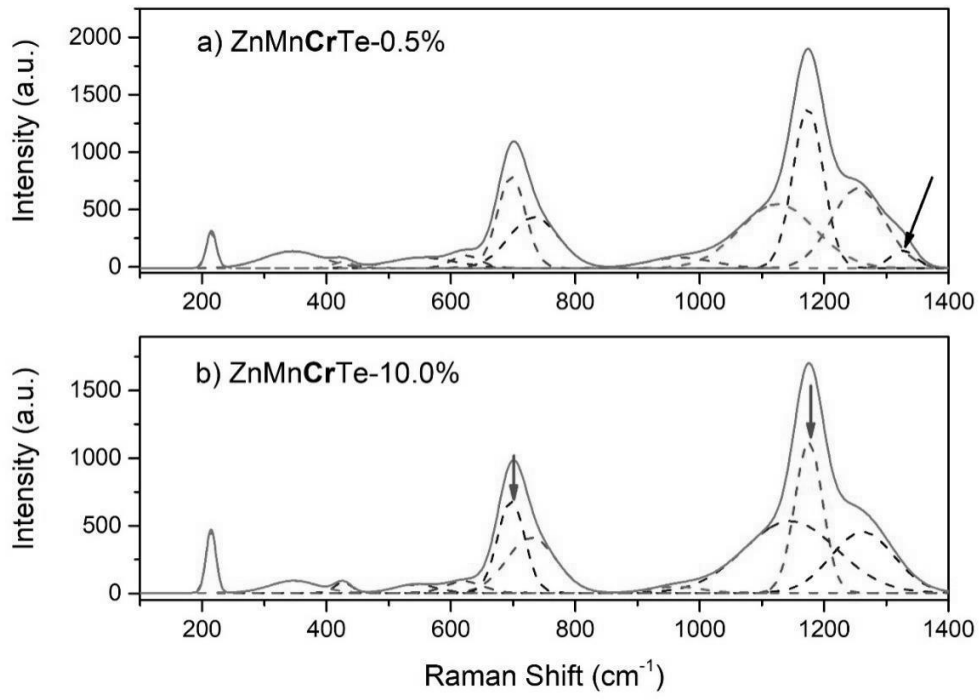
Fig. 7.

Figure Captions:

Figure 1. A scheme of thermal lens technique. In this image, L is lens, M is mirror and PD is photodiode.

Figure 2: UV-Vis spectrum of the samples. Red arrows show the bands associated with ZnTe nanostructures.

Figure 3: Raman spectrum of the samples (a) in HH situation and (b) unpolarized.

Figure 4: The normalized probe intensity versus time in the thermal lens setup for the samples.

Figure 5: Cooling curves of the samples measured by specific heat capacity technique.

Figure 6: Multiple peaks analysis of Raman spectrum for (a) PZABP and (b) PZABP+5Cr. The arrows in (b) indicate the changes in the Raman shift and intensities.

Figure 7: Multiple peaks analysis of Raman spectrum for PZABP with ZnTe and different Cr concentration. Black arrows in (a) shows presence of the band correspond to the Q^3 structures which are disappeared in (b). The red arrows in (b) indicate the shifts in the bands intensity.

Table Captions:

Table 1: Raman bands and assignments.

Table 2: Thermo-optical properties of the samples.

Bibliography

1 WEISBUCH, C.; BENISTY, H. Progress in the control of the light–matter interaction in semiconductors. *Solid state communications*, Elsevier, v. 135, n. 9-10, p. 627–637, 2005.

2 KASAP, S.; CAPPER, P. *Springer handbook of electronic and photonic materials.* [S.l.]: Springer, 2017.

3 OTHONOS, A. Probing ultrafast carrier and phonon dynamics in semiconductors. *Journal of applied physics*, AIP, v. 83, n. 4, p. 1789–1830, 1998.

4 BASAK, A. K. *ULTRAFAST CARRIER AND LATTICE DYNAMICS STUDIES IN GaAs WITH INTENSE OPTICAL EXCITATION.* Tese (Doutorado) — University of Pittsburgh, 2010.

5 MAN, M. K. et al. Imaging the motion of electrons across semiconductor heterojunctions. *Nature nanotechnology*, Nature Publishing Group, v. 12, n. 1, p. 36, 2017.

6 RUDOLPH, P.; JURISCH, M. Bulk growth of gaas an overview. *Journal of crystal growth*, Elsevier, v. 198, p. 325–335, 1999.

7 HASE, M. Ultrafast dynamics of plasmon-phonon coupling: Estimation of electron mobility in gaas. *physica status solidi c*, Wiley Online Library, v. 5, n. 1, p. 364–366, 2008.

8 NIE, X. et al. Transient transition from free carrier metallic state to exciton insulating state in GaAs by ultrafast photoexcitation. *New Journal of Physics*, IOP Publishing, v. 20, n. 3, p. 033015, 2018.

9 LIN, W.-Z. et al. Femtosecond absorption saturation studies of hot carriers in GaAs and AlGaAs. *IEEE journal of quantum electronics*, IEEE, v. 24, n. 2, p. 267–275, 1988.

10 TKACHENKO, V.; MEDVEDEV, N.; ZIAJA, B. Transient changes of optical properties in semiconductors in response to femtosecond laser pulses. *Applied Sciences*, Multidisciplinary Digital Publishing Institute, v. 6, n. 9, p. 238, 2016.

11 RODRIGUES, L. N. et al. Resonant electronic Raman scattering: A BCS -like system. *Physical Review B*, APS, v. 93, n. 20, p. 205409, 2016.

12 ANJOS, V.; IORIATTI, L. Collective and single-particle excitations in Raman scattering of multilayer δ-doped systems. *Physical Review B*, APS, v. 63, n. 3, p. 035404, 2000.

13 WRIGHT, O. B. et al. Ultrafast carrier diffusion in gallium arsenide probed with picosecond acoustic pulses. *Physical Review B*, APS, v. 64, n. 8, p. 081202, 2001.

14 CORKUM, P. et al. *Ultrafast Phenomena XVI: Proceedings of the 16th International Conference, Palazzo Dei Congressi Stresa, Italy, June 9–13, 2008.* [S.l.]: Springer Science & Business Media, 2010. v. 92.

15   SHAH, J. *Ultrafast spectroscopy of semiconductors and semiconductor nanostructures.* [S.l.]: Springer Science & Business Media, 2013. v. 115.

16   YU, X.-Y. *Advances in Microfluidics: New Applications in Biology, Energy, and Materials Sciences.* [S.l.]: BoD–Books on Demand, 2016.

17   SIMON, J. D. *Ultrafast dynamics of chemical systems.* [S.l.]: Springer Science & Business Media, 2012. v. 7.

18   PRASANKUMAR, R. P.; TAYLOR, A. J. *Optical techniques for solid-state materials characterization.* [S.l.]: CRC Press, 2016.

19   SHEN, X. et al. Experimental study of electron-phonon coupling and electron internal thermalization in epitaxially grown ultrathin copper films. *Physical Review B*, APS, v. 91, n. 4, p. 045129, 2015.

20   KING, S. B. et al. Trapped electrons at the amorphous solid water/vacuum interface as possible reactants in a water splitting reaction. *The Journal of Physical Chemistry C*, ACS Publications, v. 121, n. 13, p. 7379–7386, 2017.

21   YAHNG, J. et al. Femtosecond degenerate and nondegenerate pump-probe experiments in bulk GaAs below the band gap. *Journal of the Optical Society of Korea*, Optical Society of Korea, v. 1, n. 2, p. 100–103, 1997.

22   BENNETT, B. R.; SOREF, R. A.; ALAMO, J. A. D. Carrier-induced change in refractive index of InP, GaAs and InGaAsP. *IEEE Journal of Quantum Electronics*, IEEE, v. 26, n. 1, p. 113–122, 1990.

23   WANG, H.-C. et al. Non-degenerate fs pump-probe study on InGaN with multi-wavelength second-harmonic generation. *Optics express*, Optical Society of America, v. 13, n. 14, p. 5245–5252, 2005.

24   TOMMASI, R.; LANGOT, P.; VALLEE, F. Femtosecond hole thermalization in bulk GaAs. *Applied physics letters*, AIP, v. 66, n. 11, p. 1361–1363, 1995.

25   BABILOTTE, P. et al. Transition from piezoelectric to deformation potential mechanism of hypersound photogeneration in n-doped GaAs semiconductors. *Journal of Applied Physics*, American Institute of Physics, v. 109, n. 6, p. 064909, 2011.

26   ISHIOKA, K. et al. Sub-picosecond acoustic pulses at buried GaP/Si interfaces. *Applied Physics Letters*, AIP Publishing LLC, v. 111, n. 6, p. 062105, 2017.

27   HALL, K. L. et al. Heterodyne pump–probe technique for time-domain studies of optical nonlinearities in waveguides. *Optics letters*, Optical Society of America, v. 17, n. 12, p. 874–876, 1992.

28   SUN, C.-K. et al. Heterodyne nondegenerate pump–probe measurement technique for guided-wave devices. *Optics letters*, Optical Society of America, v. 20, n. 2, p. 210–212, 1995.

29   HALL, K. et al. Femtosecond index nonlinearities in ingaasp optical amplifiers. *Applied physics letters*, American Institute of Physics, v. 62, n. 12, p. 1320–1322, 1993.

30   CHEN, X.; WANG, K.; BEARD, M. C. Ultrafast probes at the interfaces of solar energy conversion materials. *Physical Chemistry Chemical Physics*, Royal Society of Chemistry, v. 21, n. 30, p. 16399–16407, 2019.

31   YANG, J.-A. et al. Novel electron-phonon relaxation pathway in graphite revealed by time-resolved raman scattering and angle-resolved photoemission spectroscopy. *Scientific reports*, Nature Publishing Group, v. 7, p. 40876, 2017.

32   BASAK, A. K. et al. Ultrafast coupling of coherent phonons with a nonequilibrium electron-hole plasma in GaAs. *Phys. Rev. B*, American Physical Society, v. 91, p. 125201, Mar 2015. Disponível em: ⟨https://link.aps.org/doi/10.1103/PhysRevB.91.125201⟩.

33   BOYD, R. W. *Nonlinear optics*. [S.l.]: Elsevier, 2003.

34   EICHLER, H. J.; GUNTER, P.; POHL, D. W. *Laser-induced dynamic gratings*. [S.l.]: Springer, 2013. v. 50.

35   BEJOT, P.; KASPARIAN, J. Energy conservation in self-phase modulation. *Physical Review A*, APS, v. 97, n. 6, p. 063835, 2018.

36   CUNDIFF, S. T. Coherent spectroscopy of semiconductors. *Optics express*, Optical Society of America, v. 16, n. 7, p. 4639–4664, 2008.

37   HEGARTY, J. et al. Resonant degenerate four-wave mixing in GaAs multiquantum well structures. *Applied Physics Letters*, American Institute of Physics, v. 40, n. 2, p. 132–134, 1982.

38   LIU, A. et al. Non-markovian exciton-phonon interactions in core-shell colloidal quantum dots at femtosecond timescales. *Phys. Rev. Lett.*, American Physical Society, v. 123, p. 057403, Aug 2019. Disponível em: ⟨https://link.aps.org/doi/10.1103/PhysRevLett.123.057403⟩.

39   SHIN, H. J. et al. Ultrafast nonlinear travel of hot carriers driven by high-field terahertz pulse. *Journal of Physics B: Atomic, Molecular and Optical Physics*, IOP Publishing, v. 51, n. 14, p. 144003, 2018.

40   CUNNINGHAM, P. D. Accessing terahertz complex conductivity dynamics in the time-domain. *IEEE Transactions on Terahertz Science and Technology*, IEEE, v. 3, n. 4, p. 494–498, 2013.

41   KAINDL, R. A. et al. Transient terahertz spectroscopy of excitons and unbound carriers in quasi-two-dimensional electron-hole gases. *Physical Review B*, APS, v. 79, n. 4, p. 045320, 2009.

42   SCHMUTTENMAER, C. A. Exploring dynamics in the far-infrared with terahertz spectroscopy. *Chemical reviews*, ACS Publications, v. 104, n. 4, p. 1759–1780, 2004.

43   HAFEZ, H. et al. Intense terahertz radiation and their applications. *Journal of Optics*, IOP Publishing, v. 18, n. 9, p. 093004, 2016.

44   MIN, L.; MILLER, R. D. Subpicosecond reflective electro-optic sampling of electron-hole vertical transport in surface-space-charge fields. *Applied physics letters*, American Institute of Physics, v. 56, n. 6, p. 524–526, 1990.

45 ISHIOKA, K. et al. Coherent phonon spectroscopy characterization of electronic bands at buried semiconductor heterointerfaces. *Applied Physics Letters*, AIP Publishing LLC, v. 108, n. 5, p. 051607, 2016.

46 GLINKA, Y. et al. Electro-optic nature of ultrafast pump-probe reflectivity response from multilayer semiconductor heterostructures. *Journal of Applied Physics*, American Institute of Physics, v. 103, n. 4, p. 043708, 2008.

47 HASE, M. et al. Coherent phonon-induced optical modulation in semiconductors at terahertz frequencies. *New Journal of Physics*, IOP Publishing, v. 15, n. 5, p. 055018, 2013.

48 FUKUMOTO, K. et al. Femtosecond time-resolved photoemission electron microscopy for spatiotemporal imaging of photogenerated carrier dynamics in semiconductors. *Review of Scientific Instruments*, AIP, v. 85, n. 8, p. 083705, 2014.

49 STROCOV, V. N. et al. Soft-x-ray ARPES at the swiss light source: From 3d materials to buried interfaces and impurities. *Synchrotron Radiation News*, Taylor & Francis, v. 27, n. 2, p. 31–40, 2014.

50 YANG, H. et al. Visualizing electronic structures of quantum materials by angle-resolved photoemission spectroscopy. *Nature Reviews Materials*, Nature Publishing Group, p. 1, 2018.

51 FUKUMOTO, K. et al. Lifetimes of photogenerated electrons on a GaAs surface affected by nanostructural defects. *Applied Physics Express*, IOP Publishing, v. 8, n. 10, p. 101201, 2015.

52 ALFANO, R. R. *Semiconductors probed by ultrafast laser spectroscopy*. [S.l.]: Elsevier, 2012.

53 FRUHLING, U. et al. Single-shot terahertz-field-driven x-ray streak camera. *Nature Photonics*, Nature Publishing Group, v. 3, n. 9, p. 523, 2009.

54 TAHARA, T.; TOLEUTAEV, B. N.; HAMAGUCHI, H.-o. Picosecond time-resolved multiplex coherent anti-stokes Raman scattering spectroscopy by using a streak camera: Isomerization dynamics of all-trans and 9-cis retinal in the lowest excited triplet state. *The Journal of chemical physics*, AIP, v. 100, n. 2, p. 786–796, 1994.

55 TAHARA, T.; HAMAGUCHI, H.-O. Picosecond Raman spectroscopy using a streak camera. *Applied spectroscopy*, Society for Applied Spectroscopy, v. 47, n. 4, p. 391–398, 1993.

56 ZINT, C. V. et al. Streak camera: a multidetector for diffuse optical tomography. *Applied optics*, Optical Society of America, v. 42, n. 16, p. 3313–3320, 2003.

57 WELSCH, C. et al. Status of the CTF3 synchrotron light-monitoring-system. In: CITESEER. *Beam Instrumentation Workshop*. [S.l.], 2008.

58 FOGLIA, L.; WOLF, M.; STAHLER, J. Ultrafast dynamics in solids probed by femtosecond time-resolved broadband electronic sum frequency generation. *Applied Physics Letters*, AIP Publishing LLC, v. 109, n. 20, p. 202106, 2016.

59   CLAYBURN, N. et al. Search for spin-polarized photoemission from GaAs using light with orbital angular momentum. *Physical Review B*, APS, v. 87, n. 3, p. 035204, 2013.

60   SORDILLO, L. A. et al. The interaction of twisted laguerre-gaussian light with a GaAs photocathode to investigate photogenerated polarized electrons. *Applied Physics Letters*, AIP Publishing, v. 114, n. 4, p. 041104, 2019.

61   HU, J. et al. Delayed formation of coherent lo phonon-plasmon coupled modes in n-and p-type GaAs measured using a femtosecond coherent control technique. *Physical Review B*, APS, v. 86, n. 23, p. 235145, 2012.

62   WANG, J. et al. Influence of coherent optical phonon on ultrafast energy relaxation. *Applied Physics Letters*, AIP Publishing LLC, v. 107, n. 6, p. 063107, 2015.

63   CHO, G. C. et al. Time-resolved observation of coherent phonons by the franz-keldysh effect. *Physical Review B*, APS, v. 53, n. 11, p. 6904, 1996.

64   ELZINGA, P. A. et al. Pump/probe spectroscopy by asynchronous optical sampling. *Applied spectroscopy*, SAGE Publications Sage UK: London, England, v. 41, n. 1, p. 2–4, 1987.

65   JIANG, J.; ABUDUWEILI, A. High resolution measurement with asynchronous optical sampling. In: IOP PUBLISHING. *Journal of Physics: Conference Series*. [S.l.], 2019. v. 1213, n. 4, p. 042028.

66   BARTELS, A. et al. Ultrafast time-domain spectroscopy based on high-speed asynchronous optical sampling. *Review of Scientific Instruments*, AIP, v. 78, n. 3, p. 035107, 2007.

67   RULLIERE, C. et al. *Femtosecond laser pulses*. [S.l.]: Springer, 2005.

68   SVELTO, O.; HANNA, D. C. *Principles of lasers*. [S.l.]: Springer, 2010. v. 1.

69   KOZLOV, S. A.; SAMARTSEV, V. V. *Fundamentals of femtosecond optics*. [S.l.]: Elsevier, 2013.

70   KORPEL, A. Acousto-optics—a review of fundamentals. *Proceedings of the IEEE*, IEEE, v. 69, n. 1, p. 48–53, 1981.

71   BRABEC, T. et al. Kerr lens mode locking. *Optics letters*, Optical Society of America, v. 17, n. 18, p. 1292–1294, 1992.

72   FORK, R.; GREENE, B.; SHANK, C. V. Generation of optical pulses shorter than 0.1 psec by colliding pulse mode locking. *Applied Physics Letters*, American Institute of Physics, v. 38, n. 9, p. 671–672, 1981.

73   SADAO, A. Properties of group-iv, iii-v and ii-vi semiconductors. *Hoboken (USA) Wiley&Sons*, 2005.

74   ULBRICHT, R. et al. Carrier dynamics in semiconductors studied with time-resolved terahertz spectroscopy. *Reviews of Modern Physics*, APS, v. 83, n. 2, p. 543, 2011.

75   YOON, J. et al. GaAs photovoltaics and optoelectronics using releasable multilayer epitaxial assemblies. *Nature*, Nature Publishing Group, v. 465, n. 7296, p. 329, 2010.

76 METAFERIA, W. et al. Gallium arsenide solar cells grown at rates exceeding 300 μm h^{-1} by hydride vapor phase epitaxy. *Nature communications*, Nature Publishing Group, v. 10, n. 1, p. 1–8, 2019.

77 GREEN, M. A. et al. Solar cell efficiency tables (version 53). *Progress in Photovoltaics: Research and Applications*, v. 27, n. 1, p. 3–12, 2019. Disponível em: ⟨https://onlinelibrary.wiley.com/doi/abs/10.1002/pip.3102⟩.

78 CHEN, H.-L. et al. A 19.9%-efficient ultrathin solar cell based on a 205-nm-thick GaAs absorber and a silver nanostructured back mirror. *Nature Energy*, Nature Publishing Group, v. 4, n. 9, p. 761–767, 2019.

79 GREEN, M. A. et al. Solar cell efficiency tables (version 55). *Progress in Photovoltaics: Research and Applications*, National Renewable Energy Lab.(NREL), Golden, CO (United States), v. 28, n. NREL/JA-5900-75827, 2019.

80 KING, R. et al. 40% efficient metamorphic GaInP/ GaInAs/ Ge multijunction solar cells. *Applied physics letters*, American Institute of Physics, v. 90, n. 18, p. 183516, 2007.

81 DHILLON, S. et al. Thz sideband generation at telecom wavelengths in a GaAs-based quantum cascade laser. *Applied Physics Letters*, American Institute of Physics, v. 87, n. 7, p. 071101, 2005.

82 BENGLOAN, J.-Y. et al. Intracavity sum-frequency generation in GaAs quantum cascade lasers. *Applied physics letters*, American Institute of Physics, v. 84, n. 12, p. 2019–2021, 2004.

83 FU, Z.; YAMAGUCHI, M. Coherent excitation of optical phonons in GaAs by broadband terahertz pulses. *Scientific reports*, Nature Publishing Group, v. 6, p. 38264, 2016.

84 PRIETO, E. A. P. et al. Intense THz emission in high quality MBE -grown GaAs film with a thin n-doped buffer. *Optical Materials Express*, Optical Society of America, v. 8, n. 6, p. 1463–1471, 2018.

85 DU, Y. A.; SAKONG, S.; KRATZER, P. As vacancies, ga antisites, and au impurities in zinc blende and wurtzite gaas nanowire segments from first principles. *Physical Review B*, APS, v. 87, n. 7, p. 075308, 2013.

86 GOOCH, C.; HILSUM, C.; HOLEMAN, B. Properties of semi-insulating GaAs. *Journal of Applied Physics*, AIP, v. 32, n. 10, p. 2069–2073, 1961.

87 BALAGHI, L. et al. Widely tunable GaAs bandgap via strain engineering in core/shell nanowires with large lattice mismatch. *Nature communications*, Nature Publishing Group, v. 10, n. 1, p. 1–10, 2019.

88 STROBL, G. et al. Strained GaAs layers grown on GaAs substrates with an intermediate GaAs$_{1-x}$ P$_x$ buffer layer. *Journal of applied physics*, American Institute of Physics, v. 70, n. 1, p. 198–203, 1991.

89 KOGUCHI, N.; ISHIGE, K.; TAKAHASHI, S. New selective molecular-beam epitaxial growth method for direct formation of GaAs quantum dots. *Journal of Vacuum Science & Technology B: Microelectronics and Nanometer Structures Processing, Measurement, and Phenomena*, American Vacuum Society, v. 11, n. 3, p. 787–790, 1993.

90 ANJOS, V.; IORIATTI, L.; NUNES, L. Resonant Raman spectra of spin-density transitions in periodically δ-doped GaAs. *Physical Review B*, APS, v. 49, n. 11, p. 7805, 1994.

91 SADASIVAM, S.; CHAN, M. K.; DARANCET, P. Theory of thermal relaxation of electrons in semiconductors. *Physical review letters*, APS, v. 119, n. 13, p. 136602, 2017.

92 POLLAK, F. H.; CARDONA, M. Energy band structure of germanium and gallium arsenide: The kp method. *Journal of Physics and Chemistry of Solids*, Elsevier, v. 27, n. 2, p. 423–425, 1966.

93 CLADY, R. et al. Interplay between the hot phonon effect and intervalley scattering on the cooling rate of hot carriers in GaAs and InP. *Progress in Photovoltaics: Research and Applications*, Wiley Online Library, v. 20, n. 1, p. 82–92, 2012.

94 STRAUCH, D.; DORNER, B. Phonon dispersion in gaas. *Journal of Physics: Condensed Matter*, IOP Publishing, v. 2, n. 6, p. 1457, 1990.

95 KITTEL, C.; MCEUEN, P.; MCEUEN, P. *Introduction to solid state physics*. [S.l.]: Wiley New York, 1996. v. 8.

96 SCHOLES, G. D. et al. Using coherence to enhance function in chemical and biophysical systems. *Nature*, Nature Publishing Group, v. 543, n. 7647, p. 647–656, 2017.

97 WANG, L.; ALLODI, M. A.; ENGEL, G. S. Quantum coherences reveal excited-state dynamics in biophysical systems. *Nature Reviews Chemistry*, Nature Publishing Group, v. 3, n. 8, p. 477–490, 2019.

98 KUZNETSOVA, I. et al. Determination of homogeneous and inhomogeneous broadening in semiconductor nanostructures by two-dimensional fourier-transform optical spectroscopy. *Physical Review B*, APS, v. 76, n. 15, p. 153301, 2007.

99 ZHANG, W. M.; CHERNYAK, V.; MUKAMEL, S. Multidimensional femtosecond correlation spectroscopies of electronic and vibrational excitons. *The Journal of chemical physics*, American Institute of Physics, v. 110, n. 11, p. 5011–5028, 1999.

100 TEKAVEC, P. F.; LOTT, G. A.; MARCUS, A. H. Fluorescence-detected two-dimensional electronic coherence spectroscopy by acousto-optic phase modulation. *The Journal of chemical physics*, American Institute of Physics, v. 127, n. 21, p. 214307, 2007.

101 HAREL, E. Four-dimensional coherent electronic raman spectroscopy. *The Journal of chemical physics*, AIP Publishing LLC, v. 146, n. 15, p. 154201, 2017.

102 SHAH, J. *Hot carriers in semiconductor nanostructures: Physics and applications.* [S.l.]: Elsevier, 2012.

103 PRABHU, S.; VENGURLEKAR, A. Dynamics of the pump-probe reflectivity spectra in GaAs and GaN. *Journal of applied physics*, American Institute of Physics, v. 95, n. 12, p. 7803–7812, 2004.

104 SALEH, B. E.; TEICH, M. C. *Fundamentals of photonics*. [S.l.]: John Wiley & Sons, 2019.

105 DAMEN, T. et al. Dynamics of exciton formation and relaxation in gaas quantum wells. *Physical Review B*, APS, v. 42, n. 12, p. 7434, 1990.

106 BOTT, K. et al. Dephasing of interacting heavy-hole and light-hole excitons in gaas quantum wells. *JOSA B*, Optical Society of America, v. 13, n. 5, p. 1026–1030, 1996.

107 RYAN, J.; REINECKE, T. Band-gap renormalization of optically excited semiconductor quantum wells. *Physical Review B*, APS, v. 47, n. 15, p. 9615, 1993.

108 MOSKO, M.; MOSKOVA, A.; CAMBEL, V. Carrier-carrier scattering in photoexcited intrinsic gaas quantum wells and its effect on femtosecond plasma thermalization. *Physical Review B*, APS, v. 51, n. 23, p. 16860, 1995.

109 ELSAESSER, T. et al. Initial thermalization of photoexcited carriers in gaas studied by femtosecond luminescence spectroscopy. *Physical review letters*, APS, v. 66, n. 13, p. 1757, 1991.

110 HONOLD, A. et al. Collision broadening of two-dimensional excitons in a gaas single quantum well. *Physical Review B*, APS, v. 40, n. 9, p. 6442, 1989.

111 KERSTING, R. et al. Coherent plasmons in n-doped GaAs. *Physical Review B*, APS, v. 58, n. 8, p. 4553, 1998.

112 HUBER, R. et al. How many-particle interactions develop after ultrafast excitation of an electron–hole plasma. *Nature*, Nature Publishing Group, v. 414, n. 6861, p. 286, 2001.

113 SCHOLL, E. *Theory of transport properties of semiconductor nanostructures*. [S.l.]: Springer Science & Business Media, 2013. v. 4.

114 ROSSI, F.; KUHN, T. Theory of ultrafast phenomena in photoexcited semiconductors. *Reviews of Modern Physics*, APS, v. 74, n. 3, p. 895, 2002.

115 ZIAJA, B. et al. Time-resolved observation of band-gap shrinking and electron-lattice thermalization within x-ray excited gallium arsenide. *Scientific reports*, Nature Publishing Group, v. 5, p. 18068, 2015.

116 ALEXANDROU, A.; BERGER, V.; HULIN, D. Direct observation of electron relaxation in intrinsic GaAs using femtosecond pump-probe spectroscopy. *Physical Review B*, APS, v. 52, n. 7, p. 4654, 1995.

117 YOUNG, J. F. et al. Carrier-carrier scattering rates within nonequilibrium optically injected semiconductor plasmas. *Physical Review B*, APS, v. 50, n. 4, p. 2208, 1994.

118 BECKER, P. et al. Femtosecond photon echoes from band-to-band transitions in GaAs. *Physical review letters*, APS, v. 61, n. 14, p. 1647, 1988.

119 SJAKSTE, J. et al. Hot electron relaxation dynamics in semiconductors: assessing the strength of the electron–phonon coupling from the theoretical and experimental viewpoints. *Journal of Physics: Condensed Matter*, IOP Publishing, v. 30, n. 35, p. 353001, 2018.

120 RUHLE, W.; LEO, K. Carrier heating in gaas by nonradiative recombination. *physica status solidi (b)*, Wiley Online Library, v. 149, n. 1, p. 215–220, 1988.

121 SJAKSTE, J. et al. Energy relaxation mechanism of hot-electron ensembles in GaAs: Theoretical and experimental study of its temperature dependence. *Physical Review B*, APS, v. 97, n. 6, p. 064302, 2018.

122 ROSENWAKS, Y. et al. Hot-carrier cooling in GaAs: Quantum wells versus bulk. *Physical Review B*, APS, v. 48, n. 19, p. 14675, 1993.

123 SHAH, J. et al. Energy-loss rates for hot electrons and holes in GaAs quantum wells. *Physical review letters*, APS, v. 54, n. 18, p. 2045, 1985.

124 RUELLO, P.; GUSEV, V. E. Physical mechanisms of coherent acoustic phonons generation by ultrafast laser action. *Ultrasonics*, Elsevier, v. 56, p. 21–35, 2015.

125 PFEIFER, T. et al. Generation mechanism for coherent LO phonons in surface-space-charge fields of III-V-compounds. *Applied physics A*, Springer, v. 55, n. 5, p. 482–488, 1992.

126 WEINER, A. M. et al. Femtosecond multiple-pulse impulsive stimulated Raman scattering spectroscopy. *JOSA B*, Optical Society of America, v. 8, n. 6, p. 1264–1275, 1991.

127 RUHMAN, S.; JOLY, A. G.; NELSON, K. A. Coherent molecular vibrational motion observed in the time domain through impulsive stimulated Raman scattering. *IEEE journal of quantum electronics*, IEEE, v. 24, n. 2, p. 460–469, 1988.

128 ZEIGER, H. et al. Theory for displacive excitation of coherent phonons. *Physical Review B*, APS, v. 45, n. 2, p. 768, 1992.

129 MANTE, P.-A. et al. Thz acoustic phonon spectroscopy and nanoscopy by using piezoelectric semiconductor heterostructures. *Ultrasonics*, Elsevier, v. 56, p. 52–65, 2015.

130 YU, P. Y.; CARDONA, M. *Fundamentals of semiconductors: physics and materials properties*. [S.l.]: Springer, 1996.

131 ZOLLNER, S.; GOPALAN, S.; CARDONA, M. Intervalley deformation potentials and scattering rates in zinc blende semiconductors. *Applied physics letters*, AIP, v. 54, n. 7, p. 614–616, 1989.

132 BERNARDI, M. et al. Ab initio study of hot electrons in GaAs. *Proceedings of the National Academy of Sciences*, National Acad Sciences, v. 112, n. 17, p. 5291–5296, 2015.

133 OSMAN, M.; FERRY, D. K. Monte carlo investigation of the electron-hole-interaction effects on the ultrafast relaxation of hot photoexcited carriers in GaAs. *Physical Review B*, APS, v. 36, n. 11, p. 6018, 1987.

134 BAYKAN, M. O.; THOMPSON, S. E.; NISHIDA, T. Strain effects on three-dimensional, two-dimensional, and one-dimensional silicon logic devices: Predicting the future of strained silicon. *Journal of Applied Physics*, American Institute of Physics, v. 108, n. 9, p. 093716, 2010.

135 STANTON, C.; BAILEY, D. Rate equations for the study of femtosecond intervalley scattering in compound semiconductors. *Physical Review B*, APS, v. 45, n. 15, p. 8369, 1992.

136 EREMENTCHOUK, M.; LEUENBERGER, M. N.; SHAM, L. Many-body interaction in semiconductors probed with two-dimensional fourier spectroscopy. *Physical Review B*, APS, v. 76, n. 11, p. 115307, 2007.

137 LEE, Y.-H. et al. Room-temperature optical nonlinearities in GaAs. *Physical review letters*, APS, v. 57, n. 19, p. 2446, 1986.

138 COLLET, J. et al. Influence of electron-hole correlations on the absorption of GaAs in the presence of nonthermalized carriers. *Physical Review B*, APS, v. 50, n. 15, p. 10649, 1994.

139 BANYAI, L.; KOCH, S. W. A simple theory for the effects of plasma screening on the optical spectra of highly excited semiconductors. *Zeitschrift für Physik B Condensed Matter*, Springer, v. 63, n. 3, p. 283–291, 1986.

140 MENDOZA-ALVAREZ, J.; YAN, R.; COLDREN, L. Contribution of the band-filling effect to the effective refractive-index change in double-heterostructure GaAs/AlGaAs phase modulators. *Journal of applied physics*, American Institute of Physics, v. 62, n. 11, p. 4548–4553, 1987.

141 TRÄNKLE, G. et al. Dimensionality dependence of the band-gap renormalization in two-and three-dimensional electron-hole plasmas in GaAs. *Physical review letters*, APS, v. 58, n. 4, p. 419, 1987.

142 CHOW, W. W.; KOCH, S. W. *Semiconductor-laser fundamentals: physics of the gain materials*. [S.l.]: Springer Science & Business Media, 1999.

143 STOLZ, W.; GUIMARAES, F.; PLOOG, K. Optical and structural properties of gaas grown on (100) si by molecular-beam epitaxy. *Journal of applied physics*, American Institute of Physics, v. 63, n. 2, p. 492–499, 1988.

144 KATZENELLENBOGEN, N.; GRISCHKOWSKY, D. Electrical characterization to 4 thz of n-and p-type gaas using thz time-domain spectroscopy. *Applied physics letters*, American Institute of Physics, v. 61, n. 7, p. 840–842, 1992.

145 PANDIT, S.; KRISHNAMURTHY, M. Study of femtosecond pulse laser.

146 LEBEDEV, M. et al. On the nature of "coherent artifact". *Journal of Experimental and Theoretical Physics*, Springer, v. 100, n. 2, p. 272–282, 2005.

147 MANUAL of Mai Tai HP Laser. Spectra Physics Company, p. 50–53.

148 FROLOV, S.; VARDENY, Z. Double-modulation electro-optic sampling for pump-and-probe ultrafast correlation measurements. *Review of Scientific Instruments*, American Institute of Physics, v. 69, n. 3, p. 1257–1260, 1998.

149 MANUAL of optical chopper, Model SR540. [S.l.]: Stanford Research Systems.

150 TUNYAGI, A. et al. Non-collinear second harmonic generation in strontium barium niobate. 2004.

151 WANG, Z. et al. Noncollinear second-harmonic generation in bib 3 o 6. *JOSA B*, Optical Society of America, v. 21, n. 7, p. 1348–1353, 2004.

152 OHTAKE, A. Surface reconstructions on GaAs (001). *Surface Science Reports*, Elsevier, v. 63, n. 7, p. 295–327, 2008.

153 HASE, M. et al. Ultrafast carrier and plasmon-phonon dynamics in ion-irradiated n-GaAs. *Applied physics letters*, AIP, v. 82, n. 21, p. 3668–3670, 2003.

154 MCINTOSH, K. et al. Investigation of ultrashort photocarrier relaxation times in low-temperature-grown GaAs. *Applied physics letters*, AIP, v. 70, n. 3, p. 354–356, 1997.

155 LUYO, S. J. et al. Carrier dynamics investigated by time resolved optical spectroscopy. *Brazilian journal of physics*, SciELO Brasil, v. 32, n. 2A, p. 353–355, 2002.

156 RUZICKA, B. A. et al. Ambipolar diffusion of photoexcited carriers in bulk GaAs. *Applied Physics Letters*, AIP, v. 97, n. 26, p. 262119, 2010.

157 COOK, C. et al. Ultrafast carrier relaxation and diffusion dynamics in zno. In: INTERNATIONAL SOCIETY FOR OPTICS AND PHOTONICS. *Oxide-based Materials and Devices*. [S.l.], 2010. v. 7603, p. 760304.

158 WILLIAMS, G. J. et al. Direct measurements of multi-photon induced nonlinear lattice dynamics in semiconductors via time-resolved x-ray scattering. *Scientific reports*, Nature Publishing Group, v. 6, p. 39506, 2016.

159 ERSKINE, D.; TAYLOR, A.; TANG, C. Dynamic burstein–Moss shift in GaAs and GaAs/AlGaAs multiple quantum well structures. *Applied Physics Letters*, AIP, v. 45, n. 11, p. 1209–1211, 1984.

160 KATZ, A.; ALFANO, R. Intervalley scattering rates in GaAs measured by time-resolved four-wave mixing spectroscopy. *Applied physics letters*, AIP, v. 53, n. 12, p. 1065–1067, 1988.

161 SHAH, J. et al. Determination of intervalley scattering rates in GaAs by subpicosecond luminescence spectroscopy. *Physical review letters*, APS, v. 59, n. 19, p. 2222, 1987.

162 TANIMURA, H. et al. Formation of hot-electron ensembles quasiequilibrated in momentum space by ultrafast momentum scattering of highly excited hot electrons photoinjected into the Γ valley of GaAs. *Physical Review B*, APS, v. 93, n. 16, p. 161203, 2016.

163 LEITENSTORFER, A. et al. Femtosecond carrier dynamics in GaAs far from equilibrium. *Physical review letters*, APS, v. 76, n. 9, p. 1545, 1996.

164 LIU, T.-H. et al. First-principles mode-by-mode analysis for electron-phonon scattering channels and mean free path spectra in gaas. *Physical Review B*, APS, v. 95, n. 7, p. 075206, 2017.

165 MAHAN, G. D. *Condensed matter in a nutshell*. [S.l.]: Princeton University Press, 2011. v. 8.

166 CAVASSILAS, N. et al. Full-band matrix solution of the boltzmann transport equation and electron impact ionization in gaas. *Solid-State Electronics*, Elsevier, v. 46, n. 4, p. 559–566, 2002.

167 VALLÉE, F. Time-resolved investigation of coherent lo-phonon relaxation in iii-v semiconductors. *Physical Review B*, APS, v. 49, n. 4, p. 2460, 1994.

168 KLEMENS, P. Anharmonic decay of optical phonons. *Physical Review*, APS, v. 148, n. 2, p. 845, 1966.

169 POMEROY, J. et al. Phonon lifetimes and phonon decay in InN. *Applied Physics Letters*, American Institute of Physics, v. 86, n. 22, p. 223501, 2005.

170 VALLÉE, F.; BOGANI, F. Coherent time-resolved investigation of lo-phonon dynamics in gaas. *Physical Review B*, APS, v. 43, n. 14, p. 12049, 1991.

171 NIE, X.-C. et al. Exciton-phonon and exciton-exciton interactions in GaAs by time-resolved optical reflectivity. *Results in Physics*, Elsevier, v. 12, p. 1089–1090, 2019.